3D Numerical Simulation of River Flow and Sediment Transport around Spur Dikes

于　合理（YU HELI）

2024

3D Numerical Simulation of River Flow and Sediment Transport around Spur Dikes

A dissertation submitted in partial fulfillment for the requirement of Doctoral Degree in Civil and Earth Resources Engineering

by

于　合理（YU HELI）

Supervised by Prof. KAWAIKE Kenji

Laboratory of Hydroscience and Hydraulic Engineering
Department of Civil and Earth Resources Engineering
Graduate School of Engineering
Kyoto University
Japan

2024

Abstract

Spur dikes serve as common hydraulic structures employed for purposes like bank protection, river training, navigation, and habitat improvement. Constructing spur dikes against an approaching flow leads to the development of intricate 3-dimensional flow structures, including flow separation and multiple vortices. This intricate flow pattern induces significant bed shear stress and turbulence in the vicinity of the spur dike, serving as the primary mechanism for local scour. In cases where the design of spur dikes is inappropriate, the formation of local scours may pose a threat to the stability of spur dikes, potentially resulting in their failure. Unlike artificial channels with long straight reaches, most natural rivers exhibit a distinct absence of such features, characterized instead by frequent meanders. These meanders introduce complex flow structures like cross-circulation, enhancing the randomness of both flow and sediment transport around spur dikes.

The literature review highlights that the majority of prior studies on spur dikes have been conducted either in straight flumes or within a single curved channel. There has been limited emphasis on investigating the optimal spacing in meandering channels and its correlation with channel sinuosity and the placement of spur dikes.

Therefore, at first, the numerical investigation was conducted in various meandering channels utilizing a 3D multiphase OpenFOAM solver, building upon the non-equilibrium sediment transport model previously developed by former students in our laboratory. The model comprises both a hydrodynamic component and a sediment transport component. The hydrodynamic model incorporates the porous medium method (PMM) to account for seepage flow within the bed, the volume of fluid (VOF) method for capturing the free surface, and the $k-\omega$ SST SAS model to simulate turbulence effects. For sediment transport, the model employs the Eulerian method for suspended load and the Lagrangian method for bed load. Benefiting from the PMM, the fixed mesh can be used to simulate bed deformation, making it suitable for large deformations. Additionally, the Lagrangian method facilitates the consideration of non-equilibrium sediment transport induced by spur dikes. Based on the previous applications in straight channels, the model was tested for flow field with a U-shaped channel experiment and for bed deformation based on a movable bed experiment in a meandering channel to validate its applicability to the investigation of flow and sediment

transport around spur dikes in meandering channels.

Spacing serves as a critical parameter for striking a balance between performance and construction costs. It is related to the downstream separation zone length of a spur dike. Consequently, a single spur dike was systematically positioned at various locations within diverse meandering channels to examine the impact of its placement and its correlation with channel sinuosity. The length of the downstream separation zone and the depth of local scour are contingent upon both the location of the spur dike and the sinuosity of the channel. As the spur dike is shifted downstream or the channel sinuosity decreases, the downstream separation zone undergoes a reduction in length. Concurrently, the local scour depth increases as the spur dike is displaced downstream, peaking near the crossover point. Upstream of this point, channels characterized by higher sinuosity display deeper local scours, while downstream, the opposite trend is observed.

Subsequently, a series of spur dikes with different spacings were installed across diverse meandering channels to examine the combined influence of spacing and channel sinuosity. Pronounced local scours were observed near the most upstream spur dike and spur dikes downstream of the meander apex. As the spacing between spur dikes increased, intact scour holes appeared from downstream, accompanied by a rise in potential bank erosion. Additionally, the flow near the spur tips exhibited increased turbulence with a higher velocity gradient. In most instances, the maximum local scour depth exhibited an upward trend with increasing spacing and a downward trend with higher channel sinuosity. To enhance cost-effectiveness, adopting non-uniform spacing is recommended, with different channel sinuosities necessitating distinct spacing arrangements. Furthermore, an equation, utilizing the weighted-sum approach for multi-objective programming problems, was proposed to quantify overall performance by comprehensively considering factors such as bank protection, structural stability, construction costs, and aquatic habitats based on the simulation results.

Bank erosion constitutes a crucial process in the morphological adjustment of rivers, contributing to channel migration, the loss of agricultural land, and potential damage to hydraulic structures and infrastructure. Recognizing the limited consideration of bank erosion modeling in previous numerical studies on spur dikes, a novel OpenFOAM solver was developed. This solver incorporates a bank mass failure operator into the existing 3D model to address this gap. The bank mass failure operator assesses the slope angle of each

bed surface cell in comparison to the critical angle, submerged or emerged, determining stability and simulating collapse by rotating unstable cells. This approach eliminates the explicit identification of the riverbank's location, significantly enhancing convenience. The model's performance was rigorously tested through three experiments: a straight channel dam-break experiment, a meandering channel experiment without spur dikes, and a meandering channel experiment with spur dikes. Based on these validations, it can be concluded that the model is well-suited for evaluating the performance of spur dikes against bank erosion and exploring temporal changes in planforms within meandering channels.

Finally, the new solver was implemented to assess a river reach facing severe bank erosion along the Uji River. Initially, a flood event was reproduced, demonstrating favorable agreement with water level measurements. The model could simulate bank failure during rising water levels to some extent, although some limitations were identified in predicting fluvial erosion in the main channel and bank toe. Analysis of near-bed velocity and bed shear stress distribution at various flood stages suggested that the bank erosion process involved toe erosion at lower flows, followed by collapse during or after the flood peak. Simulations incorporating spur dikes were conducted, incorporating two different spacings. The spur dikes efficiently redirected the flow away from the bank, diminishing velocity at the toe and safeguarding against erosion. Moreover, the impact on the aquatic habitat of $Zacco\ platypus$, the dominant species in the river basin, was evaluated. The weighted usable area (WUA) experienced a slight increase with the installation of spur dikes, with a correlation to spacing – larger spacings yielded greaterWUA. Overall, the larger of the two spacings performed better.

Keyword: spur dike, meandering channel, bank erosion, 3D simulation

Acknowledgments

The dissertation was written during my study at the Laboratory of Hydroscience and Hydraulic Engineering of Kyoto University. I started my PhD just at the onset of the COVID-19 pandemic, a time fraught with numerous challenges and uncertainties. Nonetheless, I made it to the finish line. I would like to express my heartfelt gratitude to the exceptional individuals who provided support and guidance during this transformative journey, enabling me to attain my doctorate despite unforeseen obstacles.

First and foremost, I would like to express my deepest gratitude to my supervisor Prof. Dr. Kenji KAWAIKE, Disaster Prevention Research Institute (DPRI), Kyoto University. His constant support, patient guidance, encouragement, and advice have been invaluable throughout the entire process. From the initial stages of determining my research topic to the final submission of my thesis, his unwavering presence and wealth of wisdom have been instrumental in shaping my academic growth. I am also deeply grateful to Asst. Prof. Dr. Kazuki YAMANOI and Asst. Prof. Dr. Takahiro KOSHIBA for their support, valuable suggestions, and comments for my research and their help in my life. I greatly appreciated the seminars we held in our laboratory, which not only served as crucial checkpoints to keep me on track academically but also offered abundant encouragement. I am profoundly thankful for the immeasurable contributions they made to my development.

I am deeply grateful to my sub-supervisors, Prof. Dr. Masaharu FUJITA, Prof. Dr. Kana NAKATANI, and Assoc. Prof. Dr. Nozomu YONEYAMA, DPRI, Kyoto University, for their support throughout my doctoral course.

I would like to express my sincere gratitude to the reviewers of my thesis, Prof. Dr. Michio SANJOU, and Assoc. Prof. Dr. Nozomu YONEYAMA, DPRI, Kyoto University, for dedicating their time and effort to read my thesis and provide valuable comments and suggestions to improve the thesis.

I am deeply grateful to Dr. Kazuyuki OTA, Central Research Institute of Electric Power Industry, Japan, and Masaki OKUDAIRA for their support. My research was carried out based on their OpenFOAM codes.

I would like to thank Ms. YAMAMOTO for her continuous help. She has not only provided support in the daily affairs of our lab but has also been helpful in my life in Japan.

In addition, I am indebted to the exceptional lab mates, whose support has been a constant source of motivation. I am grateful to my friend Dr. DING can, who reinforced my decision to resign and come to Japan for further studies and helped me quickly adapt to studying and living in Japan. I am grateful to my tutors, Gaku SASAKI and Koshi SHINOHARA for assisting me in getting acquainted with studying and living in Japan when I first arrived. I would also like to thank ZHU Wei and Hibiki KITAJIMA, whose enthusiasm and upbeat character positively influenced those around them.

I would also like to thank all the staff at the Ujigawa Open Laboratory for their friendliness, positive attitude, and always being ready to help.

I would also like to take the opportunity to acknowledge Monbukagakusho (Ministry of Education, Culture, Sports, Science and Technology (MEXT), Japan) for financial support during my studies and the China Scholarship Council (CSC) for the opportunity and support to apply for the scholarship.

Lastly, I want to express my deepest gratitude to my family for their belief in my abilities and support. Their encouragement played an integral role in my accomplishments.

Contents

Chapter 1.
Introduction

1.1. General

Spur dikes (also known as spurs, groynes, or transverse dikes) are structures or embankments constructed in a river transverse to the flow. They project a fair distance from the bank into the stream, deflecting the flowing water away from the bank and also contracting the effective channel width, thereby promoting sediment scour and deposition in the desired areas. They prevent the erosion of the bank and establish a more desirable width and channel alignment. Spur dikes are probably the most widely used river training structures and serve the following function (Asawa, 2006; Yamamoto, 1996):

(1) protecting the river bank by diverting the flow away from the river bank; (2) training a river along the desired course by attracting, deflecting, or repelling the flow in the river channel; (3) narrowing the river channel width for ensuring an adequate water depth for navigation; (4) raising the water level for the water intake or adjusting the flow diversion ratio at a river fork; (5) creating a slack flow with the aim of silting up the area in the vicinity of spur dikes; (6) fostering diverse aquatic environments with pools, riffles, and diversified flow induced by spur dikes; (7) simultaneously serving as components of landscape design while fulfilling the above functionalities.

Spur dikes can be classified into various types (Asawa, 2006; Yossef, 2002; Zhang and Nakagawa, 2008):

(1) permeable and impermeable based on the methods and materials of construction. Permeable spur dikes typically consist of piles, bamboo, or timbers, whereas impermeable spur dikes are made from rock, gravel, gabions, etc.

(2) submerged and non-submerged according to the height of the spur with respect to high flood level. Generally, impermeable spur dikes are designed to be non-submerged, while submerged spur dikes may be designed permeable.

(3) attracting, deflecting, and repelling according to the orientation. An attracting spur dike is positioned downstream, attracting the stream towards its head. A deflecting spur dike is typically perpendicular to the bank and serves local protection, diverting the flow at its

head. A repelling spur dike points upstream, diverting the flow away from itself.

(4) straight, T-shaped, L-shaped, hockey-shaped, etc., based on the appearance in the plan view.

Spur dikes have been implemented since ancient times in various countries around the world. In Japan, as early as the Edo period in 1669, a document recorded the existence of spur dikes known as 'dashi', constructed using locally available materials such as soil, stones, and wood, employing empirically devised techniques based on practical experience. In addition, the river section of the Tone River (the second longest river in Japan) from 184 to 120 km, including alluvial fans and natural embankment zones, has over half of its river banks protected by spur dikes. Numerous pile-type spur dikes with a length of 20 ~ 30 m were installed in the sand bed rivers of the Hokuriku region, such as the Shinano River and the Agano River in the 1950s (Yamamoto, 1996).

In China, spur dikes are widely used for river regulation practices. For instance, by 1997, a total of 9, 069 spur dikes with a combined length of 646, 861 m, including 5, 369 spur dikes for protecting the Levee and 3, 700 spur dikes for guiding flow, had been constructed in the Lower Yellow River, the famous raised bed river (Wu et al., 2005).

In Europe, spur dikes were constructed locally since the Middle Ages to protect river banks against erosion in the Rhine River. Systematic training of long river reaches commenced in the 19th century. Hundreds of spur dikes were constructed along the Dutch Rhine branches between 1850 and 1880 to achieve a uniform width (Mosselman, 2020).

However, as a type of in-stream structure extended from the bank into the stream, spur dikes narrow the flow, alter the hydraulic conditions, and result in non-equilibrium sediment transport, producing a notable impact on the fluvial environment. As shown in Figure 1.1, the flow structure around a single rectangular spur dike is typically complex and highly 3 dimensional (Zhang and Nakagawa, 2008). The flow structure includes: (1) separation of the flow from the side wall upstream of the spur dike, (2) consequently formation of recirculation regions both upstream and downstream of the spur dike, and (3) formation of a strong down flow resulting from a stagnant vertical pressure gradient immediately at the upstream of the spur dike, and (4) a bow wave forming near the water surface, and (5) formation of the horseshoe vortex at the spur dike base due to the interaction of the down flow and the approach boundary layer, and (6) a fully turbulent and dynamic detached shear layer in the mixing zone (Paik and Sotiropoulos, 2005; Safarzadeh et al., 2016; Zhang and

Nakagawa, 2008). The complex flow pattern results in substantial bed shear stress and turbulence around the spur dike, providing the principal mechanism for local scour (Basser et al., 2015; Safarzadeh et al., 2016). The development of local scour poses a risk to the stability of spur dikes and even may cause their failure.

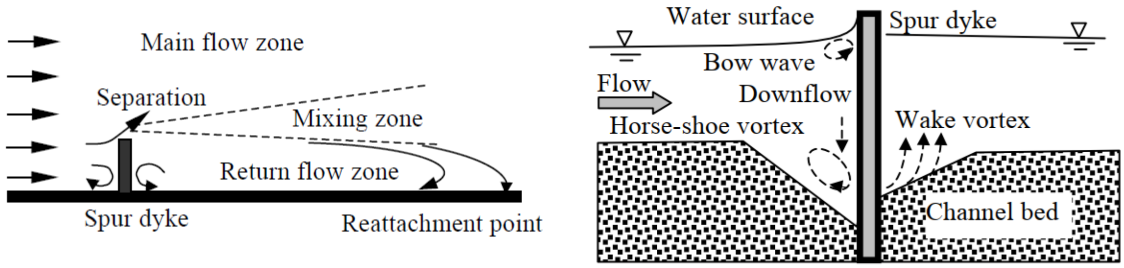

(a) Plan view (b) Elevation view

Figure 1.1 Typical flow field around a spur dike (source: (Zhang and Nakagawa, 2008))

1.2. Previous Studies

1.2.1. Experimental studies on spur dike

Due to the complexity of the flow field in the vicinity of spur dikes and the potential for severe local scour that may lead to structure failure, as listed in Table 1.1, many researchers have conducted experiments to characterize the flow structure and understand the underlying process and mechanisms of bed evolution.

Many experiments have been carried out on flumes with a rigid bed and a single spur dike. Ettema and Muste (Ettema and Muste, 2004) conducted a series of experiments to determine the scale effect in small-scale models. Duan (Duan, 2009) measured the mean and turbulent flow field and obtained that the maximum bed shear stress was approximately 3 times the mean bed-stress stress of the approaching flow. Then, Duan et al. (Duan et al., 2009) compared them with the measurements in a scoured bed and concluded that the development of the local scour was related to the high shear stress zone induced by horseshoe vortices. Some researchers evaluated the effect of the layout of a spur dike, such as the head type (Safarzadeh et al., 2016), and orientation (Abadi and Bateni, 2017; Elawady and Hinokidani, 2000). Elawady and Hinokidani (Elawady and Hinokidani, 2000) also observed the velocity and water surface with different submergences by changing spur dike height.

In addition, Kuang et al. (Kuang et al., 2021) investigated the spacing between 2 spur dikes, but these 2 spur dikes were not located on the same side of the channel. Although rare, a few investigators conducted experiments in meandering channels with a rigid bed (Giri et al., 2003; Sharma and Mohapatra, 2012). Sharma and Mohapatra (Sharma and Mohapatra, 2012) investigated the effect of the spur dike location and Froude number on the velocity amplification, and the length and width of the separation zone downstream of the spur dike.

Table 1.1 Experiments related to spur dike

References	Channel	Spur	Objective
(Elawady and Hinokidani, 2000)	Straight; rigid bed	A single spur; 3 orientations; 2 heights (different submergences);	The water surface and velocity.
(Ettema and Muste, 2004)	Straight; rigid bed	A single spur	The scale effects of small-scale flume experiments.
(Duan, 2009)	Straight; rigid bed	A single spur	The mean and turbulence characteristics.
(Duan et al., 2009)	Straight; rigid flat bed and scoured bed	A single spur	The differences in the measured flow velocity and turbulence field between the two beds.
(Safarzadeh et al., 2016)	Straight; rigid bed	A single spur; different head type (straight and T-shaped)	The effect of head shape on mean and turbulent flow structure
(Abadi and Bateni, 2017)	Straight; rigid bed	A T-shaped spur; 2 orientations	The upstream and downstream separation zone length and flow field.
(Kuang et al., 2021)	Straight; rigid bed	2 bilateral spurs	The effect of spacing on the backflow pattern and recirculation zone length.
(Uijttewaal et al., 2001)	Straight; rigid bed	A series of spurs; 2 geometries	The exchange processes between the main stream and spur fields.
(Giri et al., 2003)	Meandering; rigid bed	Different numbers (0, 1, 2, 3)	The influence on flow structure near spurs and in the further downstream region.
(Sharma and Mohapatra, 2012)	Meandering; rigid bed	A single spur; different locations	The effect of spur location and the Froude number on separation zone.
(Kuhnle et al., 2002)	Straight; movable bed	A single spur; 3 orientations;2 perpendicular lengths	The effect of orientations on the volume of scour, potential bank erosion, and aquatic habitat.
(Karami et al., 2008)	Straight; movable bed	A protective spur + a series of spurs	The effect of length and spacing of the protective spur dike on the scour depth.
(Karami et al., 2012)	Straight; movable bed	A series of spurs	The temporal variation of the scour depth around the first spur dike.
(Sadat and Tominaga, 2015)	Straight; movable bed	Pile-group + a single spur	The effect of the spacing between two structures on flow and local scour.
(Fazli et al.,	A 90-degree bend;	A single spur; 3 lengths;	The effect of Froude number, spur

References	Channel	Spur	Objective
2008)	movable bed	4 locations	location, and length on flow pattern and local scour, the empirical equation for maximum scour depth.
(Rashedipoor et al., 2012)	A 180-degree bend; movable bed	A single spur; 4 locations	The effect of Froude number and spur location on the depth, length, and width of the scour hole.
(Masjedi et al., 2011)	A 180-degree bend; movable bed	A single L-shaped spur; 4 lengths; 4 locations;	The effect of Froude number, spur location, and length on the scour depth, the empirical equation for temporal variation of scour depth.
(Giri and Shimizu, 2004)	Meandering; movable bed	Different numbers and different locations.	The bed deformation near spurs and in the further downstream region, the vegetation impact, and the empirical equation for temporal variation of scour depth.
(Tripathi and Pandey, 2021a)	Meandering; movable bed	A T-shaped spur; 4 locations	The effect of Froude number and spur location on local scour, the empirical equation for the temporal maximum scour depth.
(Burele et al., 2012)	Physical model of an actual river; movable bed	A series of spurs	The performance of the spurs.

A variety of studies have also been conducted in channels with a movable bed for local scour and bed evolution. Many researchers fitted the empirical equation for temporal variation of local scour depth using experimental data for not only straight channels (Karami et al., 2012) but also curved channels (bends and meandering channels) (Fazli et al., 2008; Giri and Shimizu, 2004; Masjedi et al., 2011; Rashedipoor et al., 2012; Tripathi and Pandey, 2021a). Karami et al. (Karami et al., 2012) also concluded that 70 ~ 90 % of the maximum scour depth was completed during the initial 20 % of the time and proposed a regression model and artificial neural networks (ANNs) for estimation of time-dependent scour depth using the collected experimental data.

Besides, Karami et al. (Karami et al., 2008) placed a protective spur dike upstream of a series of spur dikes and presented the effect of its distance on the local scour around the first spur dike. Sadat and Tominaga (Sadat and Tominaga, 2015) combined an impermeable spur dike and a group of piles and investigated the optimum distance between them to decrease the local scour.

Kuhnle et al. (Kuhnle et al., 2002) investigated the effect of orientation and contraction ratio on the scour volume, and potential bank erosion (erosion volume per unit length adjacent to the bank), as well as the aquatic habitat and concluded that the repelling spur dike had the best performance in their experiments. Giri and Shimizu (Giri and Shimizu, 2004) also assessed the vegetation impact by planting living vegetation (alfalfa) near spur dikes.

1.2.2. Numerical studies on spur dike

As the works of laboratory experiments are generally huge in both size and cost, as well as with the constantly updated computer equipment, numerical simulation methods have been getting more and more attention and gradually become an important tool in this research area. Recent numerical studies on spur dike are listed in Table 1.2.

A few investigators have employed 3D numerical models to help to give insight into the detailed flow structure around spur dikes due to the difficulties of obtaining a large number of velocity measurements (Han and Lin, 2018; Ouillon and Dartus, 1997; Paik and Sotiropoulos, 2005; Yazdi et al., 2010). Mulahasan et al. (Mulahasan et al., 2021) simulated the flow through a single spur dike made of porous media (gravel and glass beads) by including the porosity in momentum equations and transport equations for k and ε, and the results showed good agreement. Karami et al. (Karami et al., 2014) compared the results of 2 turbulence models and 6 sediment transport formulas with measurements and concluded that $k-\varepsilon$ RNG model matched better than the standard $k-\varepsilon$ model, and the sediment transport formula of van Rijn had best agreement with the experimental results in their cases. The effect of spacing on flow and bed deformation was numerically investigated in both straight channels (Giglou et al., 2017; Ning et al., 2019) and a 90-degree bend (Vaghefi et al., 2016).

Most numerical simulations employed equilibrium sediment transport and ignored the non-equilibrium sediment transport induced by the in-stream structure. Besides, most numerical studies for meandering channels and actual rivers were performed using 2D numerical models (Duan and Nanda, 2006; Elhakeem et al., 2017; Giri et al., 2004; Kafle, 2021; Ma et al., 2020; Yang et al., 2022). Although 2D numerical models are cost-effective, need less input data, and can reasonably predict the structure-induced mean flow properties and turbulent characteristics to some extent, there is no doubt that a 3D hydrodynamic model is essential to simulate the complex flow structure such as separation and vortices generation.

Among the 2D simulations, Elhakeem et al. (Elhakeem et al., 2017) employed a 2D model to help the design of spur dikes, they assessed the overall performance of different arrangements by comparing the simulated velocity and Froude number along the bank with the recommended values for erodible channel stability design to identify the optimal number and spacing. In addition, a few researchers have evaluated the effect of spur dikes on aquatic habitats by computing the weighted useable area (WUA) using the 2D hydrodynamic simulation results (Ma et al., 2020; Yang et al., 2022).

Table 1.2 Numerical studies on spur dike

References	Channel	Spur	Model	Objective
(Ouillon and Dartus, 1997)	Straight; rigid bed	A single spur	3D hydrodynamic model ($k-\varepsilon$, depth-integrated continuity equation for water surface)	Introduction and validation of the model.
(Paik and Sotiropoulos, 2005)	Straight; rigid bed	A single spur	3D simulation (detached eddy simulation (DES) turbulence model)	The 3D flow structure in the recirculating region upstream of the spur.
(Yazdi et al., 2010)	Straight; rigid bed	A single spur (different angles and lengths)	3D simulation (Fluent, $k-\omega$, VOF)	The reattachment length for various flow conditions, flow pattern for different angles, and bed shear stress distribution for different angles and lengths.
(Mulahasan et al., 2021)	Straight; rigid bed	A single spur (made of 2 porous media)	3D simulation (Fluent, $k-\varepsilon$, VOF)	Introduction and validation of the model.
(Giri et al., 2004)	Meandering; rigid bed	A series of spurs	2D model	Introduction and validation of the model.
(Kafle, 2021)	Meandering (5 channels); rigid bed	A single spur	2D simulation (Nays 2D)	The effects of meandering angle on the velocity field and separation zone.
(Tripathi and Pandey, 2021b)	Meandering; rigid bed	A T-shaped spur	3D simulation (Fluent, $k-\varepsilon$ RNG)	The effect of Froude number.
(Han and Lin, 2018)	Natural river; rigid bed	2 spurs	3D model (large eddy simulation (LES), porous medium method (PMM))	The flow characteristics in the spur field with different flowrate.
(Karami et al., 2014)	Straight; movable bed	3 spurs	3D simulation (SSIIM 2.0, equilibrium sediment transport,	Comparison of the standard $k-\varepsilon$ model and $k-\varepsilon$ RNG model, and different

References	Channel	Spur	Model	Objective
			fixed-lid approach for water surface)	bed load transport rate formulas
(Giglou et al., 2017)	Straight; movable bed	A spur and 2 spurs	3D simulation (Flow-3D, the RNG turbulence model, VOF)	The effect of the orientation of a spur and the spacing of 2 spurs in a straight channel on the flow and sedimentation area.
(Ning et al., 2019)	Straight; rigid and movable bed	A series of spurs	3D model (RNG turbulence model, equilibrium sediment transport, VOF)	The effect of spacing on flow field and bed morphology.
(Han et al., 2022)	Straight; movable bed	A single spur; submerged & non-submerged	3D model (LES, equilibrium sediment transport, PMM, PLIC-VOF)	Introduction and validation of the model.
(Vaghefi et al., 2016)	A 90-degree bend; movable bed	2 T-shaped spurs; different spacing; submerged & non-submerged	3D simulation (SSIIM, $k-\varepsilon$, equilibrium sediment transport)	The effect of spacing and submergence on flow and bed deformation.
(Duan and Nanda, 2006)	Actual river	A series of spurs	2D model (suspended load transport)	The flow field and distribution suspended sediment concentration around spurs with different lengths.
(Elhakeem et al., 2017)	Actual river; rigid bed	A series of spurs	2D simulation (FESWMS of SMS)	Enchanting spur design by estimating the velocity and Froude number along the bank.
(Ma et al., 2020)	Actual river	Different numbers (1, 2, 3)	2D hydrodynamic simulation	The impact of spur layouts on aquatic habitats with different flowrate
(Yang et al., 2022)	Actual river	A series of spurs + a dam	2D hydrodynamic simulation	The impact of combining spurs and dam on fish habitat.

1.2.3. Studies on spur dike in our laboratory

As shown in Table 1.3, many previous students in our laboratory have carried out studies related to the spur dike. Experiments for characterizing the flow field and bed deformation have been conducted in straights with spur dikes having different permeabilities (Teraguchi, 2011; Zhang, 2005), submergences (Mansoori, 2014; Mizutani, 2011; Teraguchi, 2011), orientations (Shampa, 2019), as well as head shapes (Mansoori, 2014). Among these studies, Mizutani (Mizutani, 2011) analyzed the particle distribution around a spur dike under different submergence conditions. Mansoori (Mansoori, 2014) analyzed the effect on aquatic habitat improvement. Besides, Some students investigated the flow and sediment transport around Bandal-like structures (Nishio, 2016; Okudaira, 2021; Tai, 2019; Teraguchi, 2011).

Table 1.3 Studies on spur dike by previous students in our laboratory

References	Channel	Spur	Method	Objective
(Zhang, 2005)	Straight; Movable bed	A series of impermeable & permeable spurs were installed on both sides of the channel	Experiment; 1D model; 3D model ($k-\varepsilon$, moving mesh, equilibrium sediment transport, non-uniform sediment with special attention to fine sediment)	Characterizing the flow structure and bed evolution induced by spur dikes and identifying the underlying processes and mechanisms. Introduction of a 1D model and a 3D model, validation of the 3D model through flume experiments under both non-submerged and submerged conditions.
(Mizutani, 2011)	Straight; movable bed; uniform & nonuniform sediment (3 particles)	A single impermeable spur; submerged & non-submerged	Experiment; 3D model ($k-\varepsilon$ Sediment pick-up for bed load, non-uniform sediment)	The local scour, particle distribution around a spur dike under both submerged and non-submerged conditions. Introduction and validation of the 3D model.
(Teraguchi, 2011)	Straight; movable bed	Impermeable spurs, pile-type spurs, and Bandal-like structures; 2 spurs; Submerged & non-submerged	Experiment; 3D model ($k-\varepsilon$, equilibrium sediment transport; Moving mesh)	The characteristics of flow pattern and bed deformation around 3 kinds of spurs under both submerged and non-submerged conditions. Introduction and validation of the 3D model.
(Mansoori, 2014)	Straight; rigid and movable bed	A series of impermeable spurs; Submerged & non-submerged; different head shapes (T-shaped)	Experiment and 3D simulation ($k-\varepsilon$, equilibrium bed load transport, VOF)	The effect of head type, open ratio of spur field, and submergence ratio on flow structure and bed deformation, and aquatic habitat improvement.
(Nishio, 2016)	Straight; rigid and movable bed	A series of Bandal-like structures and impermeable spurs	Experiment; 3D model ($k-\omega$ SST, suspended load transport and sediment pick for bed load, OpenFOAM, moving mesh)	The effect of Bandal-like structures on flow, suspended load concentration, and bed deformation. Introduction and validation of the 3D model.
(Ota et al.,	Straight; movable	A weir-type structure	3D model ($k-\omega$ SST,	Introduction and validation

References	Channel	Spur	Method	Objective
2016b)	bed		suspended load transport and sediment pickup for bed load, OpenFOAM, moving mesh)	of the 3D model for local scour upstream of a weir-type structure.
(Tai, 2019)	Straight; rigid bed with upstream sediment feeding	A single Bandal-like structure	Experiment and 3D simulation ($k-\omega$ SST, suspended load transport and sediment pickup for bed load, OpenFOAM, moving mesh)	The effect of the height of permeable part of Bandal-like structure on suspended load transport.
(Nakamura, 2019)	Meandering; rigid bed and partially erodible bank with upstream sediment feeding	A series of impermeable spurs; 4 orientations	Experiment and 2D hydrodynamic simulation	The flow and bed deformation around spurs.
(Shampa, 2019)	Straight; rigid bed	A series of pile-type spurs; different arrangements (staggered, non-staggered, 3 orientations)	Experiment and 3D hydrodynamic simulation (interFoam, $k-\omega$ SST)	The three-dimensional flow behaviors around a series of pile-type spurs with different arrangements.
(Karki, 2019)	Meandering (2 sinuosities); movable bed and erodible banks	A series of impermeable spurs; different crests	Experiment	The process of bed deformation and ban erosion in meandering, as well as the effect of spur dikes.
	Meandering (2 sinuosities); movable bed	A series of Impermeable and pile-type spurs; 2 positions; 2 orientations	2D simulation (TELEMAC-2D)	The effect of different arrangements of spur dikes.
		A series of Impermeable spurs	3D simulation (TELEMAC-3D, hydrostatic assumption, $k-\varepsilon$)	The 3D flow field.
	Actual river	A series of Impermeable spurs; 2 orientations	2D simulation (TELEMAC-2D) (considering bank erosion in the simulation without spurs)	The channel variations under low and high flow discharges.
(Okudaira, 2021)	Straight; rigid and movable bed	A series of Bandal-like structures; different permeability	3D numerical simulation ($k-\omega$ SST SAS, suspended load transport and sediment pickup for bed load, OpenFOAM, PMM)	The effect of the open ratio of permeable part on flow and bed deformation with considering suspended load transport

In addition to the studies within straight channels, Nakamura (Nakamura, 2019) and

Karki (Karki, 2019) carried out experiments in meanderings with a partially erodible bank or 2 fully erodible banks. Karki (Karki, 2019) also investigated the effect of different arrangements of spur dikes using a 2D model and presented the cross-sectional velocity distribution using a 3D model.

Regarding the numerical studies, a few 3D numerical models were developed and invalidated. Zhang (Zhang, 2005) gave special attention to the fine sediment in his model. Mizutani (Mizutani, 2011) proposed a 3D model considering non-uniform sediment transport. In some of them, the non-equilibrium sediment transport induced by spur dikes was considered by computing the sediment pickup rate and tracking the sediment movement using a Lagrangian method (Mizutani, 2011; Nishio, 2016; Okudaira, 2021; Ota et al., 2016b; Tai, 2019).

1.3. Research gaps and objectives of the present study

The most characteristic features of natural streams, regardless of size, are the absence of long straight reaches and the presence of frequent meanders (Leopold and Langbein, 1966). The meanders induce complex flow structures such as cross-circulation. The erosion-deposition zones and convergence-divergence flow zones alternate periodically along the meandering channels, and their locations are rather strongly dependent on channel sinuosity (da Silva and Yalin, 2017). Due to the migration of their locations with channel sinuosity, a spur dike at the same location in meandering channels with different sinuosities or at different positions in the same meandering channel can result in different collision angles with the flow, increasing the randomness of bed deformation. In a word, the flow and sediment transport around spur dikes in meandering channels are influenced by not only the arrangement of spur dikes but also the sinuosity of meandering channels.

Bank erosion is a predominant river morphodynamic process, leading to channel migration, the loss of agricultural lands, and damage to hydraulic structures and infrastructure. From the perspective of river management, bank protection structures like spur dikes are necessary to control bank erosion. However, from the standpoint of the river ecosystem, bank erosion can foster riparian vegetation succession and create dynamic habitats that are crucial for aquatic and riparian plants and animals (Florsheim et al., 2008). Consequently, some restoration projects removed bank protection (van der Mark et al., 2012). Therefore, there is a need for reliable and practical 3D numerical models that consider bank erosion to evaluate the performance of spur dikes, guide their design including the effect on aquatic habitat, and assess the morphodynamic response to their removal in restoration projects.

Regarding the design of spur dikes, many recommendations for their layout and design have been proposed (Baird et al., 2015; Brown, 1984; Lagasse et al., 2009; Seed, 1997), which are predominantly grounded in local conditions and preferences. No systematic quantitative design method has existed for crest length, angle, width, and spur spacing for various channel conditions (Baird et al., 2015). The spacing between two adjacent spur dikes is one of the most important considerations in spur dike design. It is a critical parameter to balance the performance of spur dikes and construction costs.

The literature review indicates that the majority of previous works on the flow and sediment transport around spur dikes were performed either in straight flumes or in a single curved channel (meandering channel and bend). Minimal focus is given to the optimum spacing in meandering channels as well as its relationship with channel sinuosity and the location of spur dikes. Besides, there are seldom numerical studies on spur dike considering the modeling of bank erosion.

In this context, we performed the numerical study on flow and sediment transport around spur dikes in meandering channels and actual rivers using a 3D model considering the turbulent flow around spur dikes and in curved channels, as well as bank erosion. This aims to assist in the optimum design of spur dikes.

The objectives of the study are as follows:

(1) To extend the applicability of the existing 3D model in our laboratory to the investigation of flow and sediment transport around spur dikes in meandering channels.

(2) To numerically investigate the effect of the location of a spur dike on the downstream separation zone (affecting spacing) and the local scour, as well as its relationship with the channel sinuosity.

(3) To numerically investigate the spacing and channel sinuosity on flow and bed deformation and to quantify the overall performance of different spacings including consideration of aquatic habitat.

(4) To construct a new solver by incorporating a bank mass failure operator into the 3D model to enable it to simulate bank erosion.

(5) To apply the new solver to a natural river with bank erosion problems and assess the

performance of proposed arrangements of spur dikes.

1.4. Outlines of the dissertation

The present dissertation is organized into 6 chapters as follows:

In Chapter 1, the general background of this research, a brief review of previous studies on spur dike as well as the objectives of this study are presented.

In Chapter 2, the 3D multiphase OpenFOAM solver considering sediment transport is elaborated and validated with experimental data.

In Chapter 3, the 3D solver in Chapter 2 is applied to the investigation of the effect of the location of a single spur dike and the spacing of a series of spur dikes in different meandering channels. An equation for quantifying the overall performance is proposed.

In Chapter 4, a new solver is developed by incorporating a bank mass failure operator into the solver in Chapter 2 and validated with experimental data.

In Chapter 5, the solver in Chapter 4 is used to reproduce a flood event of the Uji River and then, the performance of spur dikes with two kinds of spacings is evaluated.

In Chapter 6, the conclusions of this study and possible recommendations for future research are summarized.

Chapter 2.
3D numerical model for spur dikes in meandering channels

2.1. Introduction

In this chapter, the 3D OpenFOAM solver considering sediment transport originally developed by Ota et al. (Ota et al., 2017), Ota and Sato (Ota and Sato, 2020) and Okudaira (Okudaira, 2021) was elaborated.

The solver was developed based on the interFoam solver in OpenFOAM, which is a two-phase flow solver using the volume of fluid method (VOF) method to distinguish between the two immiscible and incompressible fluids (Mooney et al., 2014). In this new solver, an additional module for sediment transport and bed deformation has been incorporated into the interFoam solver. For bed deformation, the bed surface is not explicitly tracked. Similar to the VOF method, a volume tracking method is used. The bed is treated as a porous medium, and each computational cell is assigned a porosity or sediment volume fraction (excluding suspended sediment concentration). A cell with a porosity of 1 represents a pure fluid cell, a cell with the porosity of pure sediment porosity represents a cell within the bed, and the porosity between them represents the bed surface in that cell. During the calculation, the porosity or sediment volume fraction is updated based on the results of sediment transport and bed deformation calculations. For flow calculation, a porous medium method (PMM) is employed. There is no differentiation between the cells inside and outside the bed, and the same governing equations are used to compute open-channel flow and seepage flow within the bed. The VOF method and PMM allow the use of the fixed mesh to calculate the free water surface and bed deformation. Compared to the body-fitted mesh, the fixed mesh is more suitable for large deformations, such as local scour near in-stream structures. Additionally, it is easier to ensure good mesh orthogonality at complex topography.

The model has been applied to the study on flow and sediment transport around in-stream structures in straight channels by Ota et al. (Ota et al., 2017) (using a different turbulence model), Ota and Sato (Ota and Sato, 2020) (excluding the suspended load transport) and Okudaira (Okudaira, 2021). Towards the end of the chapter, the applicability of the model was extended to the investigation of flow and sediment transport around spur dikes in meandering channels through validation using published data from two experiments, one for flow filed in a U-shaped channel and the other for bed deformation in a meandering channel.

2.2. Hydrodynamic model

2.2.1. Governing equations

The motion of incompressible air-water flow was described by a modified Navier–Stokes equations that consider seepage flow in the bed, which is treated as a porous medium. The treatment of temporal and spatial gradient of the computational cell porosity m follows the method of Nakamura and Mizutani (Nakamura and Mizutani, 2013), where the sediment transport induced by the tsunami was simulated.

Combined with the form used in the interFoam solver of OpenFOAM (Damian, 2012), the governing equations are rearranged as follows (to match the form actually used in the code, the density is kept):

$$\frac{\partial}{\partial x_j}\left(m\rho u_j\right) = 0 \tag{2.1}$$

$$m\frac{\partial \rho u_i}{\partial t} + \frac{\partial}{\partial x_j}\left(m\rho u_i u_j\right) - \frac{\partial}{\partial x_j}\left[m(\mu + \mu_t)\frac{\partial u_i}{\partial x_j}\right] - \frac{\partial u_j}{\partial x_i}\frac{\partial[m(\mu+\mu_t)]}{\partial x_j}$$
$$= -m\frac{\partial p_d}{\partial x_i} - mg_j x_j\frac{\partial \rho}{\partial x_i} + mf_i^s - mR_i \tag{2.2}$$

where, u_j is the fluid velocity; ρ is the fluid density; p_d is the modified pressure; g_j is the gravitational acceleration; μ is the dynamic viscosity; μ_t is the turbulent viscosity; m is the volume fraction of the void space in each cell, i.e., porosity; f_i^σ is the surface tension force; R_i is the resistance force due to porous media.

For cases where the hydrostatic pressure contribution, $\rho g_j x_j$, is important, e.g., for buoyant and multiphase cases, it is numerically convenient to solve for an alternative modified pressure defined by:

$$p_d = p - \rho g_j x_j \tag{2.3}$$

where, p is the pressure.

In OpenFOAM solver applications, the original pressure p is replaced by this modified pressure in the momentum equation to simplify the definition of boundary conditions.

The surface tension force at the air-water interface is evaluated per unit volume using the continuum surface force (CSF) model (Brackbill et al., 1992).

$$f^{s}{}_{i} = \sigma\kappa\frac{\partial\alpha}{\partial x_i} \tag{2.4}$$

where, σ is the surface tension coefficient; α is the volume fraction of water; κ is the mean curvature of the free surface, determined from the expressions:

$$\kappa = \nabla\cdot\left(\frac{\nabla\alpha}{|\nabla\alpha|}\right) \tag{2.5}$$

Regarding the resistance due to porous media, in the work of Nakamura et al. (Nakamura and Mizutani, 2013), laminar and turbulent resistance was included as follows:

$$R_i = \frac{12C_{D2}\mu(1-m)}{md^2}u_i + \frac{C_{D1}\rho(1-m)}{2md}u_i\sqrt{u_j u_j} \tag{2.6}$$

where, d is the median grain size of sand particles composing porous media; C_{D1} is the turbulent drag coefficient, 0.45; C_{D2} is the laminar drag coefficient, 25.0.

However, the above equation for the resistance comes from the Morison-type equation for evaluating the wave forces on a spherical armor unit (Mizutani et al., 1996), originally developed for the interaction between a submerged breakwater and waves. Considering the different conditions in the riverbed, another method will be used for the resistance force. In many works (Burcharth and Andersen, 1995; del Jesus et al., 2012; Higuera, 2015; Liu et al., 1999; Van Gent, 1995), the total resistance for flow through a porous medium was calculated using the extended Forchheimer equation, which was enriched based on Darcy's law.

$$I_i = au_i + bu_i\sqrt{u_j u_j} + c\frac{\partial u_i}{\partial t} \tag{2.7}$$

where, a, b, c are coefficients; I_i is the hydraulic gradient.

In this equation, three contributions are contained, namely the resistance due to laminar and turbulent flow and the inertial resistance. However, when the porosity of the medium is small, e.g., sand, the small-scale turbulence inside the medium could be indeed very weak, turbulence is negligible, and porous flow is dominated by laminar resistance (Hsu et al., 2002). As a result, only the linear term in equation (2.7) accounting for laminar effects is included as follows (Burcharth and Andersen, 1995; del Jesus et al., 2012):

$$R_i = -\alpha\frac{\mu(1-m)^3}{m^2d^2}u_i \tag{2.8}$$

where, α is an empirical parameter used in the calibration of the numerical model; d is the median diameter of bed sediment.

2.2.2. Free surface methodology

The air-water interface motion was solved by a volume tracking method, the volume of fluid (VOF) method. The VOF method devised by Hirt and Nichols (Hirt and Nichols, 1981) remains one of the most versatile and robust techniques available (Katopodes, 2019). In this method, two immiscible fluids, air and water, in this study, are treated as one effective fluid throughout the whole simulation domain, whose local physical properties are calculated as weighted averages based on the volume fraction α, for example,

$$\rho = \alpha\rho_w + (1-\alpha)\rho_a \tag{2.9}$$

$$\mu = \alpha\mu_w + (1-\alpha)\mu_a \tag{2.10}$$

$$u_i = \alpha u_{i_w} + (1-\alpha)u_{i_a} \tag{2.11}$$

where, subscript w and a denote water and air, respectively. The density ρ and dynamic viscosity μ only vary across the interface.

The transport equation of the volume fraction used in the interFoam solver can be expressed as (Damian, 2012):

$$\frac{\partial\alpha}{\partial t} + \frac{\partial(\alpha u_i)}{\partial x_i} + \frac{\partial}{\partial x_i}\left[u_{r_i}\alpha(1-\alpha)\right] = 0 \tag{2.12}$$

where, u_{r_i} is the compression velocity.

$$u_{r_i} = u_{i_w} - u_{i_a} \tag{2.13}$$

Compared to the standard phase fraction function, equation (2.12) contains an extra term, referred to as the compression term. This convective term only exists within the interface cells and disappears at the regions occupied by one phase. It is an artificial term and has no meaning in the phase fraction function, but it is suitable to compress the interface in the discrete formulation and contributes significantly to a higher interface resolution, especially when the interface is not sharp enough, thus avoiding the need to devise a special scheme for convection (Damian, 2012).

2.2.3. Turbulence closure

As to the turbulence effect, the numeric simulation of turbulence is highly complex and still the subject of ongoing research (Rowiński and Radecki-Pawlik, 2015). As presented in Figure 2.1, there are mainly three turbulence simulation types that are used in hydraulic engineering practices: 1) direct numerical simulation (DNS), 2) large eddy simulation (LES), and 3) Reynolds-averaged Navier-Stokes (RANS). Among these methods, the RANS approach focuses attention on the mean flow and the effects of turbulence on mean flow properties, the computing resources required for reasonably accurate flow computations are modest, so this approach has been the mainstay of engineering flow calculations over the past several decades (Versteeg and Malalasekera, 2007).

In the RANS group, the $k-\varepsilon$ model and $k-\omega$ model are the most commonly used

	Model		Strength	Weakness	
Increasing Complexity; RANS	0-equation	Eddie viscosity ν_T	Economical, fast calculation, Good for flow dominated by simple boundary layer turbulence where turbulence length and velocity scales are known, such as in shallow rivers, where turbulence is primarily generated by the streambed	Do not account for turbulence history and transport. Provide good predictions of water surface elevation and vertically averaged velocity magnitude in rivers with large width:depth ratio (larger than 5) (Nuze *et al.*, 1993) but away from confluences. Inadequate where there are multiple turbulence length scales, flows with separations and circulations.	Isotropic turbulence
	1-equation Spalart-Allmaras, Prandtl, Baldwin-Barth	Solve 1 extra PDE (advection dispersion) for ν_T	Economical, flow with mild separation	Inadequate for flow with moderate and high separation	
	2-equation 2 extra PDE, 1 for k and one for ε or ω	k–ε standard	Simple, good for many simple flows	Poor for circulation, eddy, and for flow with strong separation and with high strain	
		k–ε RNG	Improved for moderate flow separation swirl and secondary flow. Applied in river modelling	Problems linked to isotropic turbulence and in estimating round jet flows	
		k–ε Realizable	Like k–ε RNG but better for round jet flows	Problems linked to isotropic turbulence	
		k–ω Standard	Simple, good for many simple flows	Poor for circulation, eddy, and for flow with strong separation and with high strain and free surface	
		SST k–ω	As k–ω but less sensitive to inlet free surface boundary, shows promising application in river modelling	Resolved the problem of free surface of the standard k–ω and improved description of circulation of eddy	
	RSM	7 additional equations	Anisotropic turbulence	High CPU effort	Anisotropic turbulence
NS	LES		Solve the turbulence at the large scale and parameterize it at the sub-grid level	Very high CPU effort	
NS	DNS		Solve directly the NS and continuity equation	Extremely high CPU effort	

Figure 2.1 Turbulence models (source: (Tonina et al., 2013))

two models. The $k-\varepsilon$ model performs particularly well in confined flows where the Reynolds shear stresses are most important, its results are much less sensitive to the arbitrary or assumed values in the free stream, but its near-wall performance is unsatisfactory for the boundary layer with adverse pressure gradient (Menter, 1992). While, the $k-\omega$ model has improved wall shear stress, but its solution has strong sensitivity to the free stream value for ω outside the boundary layer (Menter and Esch, 2001). Menter (Menter, 1994) proposed a hybrid model, $k-\omega$ SST (shear stress transport) model, which is a combination of the $k-\omega$ model near the wall and the $k-\varepsilon$ model away from the wall. The SST model shows promising application in river modelling due to its features. As mentioned by Ota et al. (Ota et al., 2016a), since the local scour phenomenon is mainly caused by inverse pressure gradient around hydraulic structures, the $k-\omega$ SST model has often been applied to simulate this phenomenon. After that, Menter and Egorov (Menter and Egorov, 2005) added an additional production term, the SAS (Scale Adapted Simulation) term, into the ω equation. Though not strictly designated as a hybrid RANS-LES method (Walters et al., 2013), the SAS method shows a behavior similar to DES (Detached Eddy Simulation) but avoids some of the issues related to grid sensitivities of that methodology. It allows the model to adjust to the mesh and time step resolution provided, resulting in a continuous variation of the simulation from LES to steady-state RANS (Menter, 2009).

The $k-\omega$ SST SAS model used in the current study is given here (Menter, 2009; Menter and Esch, 2001):

$$\frac{\partial \rho k}{\partial t}+\frac{\partial(\rho u_j k)}{\partial x_j}=\widetilde{P_k}-\beta^*\rho\omega k+\frac{\partial}{\partial x_j}\left[(\mu+\sigma_k\mu_t)\frac{\partial k}{\partial x_j}\right] \tag{2.14}$$

$$\frac{\partial \rho\omega}{\partial t}+\frac{\partial(\rho u_j \omega)}{\partial x_j}=\frac{\gamma}{\nu_t}\widetilde{P_k}-\beta\rho\omega^2+\frac{\partial}{\partial x_j}\left[(\mu+\sigma_\omega\mu_t)\frac{\partial \omega}{\partial x_j}\right]+2(1-F_1)\frac{\rho\sigma_{\omega 2}}{\omega}\frac{\partial k}{\partial x_j}\frac{\partial \omega}{\partial x_j}+Q_{SAS} \quad 2.15)$$

$$\nu_t=\frac{a_1 k}{\max(a_1\omega, S\cdot F_2)} \tag{2.16}$$

$$\widetilde{P_k}=\min(P_k, 10\beta^*\rho k\omega) \tag{2.17}$$

with

$$S=\sqrt{2S_{ij}S_{ij}},\ S_{ij}=\frac{1}{2}\left(\frac{\partial u_i}{\partial x_j}+\frac{\partial u_j}{\partial x_i}\right)$$

$$P_k=\tau_{ij}\frac{\partial u_i}{\partial x_j},\ \tau_{ij}=-\rho\overline{u_i' u_j'}=\mu_t\left(\frac{\partial u_i}{\partial x_j}+\frac{\partial u_j}{\partial x_i}\right)-\frac{2}{3}\rho k\delta_{ij}$$

$$F_1=\tanh(\arg_1{}^4),\ \arg_1=\min\left(\max\left(\frac{\sqrt{k}}{\beta^*\omega y},\frac{500\nu}{y^2\omega}\right),\frac{4\rho\sigma_{\omega 2}k}{CD_{k\omega}y^2}\right)$$

$$F_2=\tanh(\arg_2{}^2),\ \arg_2=\max\left(\frac{2\sqrt{k}}{\beta^*\omega y},\frac{500\nu}{y^2\omega}\right)$$

$$CD_{k\omega}=\max\left(2\rho\sigma_{\omega 2}\frac{1}{\omega}\frac{\partial k}{\partial x_j}\frac{\partial \omega}{\partial x_j},10^{-10}\right)$$

where, k is the turbulence kinetic energy per unit mass, $\frac{1}{2}\overline{u_i' u_i'}$ (prime indicates fluctuating components); ω is the turbulence frequency (dissipation rate of turbulence kinetic energy); P_k is the production rate of k; ν_t is the turbulent kinematic viscosity; τ_{ij} is the Reynolds stress tensor; δ_{ij} is the Kronecker delta ($\delta_{ij}=1$, if $i=j$ and $\delta_{ij}=0$, if $i\neq j$); S_{ij} is the mean strain rate of a fluid element; S is the scalar measure of the strain rate; y is the distance to the nearest wall; F_1, F_2 are blending functions, which are equal to zero at the wall (switch to the $k-\omega$ model) and tend to one in the far field (activate the $k-\varepsilon$ model), realizing a smooth combination of the good near-wall behavior of the former one and the robustness of the later one in the far field. β^*, a_1, are constants, $\beta^*=0.09$, $a_1=0.31$. All other constant coefficients are functions of F_1 by a blending form of the corresponding coefficients of the two models, for example, $\beta=F_1\beta_1+(1-F_1)\beta_2$. The coefficients are:

$\sigma_{k1}=0.85,\ \sigma_{\omega 1}=0.5,\ \beta_1=0.075,\ \gamma_1=5/9$

$\sigma_{k2}=1.0,\ \sigma_{\omega 2}=0.856,\ \beta_2=0.828,\ \gamma_2=0.44$

There are two limiters in this model, equation (2.16) and equation (2.17), one for turbulent viscosity to give improved performance in flows with adverse pressure gradients and wake regions, the other for production rate of turbulence kinetic energy to prevent the build-up of turbulence in stagnation regions.

The SAS concept is based on the introduction of the von Karman length scale into the turbulence scale equation. This source term is given by (Egorov and Menter, 2008):

$$Q_{SAS}=\rho\max\left(\zeta_2\kappa S^2\sqrt{\frac{L}{L_{vk}}}-C_c\frac{2k}{\sigma_\Phi}\max\left(\frac{1}{\omega^2}\frac{\partial\omega}{\partial x_j}\frac{\partial\omega}{\partial x_j},\frac{1}{k^2}\frac{\partial k}{\partial x_j}\frac{\partial k}{\partial x_j}\right),0\right) \tag{2.18}$$

with

$$L=\frac{\sqrt{k}}{\beta^{*1/4}\omega}$$

$$L_{vk}=\max\left(\frac{\kappa S}{|\nabla^2\mathbf{u}|},C_S\sqrt{\frac{\kappa\zeta_2}{\frac{\beta}{\beta^*}-\gamma}}\Delta\right),\ \ \Delta={\Omega_{CV}}^{1/3}$$

where, L is the length scale of the modeled turbulence; L_{vk} is the von Karman length scale; Δ is the grid cell size, which is calculated as the cubic root of the control volume size Ω_{CV}; ζ_2, κ, C_c, σ_Φ, C_S are constants ($=3.51, 0.41, 2, 2/3, 0.11$, respectively).

2.2.3.1. Boundary conditions for bed surface

Since the porous media method is employed, sediment cells and fluid cells are treated equally, and the bed surface is not explicitly identified as a physical boundary in OpenFOAM. This is not an issue for the velocity, as the resistance term due to porous media in equation (2.2) could control the velocity in sediment cells within a reasonable range. Hoverer, for variables related to turbulence, i.e., k, ω and ν_t, boundary conditions for the bed surface need to be set manually.

The direct-wall boundary conditions for k and ν_t are (Robertson et al., 2015):

$$k = 0,\ \nu_t = 0 \tag{2.19}$$

Taking into account what was mentioned earlier, turbulence is negligible when low porosity media are present, such as sand, and considering that $k = 0$ can lead to computational instability, the values of k for the cells below the bed surface and the bed surface itself are set to a very small value, which is the default lower allowable limit for k in OpenFOAM, i.e.,

$$k = 10^{-20} \tag{2.20}$$

For the assignment of the boundary condition for ω, the automatic near-wall treatment proposed by Menter and Esch (Menter and Esch, 2001) is adopted.

$$\omega_{vis} = \frac{6\nu}{\beta_1 y^2} \tag{2.21}$$

$$\omega_{log} = \frac{k^{1/2}}{{C_\mu}^{1/4}\kappa y} \tag{2.22}$$

where, ω_{vis} is the value computed by the viscous sublayer assumptions; ω_{log} is the value computed by the inertial sublayer assumptions; ν is the kinematic viscosity; C_μ is the empirical constant, 0.09. The final boundary condition for ω is a smooth blending of ω_{vis} and ω_{log} by using a binominal function:

$$\omega = \sqrt{{\omega_{vis}}^2 + {\omega_{log}}^2} \tag{2.23}$$

The concept underlying the automatic near-wall treatment is that this method transitions gradually between a viscous sublayer formulation and wall functions, depending on the grid density.

2.2.3.2. Initial inlet boundary condition

Initial inlet values for k, ω and ν_t are also required. Estimates for k and ω can be found in (Robertson et al., 2015).

$$k_{in} = \frac{5u_\infty}{L} \tag{2.24}$$

$$\omega_{in} = 10^{-6}{u_\infty}^2 \tag{2.25}$$

where, u_∞ is the magnitude of the mean freestream or inflow velocity; L is the length of the computational domain in the streamwise direction. The initial value of ν_t can be obtained from k and ω.

2.3. Sediment transport model

The flow around in-stream structures is complex and varies rapidly, whose sediment transport capacity is affected by complex flow features, such as downward flow, horseshoe vortex, localized pressure gradient, and turbulence intensity. The empirical formulas developed for the sediment transport capacity of gradually varied flows, e.g., equilibrium sediment transport, are not applicable to the local scour case (Wu, 2007).

For considering the non-equilibrium sediment transport around spur dikes, an Eulerian-Lagrangian coupled method proposed by Ota et al.(Ota et al., 2016a) is employed, which was constructed by extending the bed deformation model for bed load transport developed by Nagata et al. (Nagata et al., 2005) to the bed-material load by incorporating the suspended load. The method consists of 1) a Lagrangian model for the bed load component integrating the near-bed grain parcels trajectory and the motion equation, and 2) a suspended load transport model in the Eulerian grid.

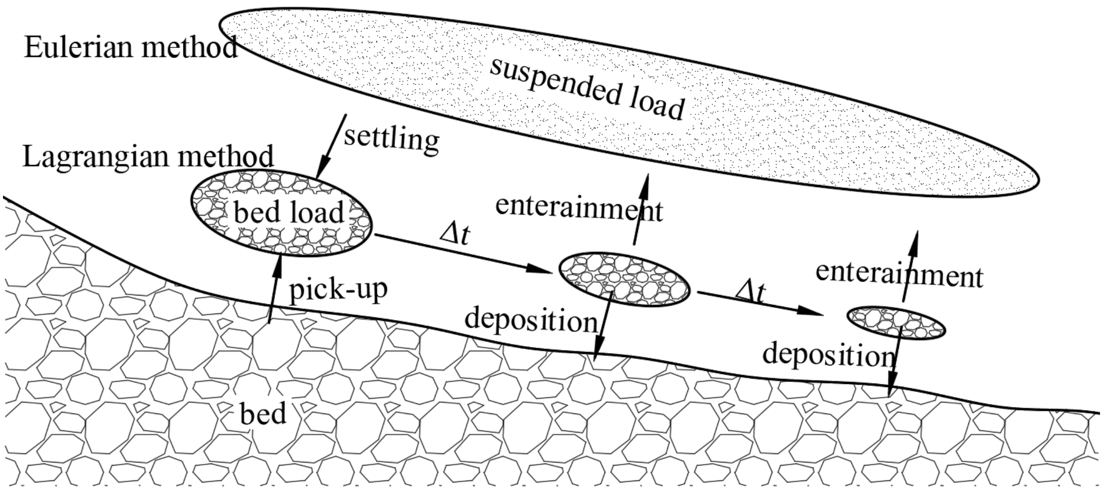

Figure 2.2 Sketch of sediment transport process

The effect of non-equilibrium bed load transport is introduced by calculating the volume of sediment pickup, the trajectory of sediment motion, and the volume of sediment deposition (Nagata et al., 2005). As illustrated schematically in Figure 2.2, the calculation of the sediment transport process starts with the flow picking up sediment particles in a stationary state. The sediment thus picked up, combined with the gravitational settling of the suspended load is regarded as generating a bed load parcel of sediment particles in each computation cell on the bed surface. The movement of each bed load parcel is tracked using a Lagrangian method with the motion equation for a sediment particle. Along the trajectory, some particles of each parcel continue moving, while others may be deposited on the bed or entrained into the suspension due to fluctuating vertical flow, and the parcel gradually disappears. Obviously, the Lagrangian and the Eulerian methods are connected through the sediment exchange between the bed load and the suspended load, as well as between the bed load and the stationary particles on the riverbed.

2.3.1. Sediment pickup

The volume of sediment pickup and the volume of sediment deposition are calculated with a stochastic model of sediment motion. V_p, the volume of sediment pickup per unit time from a numerical cell on the bed surface is given by:

$$V_p = (1-\eta) d p_s S_{bs} \tag{2.26}$$

where, η is the sediment porosity; p_s is the pickup rate; S_{bs} is the slope surface area in a bed surface cell, $S_{bs} = S_{bh}/\cos\theta_b$; S_{bh} is the area of S_{bs} projected onto the horizontal plane; θ_b is the local bed slope angle.

The sediment porosity is obtained using the formula by Wu and Wang (Wu and Wang, 2006). They revalidated the relationship between the initial porosity of sediment deposits and the sediment grain size using laboratory data and field data.

$$\eta = 0.13 + \frac{0.21}{(d+0.002)^{0.21}} \tag{2.27}$$

It should be noted that the median diameter d is in millimeters in the above equation.

The pickup rate p_s is computed from the following equation by Nakagawa et al. (Nakagawa et al., 1986). This equation includes the effect of the local bed slope on the sediment motion and can be used on a steep slope (Nagata et al., 2005).

$$p_s \sqrt{\frac{d}{\left(\frac{\rho_s}{\rho}-1\right)g}} = F_0 G_* \tau_* \left(1 - \frac{k_p \Phi \tau_{*c}}{\tau_*}\right)^{m_p} \tag{2.28}$$

with

$$G_* = \frac{\cos\Psi + k_L \mu_s}{\mu_s}$$

$$\Phi = \left(\frac{\mu_s \cos\theta_b - \sin\theta_b \cos\theta_{bs}}{\cos\Psi + k_L \mu_s}\right) \frac{1+k_L \mu_s}{\mu_s}$$

where, τ_* is the magnitude of dimensionless shear stress, $(= {u_*}^2/((\rho_s/\rho - 1)gd))$; u_* is the bed shear velocity determined using a logarithmic velocity profile; τ_{*c} is the magnitude of dimensionless critical shear stress; G_* is the coefficient of directional deviation between near-bed velocity and sediment movement; Φ is the coefficient of bed slope; F_0, k_p, m_p are constants $(= 0.03, 0.7, 3$, respectively); Ψ is the angle between near-bed velocity and sediment movement; θ_{bs} is the angle between the direction of the maximum local bed slope and the sediment movement; μ_s is the static friction factor ($= 0.7$); k_L is the ratio of lift force to drag force ($= 0.85$); ρ_s is the sediment density; g is the magnitude of gravitational acceleration.

The dimensionless critical shear stress is computed with the formula based on the median grain size proposed by Wu and Wang (Wu and Wang, 1999):

$$\tau_{*c} = \begin{cases} 0.126{D_*}^{-0.44}, & D_* < 0.15 \\ 0.131{D_*}^{-0.55}, & 1.5 \le D_* < 10 \\ 0.0685{D_*}^{-0.27}, & 10 \le D_* < 20 \\ 0.0173{D_*}^{0.19}, & 20 \le D_* < 40 \\ 0.0115{D_*}^{0.30}, & 40 \le D_* < 150 \\ 0.052, & D_* \ge 150 \end{cases} \tag{2.29}$$

with

$$D_* = d\left(\frac{\rho_s-\rho}{\rho}\frac{g}{\nu^2}\right)^{1/3}$$

where, D_* is the dimensionless grain size; ν is the kinematic viscosity.

It should be noted that the above relationship was based on the data in the lower flow regime from stationary flat beds to moving plane beds, and covering the flow discharges of $0.028\sim14260.0\ \mathrm{m^3/s}$, the flow velocities of $0.22\sim2.017\ \mathrm{m/s}$, the flow depths of $0.04\sim13.28\ \mathrm{m}$, the water surface slopes of $0.000026\sim0.0103$, and the sediment median sizes of $0.084\sim22.2\ \mathrm{mm}$ (Wu and Wang, 1999).

2.3.2. Bed load movement

The movement of a sediment particle in a time step is assumed to follow the local bed plane, that is the blue surface in Figure 2.3. As shown in this figure, two unit vectors, $\mathbf{P}_{b1}$ and $\mathbf{P}_{b2}$, are defined on the oxy and ozy planes, respectively. Both of them are parallel to the local bed surface.

$$\mathbf{P}_{b1} = \begin{pmatrix} \cos\theta_{b1} \\ -\sin\theta_{b1} \\ 0 \end{pmatrix} = \begin{pmatrix} \frac{n_y}{\sqrt{{n_x}^2+{n_y}^2}} \\ -\frac{n_x}{\sqrt{{n_x}^2+{n_y}^2}} \\ 0 \end{pmatrix} \tag{2.30}$$

$$\mathbf{P}_{b2} = \begin{pmatrix} 0 \\ -\sin\theta_{b2} \\ \cos\theta_{b2} \end{pmatrix} = \begin{pmatrix} 0 \\ -\frac{n_z}{\sqrt{{n_z}^2+{n_y}^2}} \\ \frac{n_y}{\sqrt{{n_z}^2+{n_y}^2}} \end{pmatrix} \tag{2.31}$$

where, θ_{b1} θ_{b2} are the angles of the local bed plane inclination in the x and z directions, respectively; vector $(n_x,\ n_y,\ n_z)$ is the upward-pointing unit normal vector of the local bed plane.

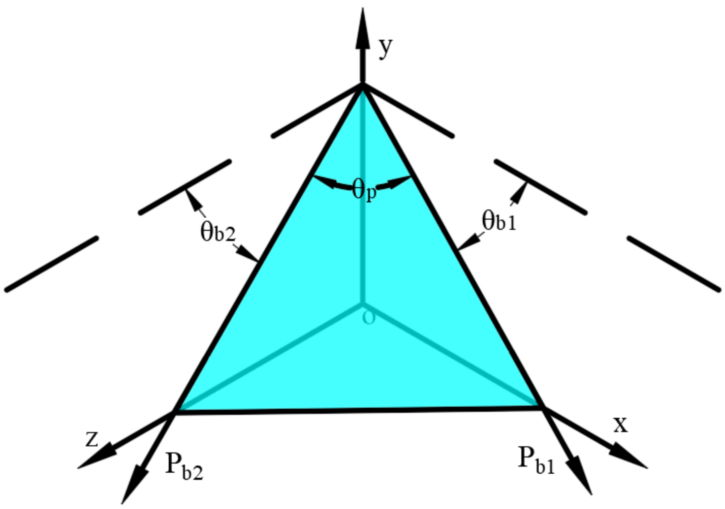

Figure 2.3 Local bed plane for sediment particle movement

Considering the fluid drag, submerged weight, bed friction and added mass, the motion equation of a sediment particle in the $\mathbf{P}_{bj}(j = 1, 2)$ direction is given by (Ota et al., 2017):

$$\rho\left(\frac{\rho_s}{\rho} + C_M\right) A_3 d^3 \frac{\partial u_{sed,j}}{\partial \mathrm{t}} = D_j + W_j - F_j \quad \mathrm{j} = 1{,}2 \tag{2.32}$$

with

$$D_j = \frac{\rho C_D}{2}\sqrt{u_{r,i}u_{r,i}}u_{r,j}c_e A_2 d^2,\ u_{r,j} = u_{b,j} - u_{sed,j}$$

$$W_j = \begin{cases} -W\dfrac{\sin\theta_{b1}\cos^2\theta_{b2}}{\sin^2\theta_p}, & j = 1 \\ -W\dfrac{\sin\theta_{b2}\cos^2\theta_{b1}}{\sin^2\theta_p}, & j = 2 \end{cases},\ W = (\rho_s - \rho)gA_3 d^3$$

$$F_j = \mu_k\left(W\frac{\cos\theta_{b1}\cos\theta_{b2}}{\sin\theta_p} - k_L\sqrt{D_i D_i}\right)\frac{u_{sed,j}}{\sqrt{u_{sed,i}u_{sed,i}}}$$

where, $u_{sed,j}$ is the sediment particle velocity in $\mathbf{P}_{bj}$ direction; C_M is the coefficient of added mass $(= 0.5)$; A_2, A_3 are the shape coefficients of sediment grain for two- and three- dimensional geometrical properties $(= \pi/4,\ \pi/6)$, respectively; D_j is the fluid drag force on a sediment particle; W_j is the submerged weight of sediment particle; F_j is the friction force between sediment particles and the bed; C_D is the drag coefficient $(= 0.4)$; c_e is the coefficient accounting for the effective application area of the drag force

($=1.0$ for moving particles, and $=0.4$ for static particles); $u_{b,j}$ is the near-bed velocity in $\mathbf{P}_{bj}$ direction; θ_p is the angle between $\mathbf{P}_{b1}$ and $\mathbf{P}_{b2}$; μ_k is the coefficient of kinetic friction of sediment particles $(= 0.35)$.

The position vector of a bed load parcel $\mathbf{P}_{sed}{}^{n}$ and its cumulative moving distance $s_{sed}{}^{n}$ at the end of the nth time step after generation, can be computed using the sediment particle velocity vector $\mathbf{u}_{sed}$ obtained from the above equations.

$$\mathbf{P}_{sed}{}^{n} = \mathbf{P}_{sed}{}^{n-1} + \Delta t \mathbf{u}_{sed}{}^{n} \tag{2.33}$$

$$s_{sed}{}^{n} = s_{sed}{}^{n-1} + \Delta t |\mathbf{u}_{sed}{}^{n}| \tag{2.34}$$

where, Δt is the time step for bed load transport calculation; superscript n represents the nth step after the generation of a bed load parcel.

2.3.3. Bed load deposition and entrainment

For a bed load parcel, its deposition volume $V_d{}^{n}$ and the volume of entrainment into the suspension $V_{sus}{}^{n}$ during the time nth time step are calculated by (Okudaira, 2021):

$$V_d^n = V_{b0} F_d^n (1 - F_t^n) \tag{2.35}$$

with

$$V_{b0} = V_p + V_{settle}$$

$$V_{sus}^n = E_s w_s S_{bh} \tag{2.36}$$

where, V_{b0} is the volume of the bed load parcel when generated at the starting point; V_{settle} is the gravitational settlement volume of the suspended load; F_d^n is the probability of a bed load particle being deposited on the bed during the nth time step; F_t^n is the probability of a bed load particle being entrained into suspension during the nth time step; E_s is a dimensionless coefficient describing the entrainment of sediment into suspension due to turbulence; w_s is the settling velocity magnitude of a sediment particle.

The deposition probability F_d^n and entrainment probability F_t^n read (Okudaira, 2021):

$$F_d^n = f_d(s_{sed}^n) \Delta s_{sed}{}^{n} = f_d(s_{sed}^n) \Delta t |\mathbf{u}_{sed}{}^{n}| \tag{2.37}$$

with

$$f_d(s_{sed}^n) = \frac{1}{\max(\Lambda, 1.0e-10)} \exp\left(-\frac{s_{sed}^n}{\max(\Lambda, 1.0e-10)}\right)$$

$$\Lambda = \frac{K_1}{1+\frac{K_2}{\tau_*}} d$$

$$F_t^n = \frac{V_{sus}^n}{V_{b0}(1-F_d^n)} \tag{2.38}$$

where, $f_d(s_{sed}^n)$ is the probability density function of the step length; Λ is the average step length; K_1, K_2 are constants ($= 150, 1$, respectively); Equation (2.38) comes from $V_{sus}^n = V_{b0}(1 - F_d^n)F_t^n$. Based on the Gaussian distribution, the movement distance of each bed load parcel is restricted to 3Λ, and parcels exceeding 3Λ will be fully deposited.

The entrainment coefficient E_s is given by (Garcia and Parker, 1991):

$$E_s = \frac{A{Z_u}^5}{1+\frac{A}{0.3}{Z_u}^5} \tag{2.39}$$

with

$$Z_u = \frac{u_*}{w_s}{R_p}^{0.6},\ R_p = \frac{\sqrt{\left(\frac{\rho_s}{\rho}-1\right)gdd}}{\nu}$$

where, Z_u is a similarity variable for uniform sediment; R_p is the particle Reynolds number; A is a constant $(= 1.3 \times 10^{-7})$.

Wu and Wang (Wu and Wang, 1999) derived the general relation of settling velocity magnitude as:

$$w_s = \frac{M\nu}{N}\left[\sqrt{\frac{1}{4}+\left(\frac{4N}{3M^2}{D_*}^3\right)^{1/n}} - \frac{1}{2}\right]^n \tag{2.40}$$

with

$$M = 53.5e^{-0.65S_f},\ N = 5.65e^{-2.5S_f},\ n = 0.7 + 0.9S_f$$

where, S_f is the Corey shape factor defined as $c/\sqrt{ab}$ (a, b, c are the diameters of a sediment particle in the longest, the intermediate, and the shortest mutually perpendicular axes, respectively). For naturally worn sediment particles, the Corey shape factor is usually about 0.7, and coefficients M, N, and n have values of 33.9, 0.98, and 1.33 respectively.

2.3.4. Suspended load transport

The suspended load transport is calculated by the advection-diffusion equation of sediment concentration as follows (Okudaira, 2021):

$$\frac{\partial C_{sus}}{\partial t} + \frac{\partial}{\partial x_j}\left[\left(u_j + w_s\frac{g_j}{g}\right)C_{sus}\right] = \frac{\partial}{\partial x_j}\left(\frac{\nu+\nu_t}{S_c}\frac{\partial C_{sus}}{\partial x_i}\right) + \frac{V_{sus}-V_{settle}}{V_b} \tag{2.41}$$

$$V_{settle} = w_s C_{s,b} S_{bh} \tag{2.42}$$

where, C_{sus} is the sediment concentration; $C_{s,b}$ is the sediment concentration near the bed; V_b is the volume of the cell near the bed; S_c is the Schmidt number, computed using the formula by van Rijn (for β-factor) (van Rijn, 1984; Wu, 2007):

$$\frac{1}{S_c} = 1 + 2\left(\frac{w_s}{u_*}\right)^2 \quad \text{for } 0.1 < \frac{w_s}{u_*} < 1 \tag{2.43}$$

In the transport equation of sediment concentration, there is a source term accounting for the exchange between bed load parcels and suspended load near the bed boundary. The volume of entrainment, V_{sus}, originally in the Lagrangian frame is converted to the entrainment flux into Eulerian numerical cells adjacent to the bed boundary. In the current calculation, V_{sus} is distributed to the four cells, specifically, the cell where the corresponding bed load particle is located, as well as the cells that are the closest, second closest, and third closest neighboring cells to the bed load parcel. The distribution weights are calculated using the inverse distance weighting method.

2.3.5. Bed deformation

The deposition volume of each bed load parcel and the sediment pickup volume of each bed surface cell at every time step can be computed with the forementioned equations. Then, temporal changes in bed elevation can be obtained from:

$$(1-\eta)\frac{\partial z_b}{\partial t} = \frac{V_d - V_p}{S_{bh}} \tag{2.44}$$

where, z_b is bed elevation.

Similar to the volume of entrainment V_{sus}, the deposition volume V_d in the Lagrangian frame needs to be distributed to four bed surface cells proportionally based on the distance from the deposition location.

Finally, the porosity information of each computational cell can be updated according to the new bed elevation.

2.4. Solutions

2.4.1. Mesh system

By default, OpenFOAM specifies 3D mesh consisting of unrestricted polyhedral cells with arbitrary polygonal boundary faces (Greenshields, 2020). This means that the cells can possess an unlimited number of faces, and for each face, there are no constraints on the number of edges or limitations on their alignment.

To account for the complex boundaries near spur dikes in meandering channels, the unstructured triangular mesh is employed in the horizontal direction. Meanwhile, to facilitate locating the cells containing the bed surface and updating the porosity of each cell during changes in riverbed elevation, the structured mesh is adopted in the vertical direction. Ultimately, the semi-structured triangular prism mesh is used, where the cells are fully overlapped in the vertical direction.

2.4.2. Time step

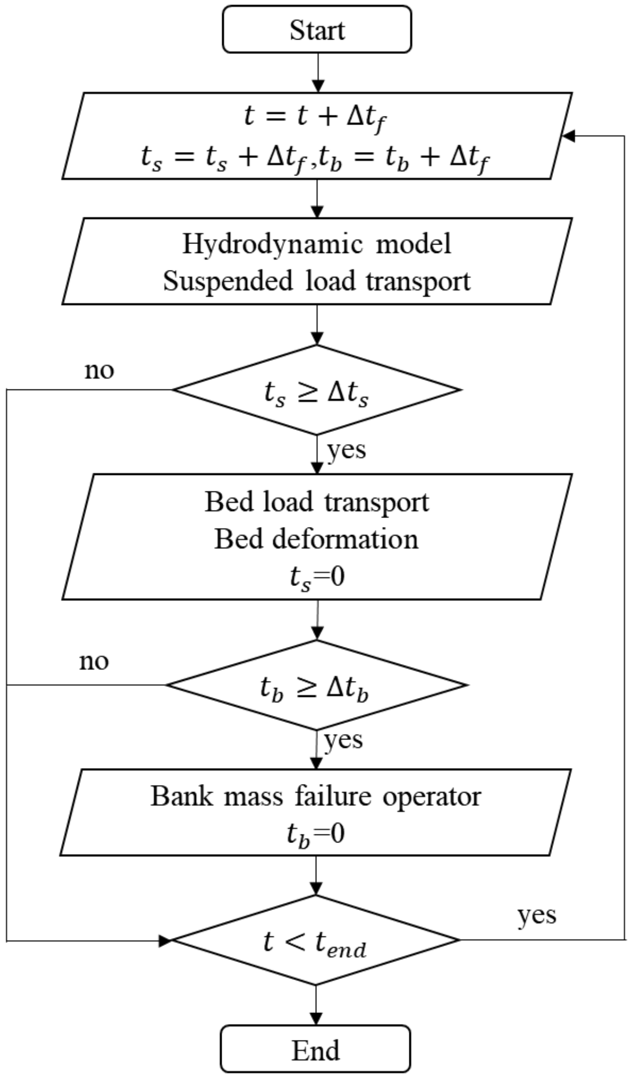

Figure 2.4 Flow chart of the model in this study
(t is the simulation time count; t_s, Δt_s are time count and time step for bed load transport and bed deformation, respectively; t_b, Δt_b are time count and time step for bank mass failure, respectively; Δt_f is the time step for hydrodynamic model and suspended load transport)

In the current Lagrangian method for bed load transport, it is essential to track the trajectory of bed load parcels generated at each time step, recording their positions and velocities until they disappear. Due to the limitation in computational memory, it becomes impractical to record information for all bed load parcels at all time steps (Ota et al., 2016a). On the one hand, to reduce computational memory cost, and on the other hand, also to save the computational time for bed load transport and bed deformation, the hydrodynamic model and suspended load transport use the same time step as presented in Figure 2.4 (the time step for bank mass failure will be explained in Chapter 4). This time step is automatically adjusted according to the maximum global Courant number and the maximum Courant number for the interface of the VOF method. Meanwhile, the bed load transport and bed deformation are carried out using a larger time step to decrease the number of bed load parcels that need to be tracked.

Nicholas (Nicholas, 2013) and Lesser et al. (Lesser et al., 2004) also used decoupled time steps for the hydrodynamic model and morphodynamic model to speed up the simulations and allow the simulations of long timescales of riverbed evolution. However, instead of using different time steps directly, they simply multiply the bed sediment changes by an acceleration factor to extend the morphological time step, where choosing a suitable acceleration factor remains a matter of judgment and sensitivity testing. Unlike that, in this study, the time step of the hydrodynamic model is multiplied by a constant factor as the time step for the bed load transport and bed deformation.

2.4.3. Boundary conditions

Table 2.1 Boundary condition types used in simulations

Physical boundary	Inlet	Outlet	Atmosphere	Sidewall	Bed
α	variableHeightFlowRate	zeroGradient	inletOutlet	zeroGradient	zeroGradient
$\mathbf{u}$	variableHeightFlowRateInletVelocity	zeroGradient or pressureInletOutletVelocity	pressureInletOutletVelocity	noSlip or partialSlip	noSlip or partialSlip
p_d	fixedFluxPressure	waterLevelTotalPressure (derived from totalPressure)	totalPressure	fixedFluxPressure	fixedFluxPressure
k	fixedValue	zeroGradient	inletOutlet	kqRWallFunction	kqRWallFunction
ω	inletOutlet	zeroGradient	inletOutlet	omegaWallFunction	omegaWallFunction
ν_t	fixedValue	calculated	calculated	nutUWallFunction	nutUWallFunction
C_{sus}	uniformFixedValue	inletOutlet	inletOutlet	zeroGradient	zeroGradient

Setting appropriate boundary conditions is vital for the success of a simulation. In the current solver, initial conditions and boundary conditions for the phase fraction α, velocity $\mathbf{u}$, pressure p_d, turbulence kinetic energy k, turbulence frequency ω, turbulent kinematic viscosity ν_t and suspended load concentration C_{sus} are required to be specified. The commonly encountered physical boundaries include inlet, outlet, atmosphere (the open boundary with air), and impermeable wall (bed and sidewall).

OpenFOAM offers a wide range of boundary condition types that can be selected by their keywords. The boundary condition types used in the simulations of this study are listed in Table 2.1 and explained in Table 2.2. More detailed descriptions can be found in its user guide and source code guide documentation (Greenshields, 2020; "OpenFOAM: User Guide," n.d.; "The OpenFOAM Source Code Guide," n.d.)

Table 2.2 Description of boundary condition types

Condition type	Description
$calculated$	The boundary value of a variable is derived from other variables.
$fixedValue$	The boundary value is specified by a value given by the user.
$uniformFixedValue$	It is a $fixedValue$ condition, but the given value can be a function of time.
$totalPressure$	It is a $fixedValue$ condition, giving the pressure calculated from specified total pressure and local velocity.
$zeroGradient$	The normal gradient of variables from a boundary cell center tonto its boundary face is zero. For vector variables, their boundary tangential components are zero.
$inletOutlet$	It switches between $zeroGradient$ condition for outflow and $fixedValue$ for inflow. The inlet value should be specified.
$pressureInletOutletVelocity$	It is a velocity inlet/outlet boundary condition for pressure boundaries, extremely common for boundaries where some inflow occurs, but the inlet value is no known.
$fixedFluxPressure$	It is plied to pressure in scenarios where zeroGradient is commonly used, but body forces like gravity and surface tension force are present. The condition adjusts the gradient accordingly.
$variableHeightFlowRate$	It specifies α according to the local flow conditions. The values are restricted to fall within user-specified upper and lower bounds.
$variableHeightFlowRate$ $InletVelocity$	It provides the mean velocity normal to inlet faces for multiphase flow based on a user-specified volumetric flowrate.
$kqRWallFunction$	It is a simple wrapper around the $zeroGradient$ condition, providing k for the case of high Reynolds number flow using wall functions.
$omegaWallFunction$	It provides a wall constraint on ν_t based on velocity for low- and high-Renolds number turbulence models.
$nutUWallFunction$	It provides a wall constraint on ω for low- and high-Renolds number turbulence models.

The outlet condition type $waterLevelTotalPressure$ for p_d is developed based on $totalPressure$ condition. It provides p_d for boundary faces calculated from the user-specified water level.

$$p_d = \begin{cases} p_0 + \rho g h & \text{for outflow} \\ p_0 + \rho g h - 0.5|\mathbf{u}|^2 & \text{for inflow} \end{cases} \tag{2.45}$$

where, p_0 is the atmospheric pressure, 0; h is the water level at the boundary.

The above equation is used for the case of gravitational acceleration in the vertical direction of the mesh coordinate system. Sometimes, when there is a slight angle between gravitational acceleration and the vertical direction of the mesh coordinate system, the positions of boundary faces need to be taken into consideration.

In addition, for $variableHeightFlowRateInletVelocity$ inlet velocity boundary condition, the velocity magnitudes normal to boundary faces are computed from the user-specified inflow discharge by:

$$U_i = \frac{Q}{\sum_{i=1}^{n}(A_i \alpha_i)} \alpha_i \tag{2.46}$$

where, i is the boundary face label; Q is the inflow volumetric discharge; A is the boundary face area; n is the number of faces of an inlet boundary.

The actual inlet flowrate obtained with velocities from the above equation tends to be underestimated, especially in cases with wide inlet water surfaces and large vertical grid sizes. Therefore, a simple correction has been applied, and the above equation is replaced by the following expression:

$$U_i = \frac{Q}{\sum_{i=1}^{n}(A_i {\alpha_i}^2)} \alpha_i \tag{2.47}$$

2.4.4. Solution schemes

In OpenFOAM, there are a variety of numerical schemes for discretization of temporal terms, convection terms and diffusion terms in all governing equations by simply specifying their keywords in the dictionary file. Detailed descriptions of the schemes can be found in some guides and papers (Greenshields, 2020; Greenshields and Weller, 2022; Robertson et al., 2015).

Considering that second-order schemes are accurate but unbounded and may cause unphysical oscillation, the temporal terms are discretized with the Euler implicit method, which is first-order accurate in time but guarantees the boundedness of the solution. Additionally, the Crank-Nicolson method, using a blending factor to balance accuracy and boundedness, is also an option. When its blending factor is zero, it becomes the Euler method, and when the blending factor is one, it has second-order accuracy.

For the gradient terms, "cellLimited Gauss linear" is specified. The interpolation scheme is determined by the keyword "linear", indicating second-order linear interpolation or central differencing. The keyword "Gauss" means the standard finite volume discretization with Gaussian integration, necessitating the interpolation of values from cell centers to face centers. The "cellLimited" method is used to enhance the boundedness and stability, which restricts the calculated face gradient values from exceeding those of the surrounding cells by specifying a limiting coefficient.

The divergence terms are discretized using “Gauss linearUpwind”, which is second order, upwind-biased, and much less unbounded than the linear scheme, except for phase fraction α using the TVD (van Leer) scheme with an interface compression method (“Gauss interfaceCompression vanLeer”). However, sometimes the divergence terms of k and ω are discretized with the first-order upwind scheme to improve boundedness and stability. After all, turbulence is a diffusive process so using a first-order accurate discretization method for the turbulence variables is acceptable.

Concerning the Laplacian terms, the “Gauss linear corrected” scheme is selected. This scheme is utilized for grids with grading and non-orthogonality, providing second-order accuracy and bounded performance depending on the grid quality. Besides, the numerical scheme for the surface normal gradient terms is also required to be specified, typically using the same method as chosen for the Laplacian terms, i.e., “corrected” in this study.

The pressure-velocity coupling procedure for transient flow calculations, the PISO (Pressure-Implicit with Splitting of Operators) algorithm originally proposed by Issa (Issa, 1986), is employed to solve the governing equations of the hydrodynamic model. The implementation of this pressure-velocity treatment in OpenFOAM is based on the detailed elaboration in Jasak (Jasak, 1996). It divides the solving process into three stages:

1) Momentum predictor: at this stage, the pressure field from the preceding time step is utilized to solve the momentum equation first, yielding an estimate of the new velocity field, that is, the predicted velocities.

2) Pressure solution: use the predicted velocities to solve the pressure equation, which is assembled from governing equations and give the estimate of the new pressure field.

3) Explicit velocity correction: update the velocity field based on the new pressure field obtained at the second step in an explicit manner.

2.5. Model validation

Since in the next chapter, the model would be used for numerical simulations of the flow field and sediment transport around spur dikes in meandering channels, it was necessary to validate its applicability for such cases through observed data before application.

Ota et al. (Ota et al., 2017) have well reproduced the erosion and deposition around both impermeable and partially permeable (Bandal-like) spur dikes in a straight flume with the same porous media method, VOF method, and Eulerian-Lagrangian sediment transport model but Large Eddy Simulation (LES) model for turbulence. Ota and Sato (Ota and Sato, 2020) have applied the SAS model to the study of lateral diversion with vanes, successfully achieving a reasonable resolution of coherent turbulence structures. Okudaira (Okudaira, 2021) has utilized the model in the study on the effect of permeability of the Bandal-like structure on bed deformation in a straight flume. Hence, at present, it can be concluded that the model can be used to analyze the flow and sediment transport around spur dikes in straight channels.

On this basis, this section extended the applicability of the model to the simulations of flow and sediment transport in meandering channels. The extension was validated using published data from two experiments, one for the flow filed in a bend and the other for the bed deformation in a meandering channel.

2.5.1. U-shaped flume case for flow field

(1) Case setup

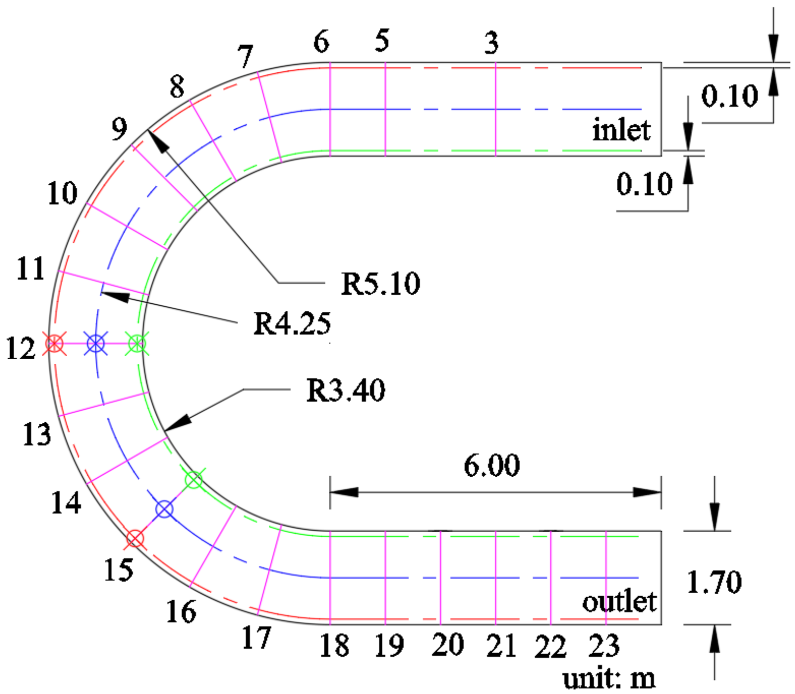

Figure 2.5 Experimental channel outline and cross-section locations

The experimental data of de Vriend (de Vriend, 1979) was used to validate the model's performance for flow field in curved channels. As illustrated in Figure 2.5, it was a 1.7 m wide U-shaped channel with a horizontal bottom and vertical sidewalls. The upstream and downstream straight reaches had a length of 6 m. In the bend, the radius of curvature of the flume axis was 4.25 m. The experiment was carried out with a steady inflow of 0.189 m^3/s and a constant outlet water level of 0.1876 m.

(2) Results

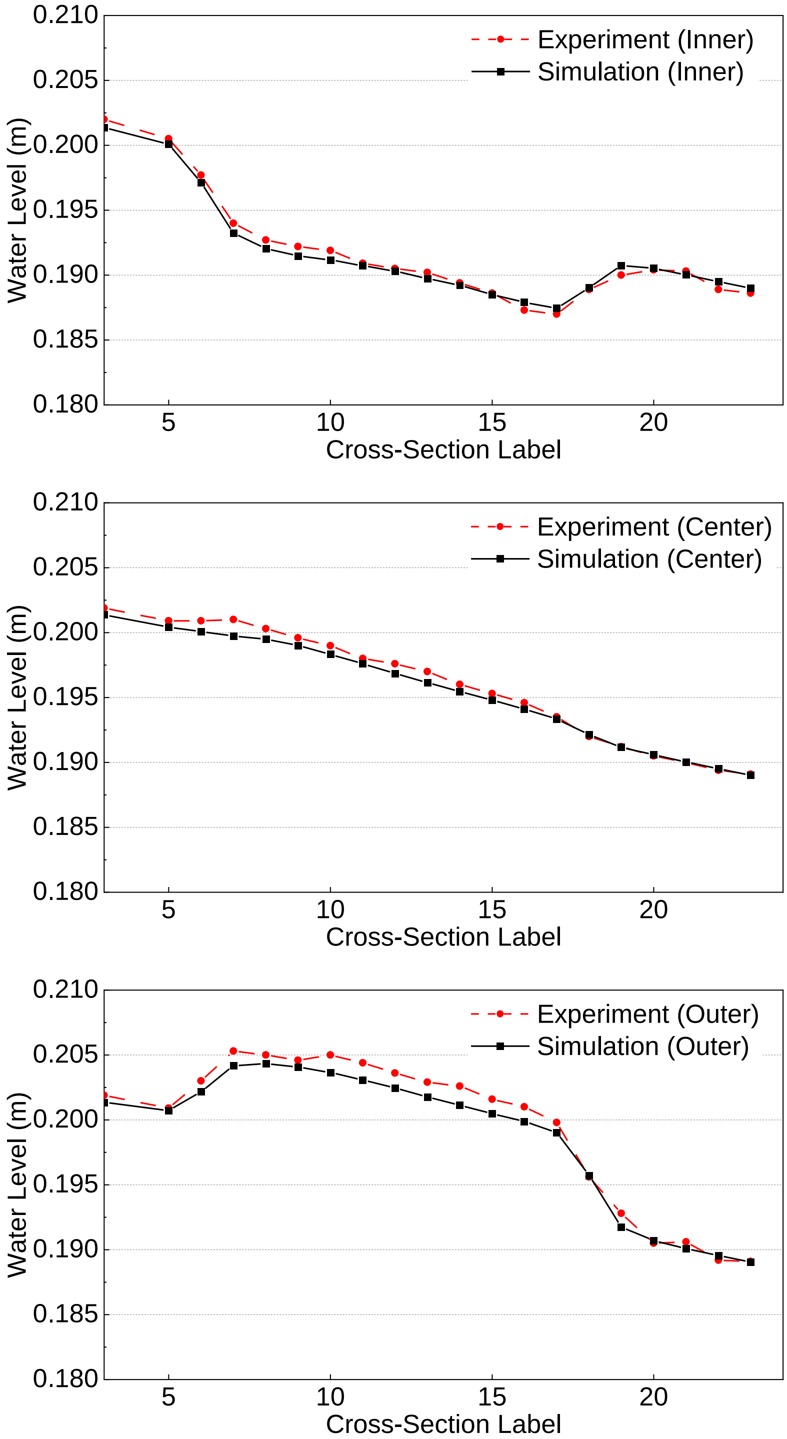

Figure 2.6 Comparison of the water levels

For comparing the observed and the simulated results, 20 cross-sections (CS3, CS5-CS23) along the channel were considered as shown in Figure 2.5. At each cross-section, water levels at three positions were compared. The three positions were close to the inner bank, at the center, and close to the outer bank, marked by green, blue, and red, respectively, where the inner and outer positions were 10 cm away from the sidewalls. The comparison between simulated water levels and measured water levels along the green line, blue line, and red line in Figure 2.5 was plotted in Figure 2.6. We can see that the simulated water levels aligned well with the observed water levels of the experiment, with only slight underestimation in some areas, especially along the line near the outer bank. This might be attributed to that the bed and bank friction could not be exactly determined.

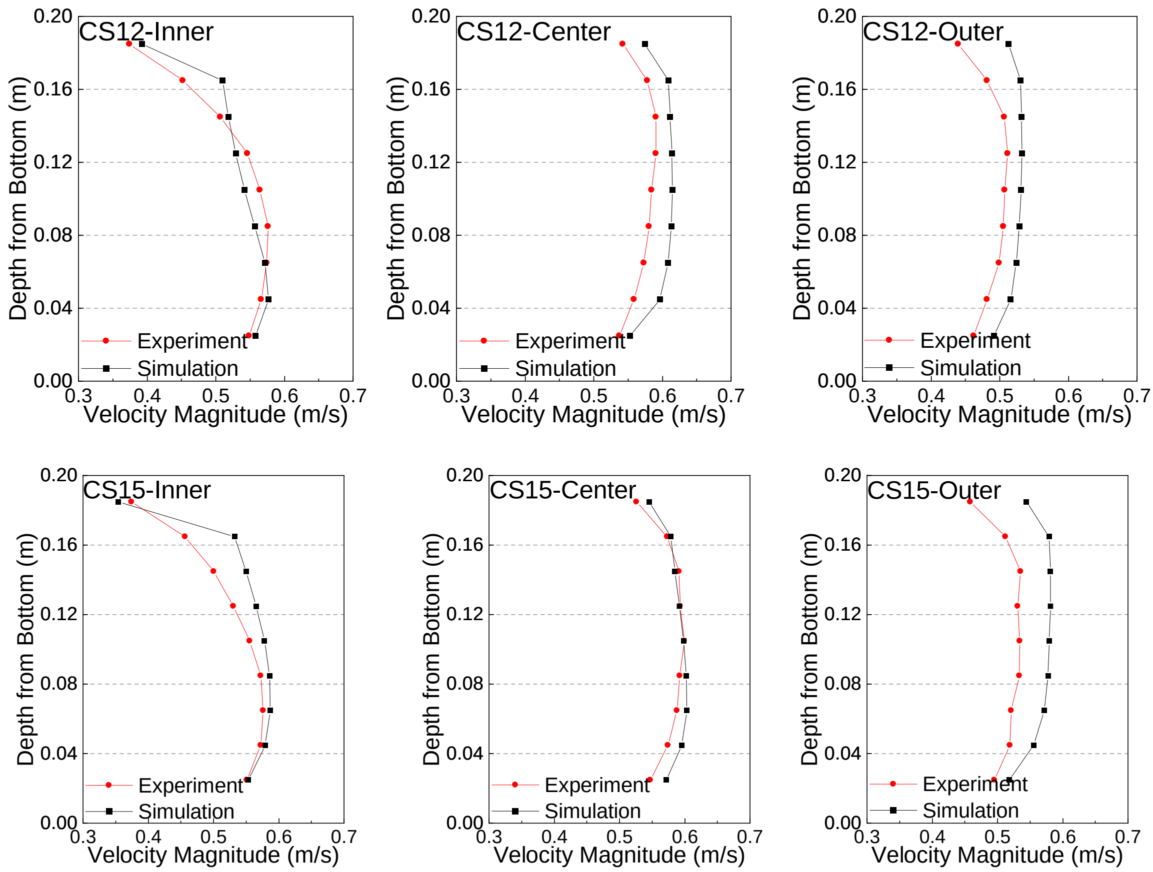

Figure 2.7 Comparison of the velocity distribution along depth at CS12 and CS15

Regarding the flow velocity comparison, two representative cross-sections, CS12 located at the apex of the bend, and CS15 located halfway between the apex and end of the bend, were selected. Similarly, the vertical velocity distribution along depth at three positions, inner, center, and outer points, was compared, and the results were depicted in Figure 2.7. The simulated velocity distribution has matched the shape of the observed velocity distribution. At the inner position of the two cross-sections and the center position of the CS15, they were almost identical, although, at the outer positions of both and the center position of CS12, there was a slight overestimation, which was consistent with the underestimation of water level along the line close to the outer sidewall. This is likely due to the difficulty of perfectly matching the boundary friction conditions of the simulation with the experiment.

Overall, the model has reasonably reproduced the experimental observations.

2.5.2. Meandering channel case for bed deformation

(1) Case setup

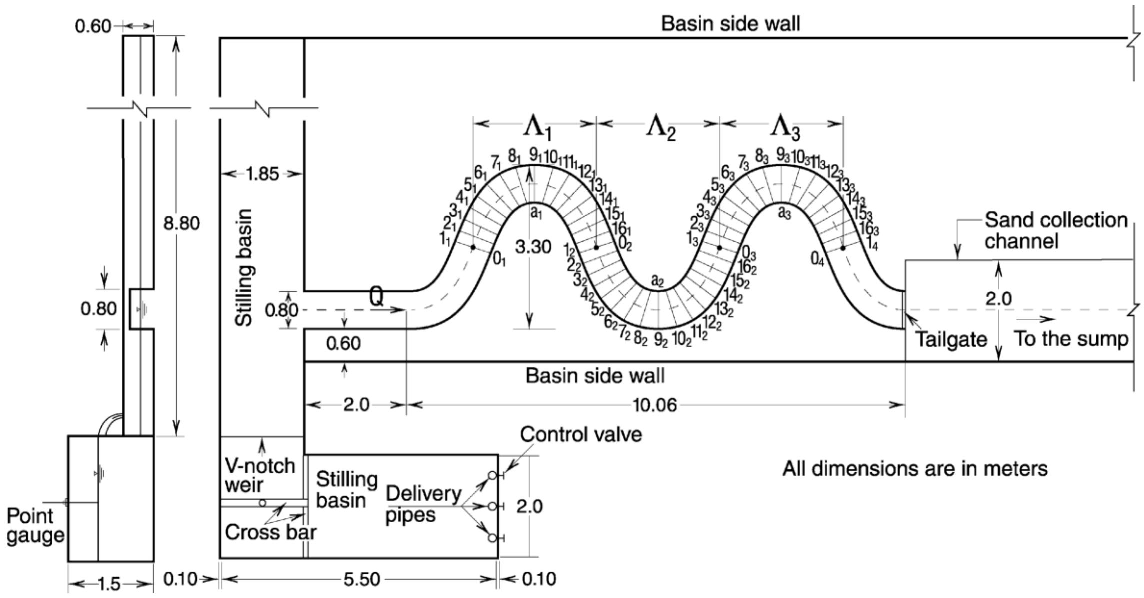

Figure 2.8 Experimental meandering channel of (source: (da Silva and El-Tahawy, 2008))

A series of movable bed experiments in a meandering channel have been conducted to investigate the distributions of flow plan and erosion-deposition zones under different conditions by da Silva and El-Tahawy (da Silva and El-Tahawy, 2008). Among their experimental runs, run 1 was chosen to validate the model applicability in the bed deformation of meandering channels. The plan view of the experimental channel is depicted in Figure 2.8. it was a sine-generated meandering channel with a maximum deflection angle of 70°. The channel had vertical rigid sidewalls with a channel width of 80 cm. There was a 2 m long straight approach channel at the upstream end. The initial flat bed consisted of well-sorted silica sand with a median grain size of 0.65 mm and a specific density of 2.65. For run 1, the initial bed slope is 1:450. This case was conducted with an average water depth of 7.5 cm and a constant discharge of 11.0 l/s, concluding after 75 min.

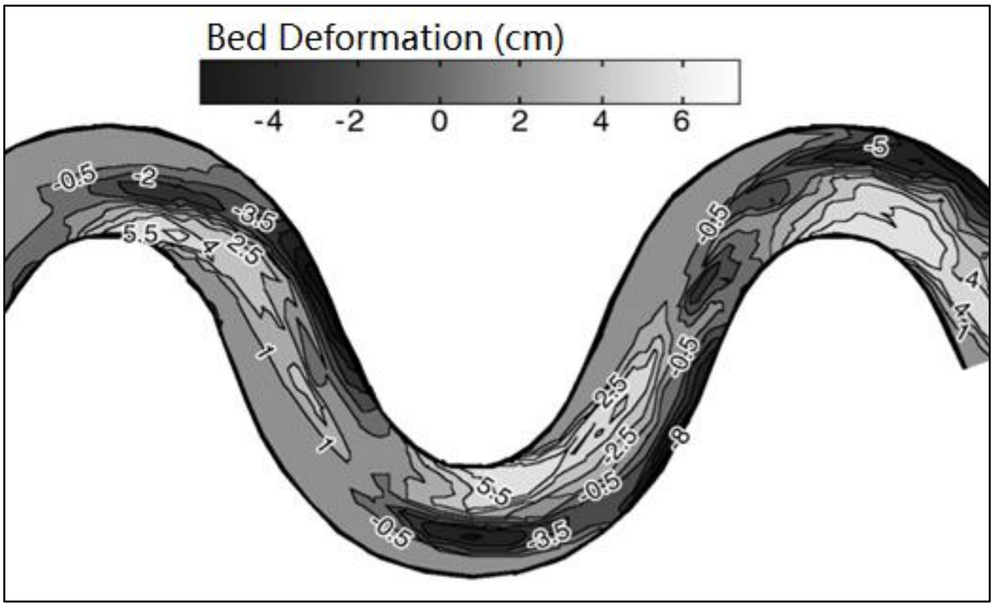

Figure 2.9 Experimental bed deformation contour (source: (da Silva and El-Tahawy, 2008)))

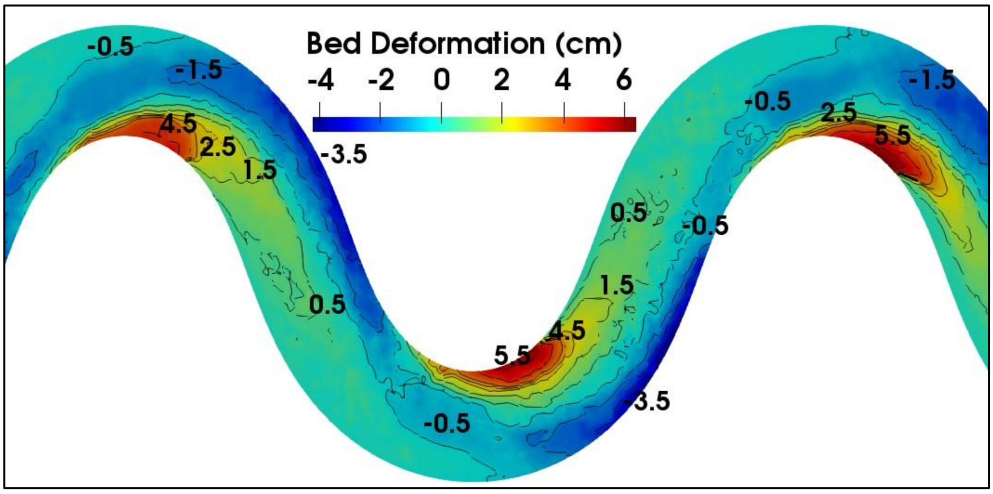

Figure 2.10 Simulated bed deformation contour

(2) Results

Figure 2.9 and Figure 2.10 display the final bed deformation results for the experiment and simulation at 75 min, respectively, where dark colors and blue represent erosion, while light colors and red indicate deposition. By comparing them, we can see that the numerical result has captured the bed deformation features observed in the experiment such as the scour pools along the outer banks, the deposition bars along the inner banks, and alternating deposition-erosion zones along the channel. The ranges of deposition and erosion exhibited a close alignment, especially with a good match for the -0.5 cm contour line. However, there were some areas with underestimation, particularly in the erosion of the second meander, which might be attributed to the inaccurate bank friction and bed shear stress.

In summary, the model is applicable for the investigation of bed deformation in meandering channels.

2.6. Summary

In this chapter, the 3D numerical model for the instigation of the flow and sediment transport around spur dikes in meandering channels is presented.

It consists of two parts: the hydrodynamic model and the sediment transport model. The hydrodynamic model includes the use of the porous medium method (PMM) for seepage flow within the bed, the volume of fluid (VOF) method to capture the free surface, and the $k - \omega$ SST SAS model for turbulence effect. The sediment transport model includes the Eulerian method for suspended load, the Lagrangian method for bed load, and the Exner equation for bed deformation. Benefiting from the PMM, it is possible to use the fixed cell to simulate bed deformation, making it suitable for large deformations such as the local scour near spur dike tips and complex bed topography. Additionally, the Lagrangian method enables the consideration of non-equilibrium sediment transport induced by spur dikes.

Based on the applications in straight channels by Ota et al. (Ota et al., 2017), Ota and Sato (Ota and Sato, 2020), and Okudaira (Okudaira, 2021), the model was tested for the flow field with a U-shaped channel experiment and for the bed deformation based on a movable bed experiment in a meandering channel to validate its applicability to the investigation of the flow and sediment transport around spur dikes in meandering channels for subsequent simulations. For the first one, the simulated water levels and velocity distribution along depth aligned well with the observed ones. For the second one, the numerical result has captured the bed deformation features observed in the experiment. It can be concluded that the model can be used to analyze the flow and sediment transport around spur dikes in meandering channels.

Chapter 3.
3D numerical simulation in meandering channels

3.1. Introduction

The most characteristic features of natural streams, regardless of size, are the absence of long straight reaches and the presence of frequent meanders (Leopold and Langbein, 1966). The erosion-deposition zones and convergence-divergence flow patterns alternate periodically along the meandering channels and are affected by the channel sinuosity (da Silva and Yalin, 2017). Therefore, the flow and sediment transport around spur dikes are affected by not only the arrangement of spur dikes but also the sinuosity of meandering channels.

As the flow pattern changes with the sinuosity, a spur dike at the same location in meandering channels with different sinuosities or at different positions in the same channel can result in different collision angles with the flow, increasing the randomness of bed deformation. As a result, in the following section, a spur dike was sequentially placed at different locations in different meandering channels to numerically investigate the effect of both spur dike position and channel sinuosity.

Spur dikes are typically arranged in series to achieve a more effective outcome from both the perspectives of bank protection and navigation (Giri et al., 2003). The spacing between two adjacent spur dikes is an important consideration in spur dike design, serving as a critical parameter to balance the performance and construction cost. In the subsequent section, a series of spur dikes with different spacings were installed in different meandering channels to investigate the influence of both spur dike spacing and channel sinuosity, and their overall performance was quantitatively assessed by comprehensively considering different factors using the weighted sum approach for multiobjective programming problems.

3.2. The effect of the location of a single spur dike and channel sinuosity

3.2.1. Introduction

Since most of the previous studies on the effect of spur dikes in meandering channels (Kafle, 2021; Karki, 2019; Sharma and Mohapatra, 2012; Tripathi and Pandey, 2021a) were carried out for the case of either a single meandering channel or a single arrangement of spur dikes, the work to systematically study the effect of both the channel sinuosity and the location of a single spur dike is still necessary.

On the one hand, separation zones are observed on the upstream and downstream sides of a spur dike (Sharma and Mohapatra, 2012), and the spacing between two adjacent spur dikes must be smaller than the downstream separation zone length (the distance between the spur dike and reattachment point in Figure 1.1 (a)) (Elhakeem et al., 2017). On the other hand, the local scour, which may jeopardize the safety of the structure, has been one of the fundamental concerns of researchers for years (Basser et al., 2015). As a result, in this section, a single spur dike was sequentially installed at different locations in different meandering channels to numerically investigate the effect of its location on both the downstream separation zone and local scour, as well as its relationship with the channel sinuosity.

3.2.2. Case setup

(1) Channel geometry

The sine-generated curve (SGC) proposed by Langbein and Leopold (Langbein and Leopold, 1966) is widely acknowledged as an idealized description of the channel centerline of natural regular meandering streams (Mecklenburg and Jayakaran, 2012).

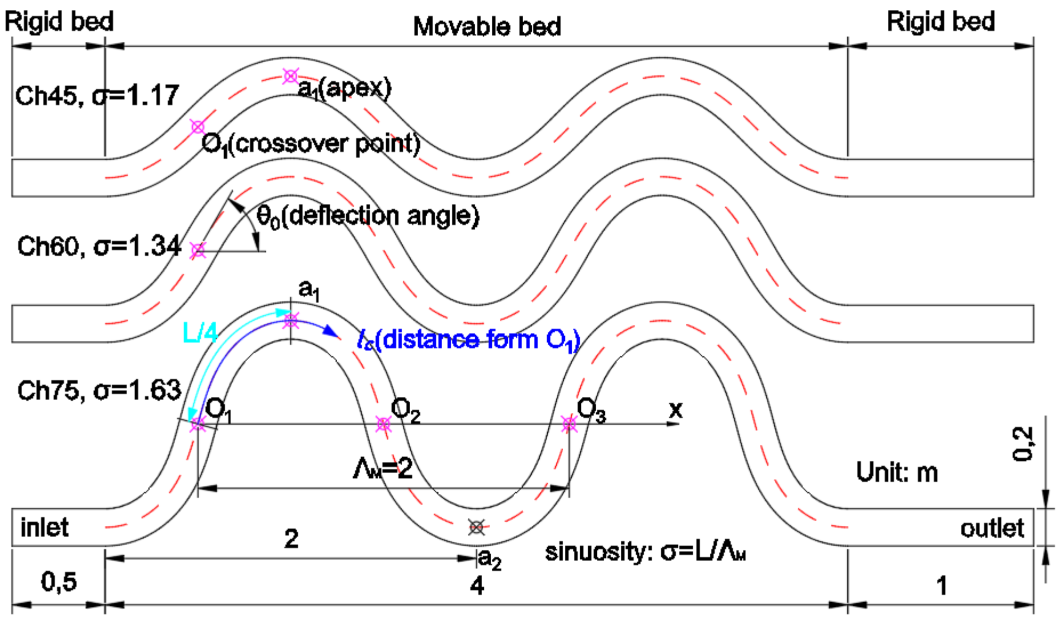

Figure 3.1 Layout plan of the channel arrangement
(Ch45 represents the channel with a maximum deflection angle of 45°)

Table 3.1 Channel parameters

No.	Ch45	Ch60	Ch75
Maximum deflection angle, θ_0 (°)	45	60	75
Sinuosity, σ	1.17	1.34	1.63
Meander wavelength, Λ_M (m)	2	2	2
Meander length, L (m)	2.34	2.68	3.26
Channel width, B (m)	0.2	0.2	0.2
Spur dike length b (m)	0.03	0.03	0.03

Referring to the channels by Karki (Karki, 2019), the channel geometry is depicted in Figure 3.1. The centerline of the meanders is the SGC, determined by the following equation (Langbein and Leopold, 1966):

$$\theta = \theta_0 \cos\left(2\pi \frac{l_c}{L}\right) \tag{3.1}$$

where, L is the meander length, i.e., total path distance along a complete meander; in a curvilinear coordinate system with the origin located at the crossover point O_1 (Figure 3.1), l_c is the path distance to O_1 along the centerline of the channel; θ is the deflection angle at any l_c; θ_0 is the maximum deflection angle. However, Karki (Karki, 2019) actually did not directly use the above equation as the channel centerline but instead fitted arcs and straight lines to facilitate the experimental channel construction. The meandering channel sinuosity is given by:

$$\sigma = \frac{L}{\Lambda_M} \tag{3.2}$$

where, σ is the sinuosity, uniquely determined by θ_0; Λ_M is the meander wavelength.

Three channels were considered, with sinuosities σ of 1.17, 1.34, and 1.63, maximum deflection angles θ_0 of 45°, 60°, and 75°, referred to as Ch45, Ch60, and Ch75, respectively. The channels had a width of 20 cm. Existing data indicated that the flow pattern and bed topography characteristics in sine-generated streams were affected by the ratio of the meander wavelength Λ_M to the channel width B (da Silva and Yalin, 2017). Consequently, all channels were designed to have the same meander wavelength to keep the same ratio. In each channel, there were two consecutive meanders, with their upstream and downstream ends connected to rigid straight channels with lengths of 0.5 m and 1.0 m, respectively.

(2) Spur dike arrangement

As illustrated in Figure 3.2, taking the 45° channel for example, in each channel, an impermeable rectangular spur dike was installed at 6 locations downstream of the crossover point O_1. In total, 18 cases have been simulated. The spur dike location was determined by the nondimensional location $l_c{}^* = l_c/L$, which was obtained by normalizing the path distance l_c with the meander length L. The spur dike had a length of 3 cm, equivalent to 15% of the channel width. The crest of the spur dike was level with the banks, considering only the non-submerged condition.

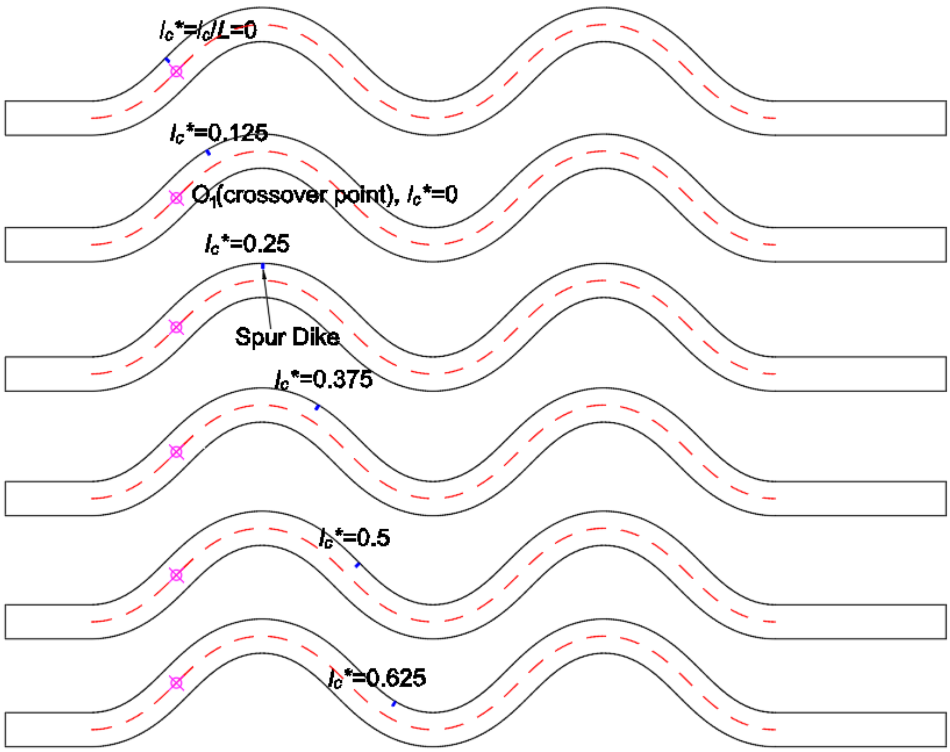

Figure 3.2 Location of the spur dike in Ch45

(3) boundary conditions

Table 3.2 Boundary conditions

Upstream discharge (clear water) (l/s)	0.95
Downstream water depth (cm)	2.86
Channel bed slope	1:550
Sediment properties	
Density (kg/m^3)	1410
Mean diameter (mm)	0.72

Boundary conditions were set based on the experiments of Karki (Karki, 2019). As listed in Table 3.2, in each case, the inlet flow was maintained constant with a discharge of

0.95 l/s, and no sediment was fed to the channel during the simulation, the outlet water depth was kept at 2.86 cm. All simulations concluded at 60 min. The channel banks were non-erodible, and the movable bed was filled with non-cohesive sediment, featuring a median grain size of 0.72 mm and a specific gravity of 1.41. The initial bed slope was 1:550.

In these simulations, GID software was used to generate the semi-structured triangular prism mesh. Horizontal cell size was 1 cm, but 2.5 mm around the spur dike.

3.2.3. Results and discussions

(1) Downstream separation zone length and bank protection extent

The variation of longitudinal near-bed velocity along the left bank was used to find the length of the downstream separation zone. The distance between the spur dike and the point directly downstream where a non-negative value of the longitudinal velocity was observed was taken as the downstream separation zone length L_1.

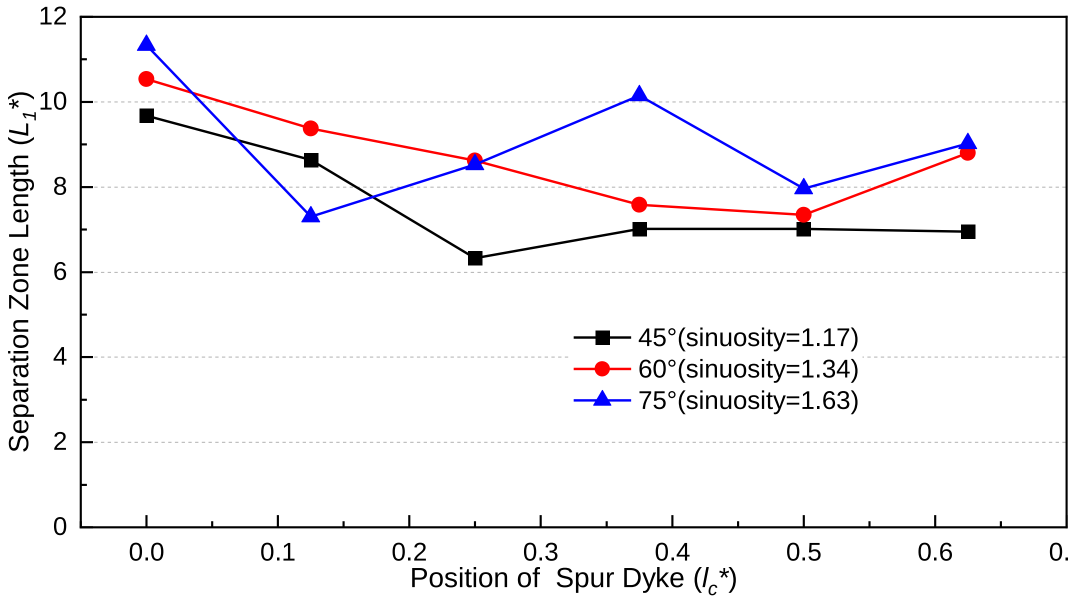

Figure 3.3 Downstream separation zone length of a spur dike in different cases

The nondimensional downstream separation zone length $L_1{}^*$, which was the downstream separation zone length L_1 normalized by the spur dike length b, was plotted graphically and analyzed in Figure 3.3, where the horizontal axis was the dimensionless spur dike location $l_c{}^*$ (Figure 3.2). For cases of Ch45, the nondimensional downstream separation zone length $L_1{}^*$ was maximum when $l_c{}^*$ was equal to zero, i.e., the spur dike was located at the outer bank of the section of the first crossover point (point O_1 in Figure

3.1). As $l_c{}^*$ increased and the spur dike location moved downstream, $L_1{}^*$ decreased and reached the minimum value at $l_c{}^* = 0.25$, that is, the spur dike was located at the outer bank of the apex section (point a_1 in Figure 3.1). After that, $L_1{}^*$ increased slightly and remained around 7.0. This variation trend of $L_1{}^*$ with the spur dike location at the outer bank was basically consistent with the experimental results of cases 4 to 8 in a 50° meandering channel by Sharma and Mohapatra (Sharma and Mohapatra, 2012). The trend of the variation of $L_1{}^*$ for Ch60 cases was similar to that of Ch45 cases, but its $L_1{}^*$ reached the minimum value around $l_c{}^* = 0.5$ (crossover point O_2 in Figure 3.1), and $L_1{}^*$ of all locations was greater than that of Ch45 cases. For Ch75 cases, although the results were somewhat fluctuating, the overall trend was consistent with the first two channels, that is, overall, $L_1{}^*$ decreased as $l_c{}^*$ increased. In addition, it seemed that the spur dike location for minimum $L_1{}^*$ varied with the channel sinuosity. For all cases, at the same spur dike location, except for $l_c{}^*$ equal to 0.125 and 0.25 (upstream of the apex point a_1), $L_1{}^*$ increased as the sinuosity increased. In other words, downstream of the outer bank apex at the same location, $L_1{}^*$ increased with an increase in channel sinuosity.

As a result, larger spacing can be used in upstream reach, especially upstream of the apex. In the reach near the crossover point (O_2), the spacing should be reduced accordingly. Non-uniform spacing can be adopted to reduce the cost of construction and improve cost-effectiveness. In addition, the spacing also should be adjusted with the channel sinuosity.

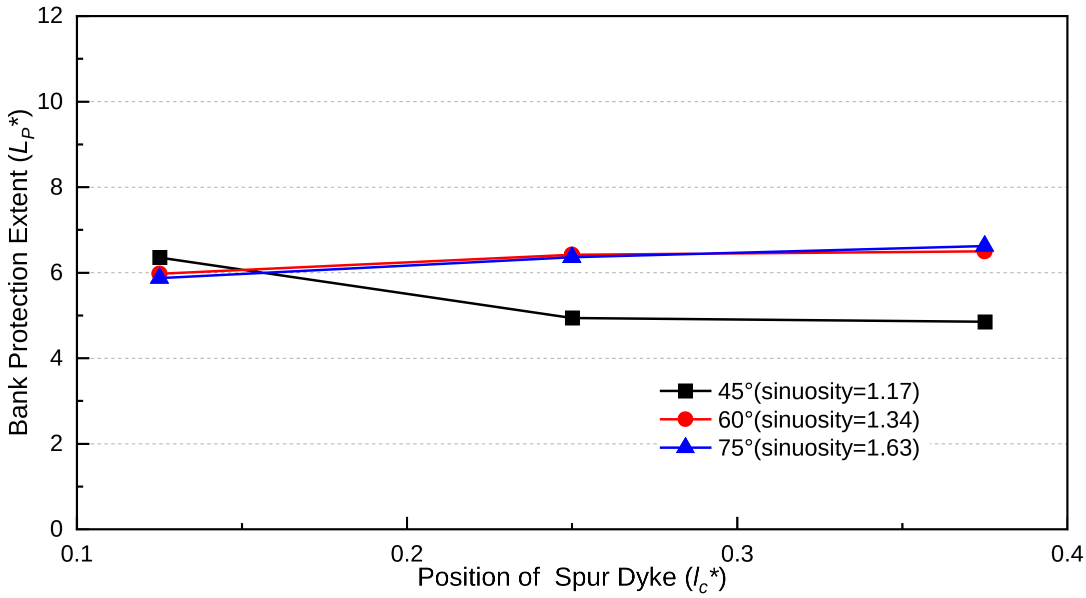

Figure 3.4 Bank protection extent of a spur dike in different cases

Bank protection extent L_p is the length of the bank downstream of the spur dike where the riverbed deformation is greater than 0. It was determined by observing the riverbed deformation along the left bank. Due to the longitudinal alternation of adjacent erosion-deposition zones in meandering streams, the bank protection extent for $l_c{}^* = 0$ (crossover point O_1), 0.5, and 0.625 (downstream of the crossover point O_2) could not be clearly measured. As a result, only the bank protection extent for $l_c{}^*$ between 0.125 and 0.375, i.e., the spur dike was located between the two crossover points, is presented in Figure 3.4. The nondimensional bank protection extent, $L_p{}^* = L_p/b$, of Ch45 cases was observed in the range of 4.9 to 6.4 and decreased mildly with $l_c{}^*$ increasing. The results of Ch60 cases were close to those of Ch75 cases, in the range of 6.0 to 7.0, and marginally increased as $l_c{}^*$ increased. Overall, the values of bank protection extent were concentrated between 5 and 7 times the spur dike length, less than the corresponding downstream separation zone length compared to Figure 3.3.

(2) Maximum local scour depth

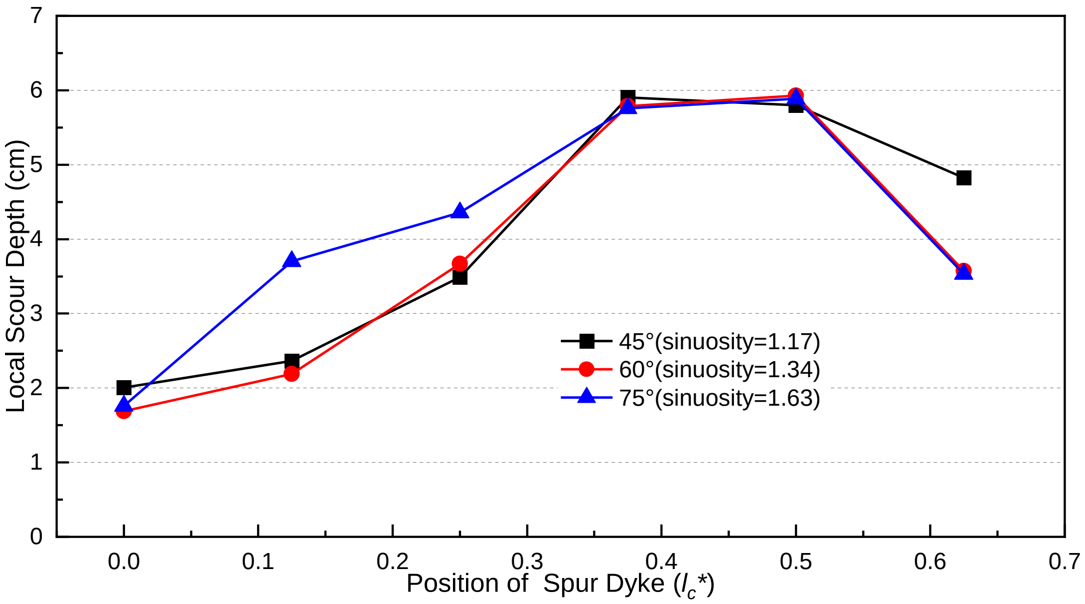

Figure 3.5 Local scour depth around a spur dike tip in different cases

The scour hole was observed around the spur dike tip due to the local scour. The maximum eroded depth of the scour hole near the spur dike tip was taken as the maximum local scour depth d_p, which was measured by observing the riverbed deformation along the cross-section where the spur dike was located. Figure 3.5 depicts the variation of maximum local scour depth d_p with the nondimensional spur dike location $l_c{}^*$ for the three channels. The results of the three channels had the same trend, d_p was minimum at the furthest upstream. increased as the spur dike moved downstream and reached the maximum value near the crossover point (O_2), which might endanger its safety. In this reach, it is more likely that specific measures are required to be taken to mitigate the local scour, for example, changing the orientation, spacing, or type of the spur dike. Upstream of this location, channels with greater sinuosity exhibited larger local scour, whereas the opposite trend was observed downstream.

3.3. The effect of the spacing of a series of spur dikes and channel sinuosity

3.3.1. Introduction

The spacing between two adjacent spur dikes is an important consideration in spur dike design, serving as a critical parameter to balance the performance and construction cost. Most of the previous studies on spacing (Cao et al., 2013; Gu et al., 2020; Möws and Koll, 2019; Ning et al., 2019; Vaghefi et al., 2016) were conducted in either straight channels or a single bend, and they were concentrated on the hydrodynamic and morphodynamic processes. In addition, although the development of local scour may pose a risk to the stability of spur dikes, the pools formed by the local scour and the diversified flow around spur dikes are attractive for enhancing the aquatic habitat (Sadat and Tominaga, 2015). The investigation of the spacing of spur dikes in meandering channels and its effect on the aquatic habitat is rarely concerned. Therefore, the work to identify the optimum spacing in meandering channels and to instigate the effect on the aquatic habitat is still required.

In this section, the effect of two sinuosities and five spacings on bed deformation and flow was numerically investigated at first. Then, an equation using the weighted sum approach for multiobjective programming problems was proposed to quantify the overall performance of different spacings by considering four factors of bank protection effectiveness, structural stability, construction cost, and aquatic habitat, in order to identify the optimum spacing for each channel.

3.3.2. Case setup

(1) Channel geometry and boundary conditions

In this section, the channels Ch45 and Ch60 used in the previous section were taken into consideration, having sinuosities of 1.17 and 1.34, along with maximum deflection angles of 45° and 60°, respectively (Figure 3.1). Except for the arrangement of spur dikes, the bed sediment conditions, and hydraulic boundary conditions were the same as in the previous section (Table 3.2), and the duration of each simulation was also 60 minutes.

(2) Arrangement of spur dikes

The spacing between spur dikes is often expressed as a multiple of the spur dike length, and a ratio of 2 to 6 is generally used for bank protection (Alauddin et al., 2017). Therefore, from 2 to 6 times the spur dike length, we set 5 spacing cases in each channel and simulated 10 cases in total. Detailed arrangements are shown in Figure 3.6. Regarding the extent of spur dikes, the location of the first spur dike (most upstream) followed the criteria by Brown (Brown, 1984), the last spur dike was placed near the crossover point (O_2 in Figure 3.1) according to the simulations of a single spur dike in the previous section. The dimensions of spur dikes were the same as in the previous section, with a length of 3 cm (15% of the channel width). The crests of spur dikes were level with the banks, considering only the non-submerged condition.

In this section, GID software was still used to generate the semi-structured triangular prism mesh with an average horizontal cell size of 2.5 mm around spur dikes and 1 cm elsewhere.

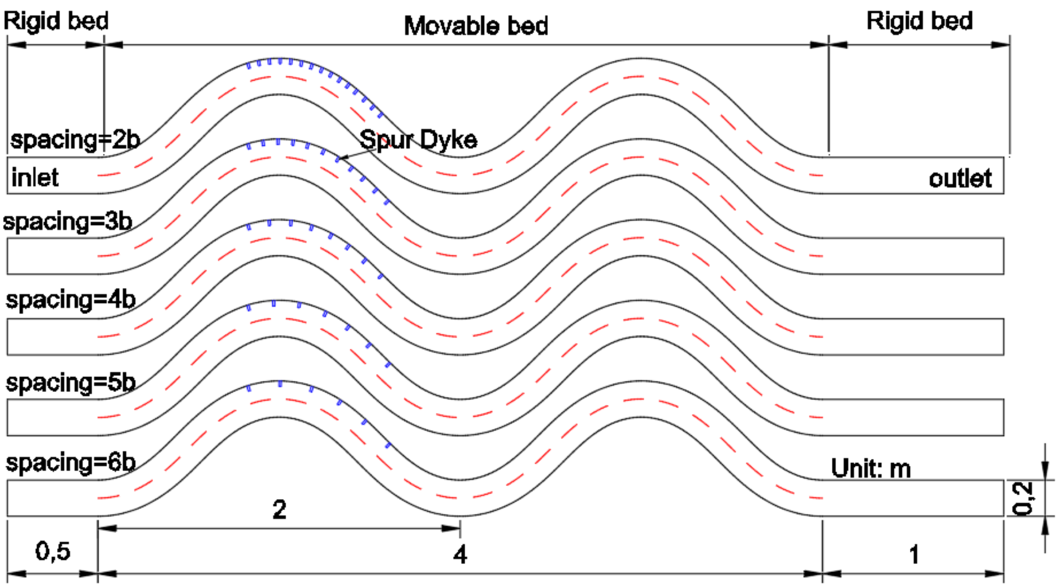

(a) Ch45 (the channel with a maximum deflection angle of 45°)

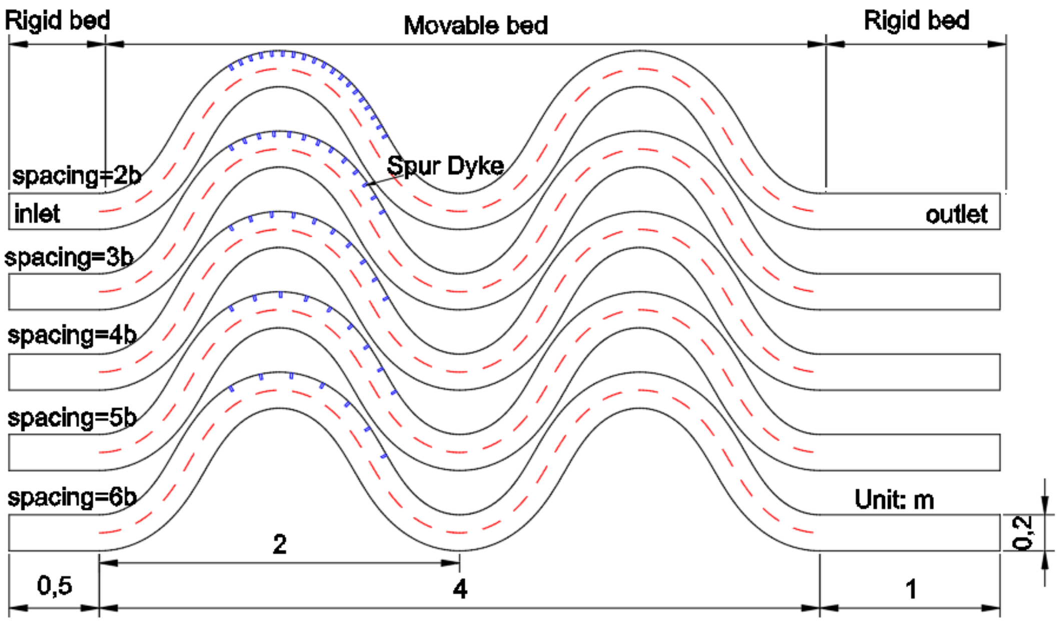

(b) Ch60 (the channel with a maximum deflection angle of 60°)

Figure 3.6 Spur dikes arrangement for Ch45 and Ch60

3.3.3. Results and discussions

(1) Bed deformation

Bed deformation contours of all cases of Ch45 at the final stage are shown in Figure 3.7. Consistent with the straight channel experiment of Ning et al. (Ning et al., 2019), an integral large scour zone was formed downstream of the first (most upstream) spur dike with a small spacing of $2b$ (Figure 3.7 (a)), and the local scour hole of each spur dike remained relatively complete with a large spacing (Figure 3.7 (e)). However, meandering channel had its own features. When the spacing was $3b$, a new scour zone formed downstream of the apex, and it was deeper than the scour zone near the first spur dike (Figure 3.7 (b)). This was different from the straight channel experiment result of Ning et al. (Ning et al., 2019), where the new scour zone was not deeper than the one near the first spur dike. Besides, relatively intact small scour holes were observed around the two most downstream spur dikes After that, as the spacing increased, the individual scour holes around downstream spur dikes became apparent, and new separate scour holes gradually appeared near the further upstream spur dikes (Figure 3.7 (c), (d)). As shown in Figure 3.7 (e), there was no independent scour hole around the second spur, and the spur dike installed near the apex seemed to be ineffective and unnecessary.

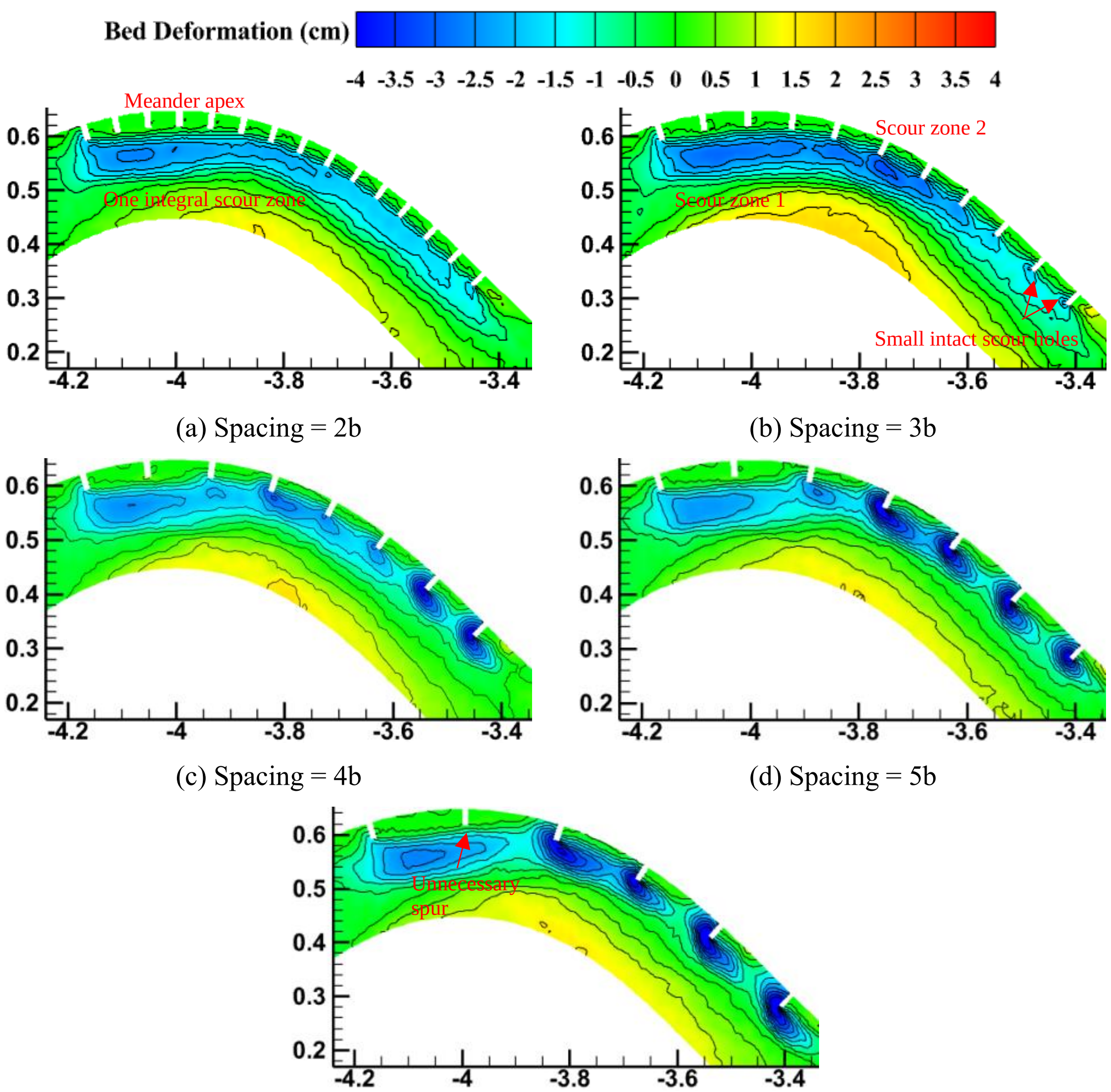

(a) Spacing = 2b (b) Spacing = 3b

(c) Spacing = 4b (d) Spacing = 5b

(e) Spacing = 6b

Figure 3.7 Contours of bed deformation for Ch45

The trend of Ch60 cases, as shown in Figure 3.8 was similar to that of Ch45 cases. However, due to the effect of the sinuosity, even with a spacing of $2b$, there were two separate scour zones in Figure 3.8 (a), and the one downstream was deeper than the one upstream. Besides, compared to Ch45, the most sever scour location shifted upstream. In the cases with large spacings, the depths of scour holes around the four downstream spur dikes were extremely similar in Ch45 (Figure 3.7 (d), (e)), while in Ch60, the local scour of the spur dikes close to the apex was more severe than that of the more downstream spur dikes (Figure 3.8 (d), (e)). This should be related to the erosion-deposition zones shifting with the sinuosity in meandering channels.

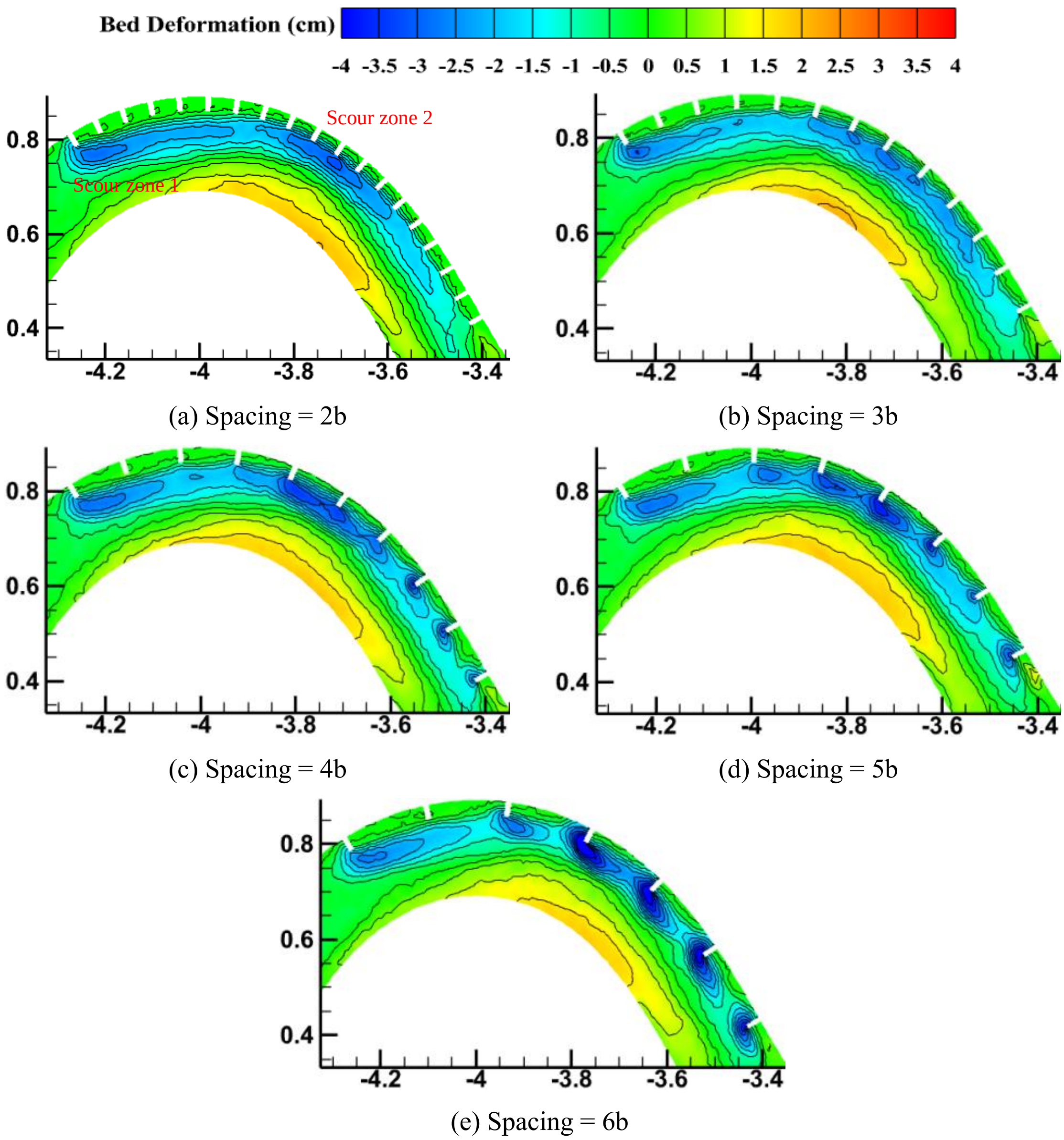

(a) Spacing = 2b

(b) Spacing = 3b

(c) Spacing = 4b

(d) Spacing = 5b

(e) Spacing = 6b

Figure 3.8 Contours of bed deformation for Ch60

Based on the above results, in meandering channels, non-uniform spacing should be adopted to reduce the spur dike number, i.e., the construction cost. For Ch45, it is appropriate to gradually reduce the spacing from upstream to downstream, while for Ch60, it seems better to use a larger spacing both upstream and downstream, but a smaller spacing in the middle.

In addition, unlike straight channels where the maximum scour depth is generally found in the vicinity of the first spur dike tip (Ning et al., 2019), in meandering channels, serious local scour occurred not only near the first spur dike tip but also surrounding the spur dikes located downstream of the apex. The erosion in the latter location was much severer than the former one in most cases. Both locations should be given special attention to control local scour in practices.

(2) Flow field

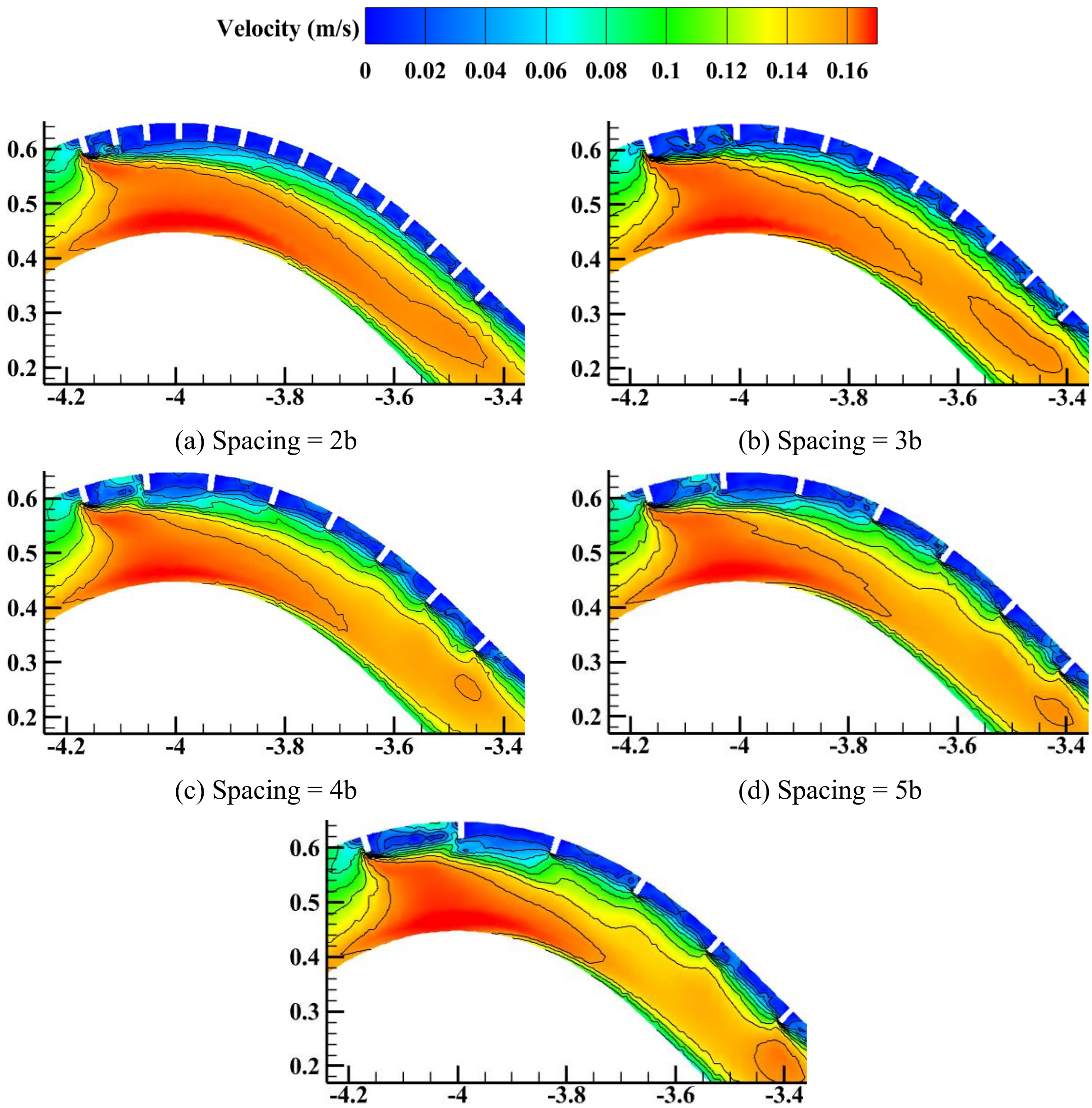

Figure 3.9 Contours of near-bed velocity (at 10% water depth) magnitude for Ch45

Rigid flat bed simulations were conducted to analyze the flow field. Figure 3.9 and Figure 3.10 present the contours of near-bed velocity (at 0.1 water depth) magnitude. The mainstream was shifted from the outer bank to the inner bank by spur dikes. Affected by the meander, the first spur dike effectively deflected the flow away from the outer bank, forming a long low-velocity zone. Downstream the apex, the flow hit spur dikes again resulting in a new local scour zone in addition to the one around the first (most upstream) spur dike. With a small spacing of $2b$, in the proximity of the spur dike tips, the velocity magnitude and the contour line density were not large, and the velocity contour lines were quite smooth, indicating a smooth transition of streamlines. As the spacing increased, the contour lines close to spur dike tips became increasingly rough and jagged. Starting from downstream, the contour line density around spur dike tips increased, i.e., higher velocity gradient, and the flow penetrated into the spur dike fields, leading to separate local scour holes.

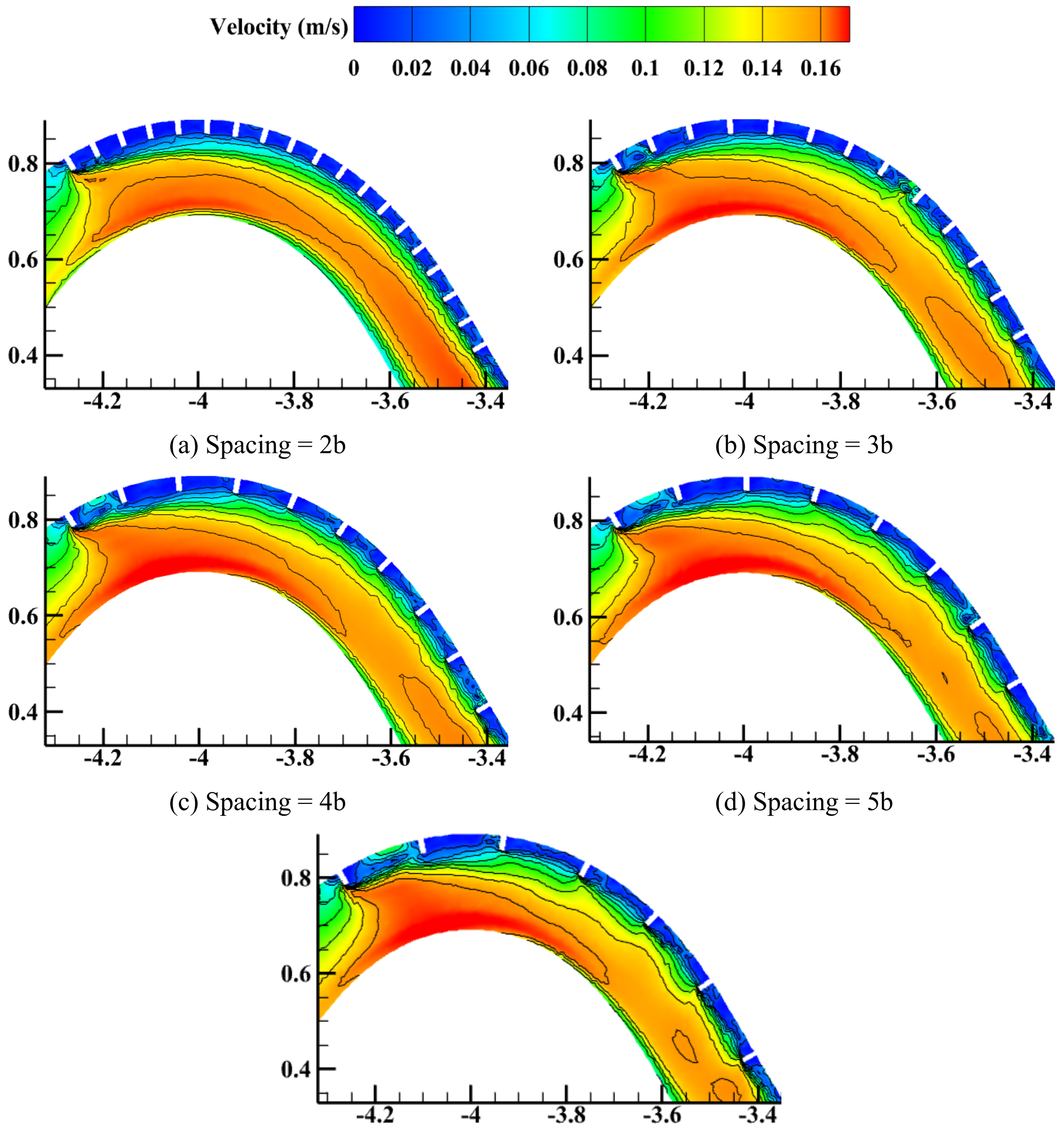

(a) Spacing = 2b

(b) Spacing = 3b

(c) Spacing = 4b

(d) Spacing = 5b

(e) Spacing = 6b

Figure 3.10 Contours of near-bed velocity (at 10% water depth) magnitude for Ch60

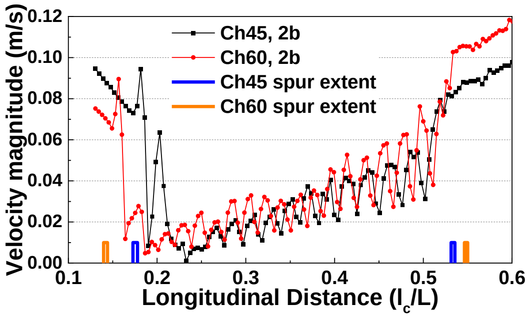

(a) Spacing = 2b

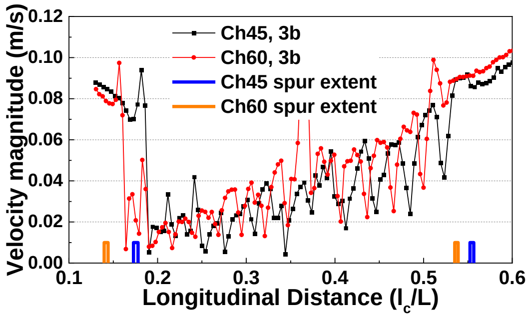

(b) Spacing = 3b

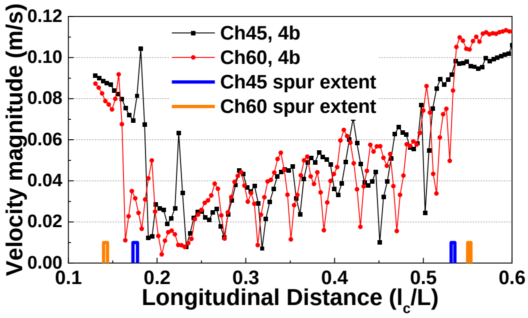

(c) Spacing = 4b

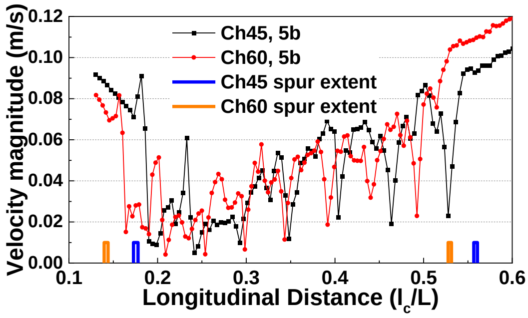

(d) Spacing = 5b

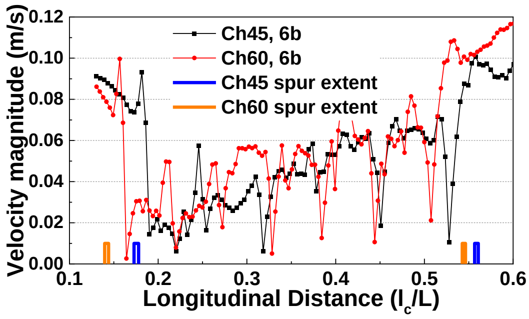

(e) Spacing = 6b

Figure 3.11 Longitudinal profiles of near-bed velocity (at 10% water depth) magnitude along spur tips

The near-bed velocity (at 10% water depth) magnitude along spur tips was plotted in Figure 3.11. L is the meander length, l_c is the distance to the crossover point O_1 along the centerline as shown in Figure 3.1. The first spur dike had the most significant flow-deflecting effect, resulting in the minimum flow velocity downstream of it. With a small spacing of $2b$ (Figure 3.11 (a)), the fluctuations of velocity magnitude along spur dike tips were small, indicating a relatively smooth transition of streamlines. As the spacing increased, the fluctuations became bigger and bigger, that is, the velocity gradient, the velocity magnitude and the turbulence increased, leading to separate local scour holes. In Ch45, the velocity fluctuations amplitude became larger downstream from the apex almost for all cases. In Ch60, $2b$, $3b$, and $4b$ cases (Figure 3.11 (a), (b), (c)) had the same pattern, but for $5b$ and

$6b$ (Figure 3.11 (d), (e)), the fluctuation amplitude did not change much after $l_c/L = 0.3$, and the location of the most severe scour hole may be related to this.

(3) Aquatic habitat assessment

The aquatic habitat was assessed by considering space availability and habitat diversity.

Space availability is a crucial factor in providing a favorable aquatic habitat for fish, which can be characterized by the depth, volume, and extent of pools along the channel (Mansoori, 2014). Therefore, the aquatic habitat space availability was assessed by computing the volume V_E and the planar area A_E of the deep pools (scour holes 5 mm beneath the zero bed level (Sadat and Tominaga, 2015)) within the spur dike reach.

Habitat diversity is essential for fish populations (Mansoori, 2014). The three most common habitats, pool, riffle, and run, were defined based on velocity/depth ratio (v/d) and Froude number (Fr), i.e., $v/d < 1.24$ & $Fr < 0.18$ for pool, $v/d > 3.2$ & $Fr > 0.41$ for riffle, and other for run (Jowett, 1993). Since seldom areas satisfied $Fr > 0.41$, this condition was ignored in this part. The spatial entropy (H) (Wang and Wang, 2011) was selected to assess habitat diversity within the spur dikes reach, which reads:

$$H = -\sum_{i=1}^{m} \frac{d_i^{int}}{d_i^{ext}} \frac{n_i}{N} \log \frac{n_i}{N} \tag{3.3}$$

where, m is the number of habitat types i.e., 3; n_i is the number of entities for habitat type i; N is the total number of all entities; d_i^{int} is the average distance between entities belonging to habitat type i; d_i^{ext} is the average distance between entities of habitat type i and entities of all other habitat types. In the current calculation, n_i and N have been replaced by the area considering the difference between cells.

The values of V_E, A_E, H are listed in Table 3.3. Regarding habitat diversity, the differences of H were very small for different spacings in each channel. In the current channel conditions, the spacing of spur dikes had a negligible impact on factor H. As for space availability, the bigger deep pool volume V_E tended to have the larger planar area A_E except for $5b$, $6b$ in Ch45, and 6b in Ch60 due to the deep scour holes. For both Ch45 and Ch60, A_E increased first and reached their peak values of 738 and 875 cm^2 when the spacing was $3b$ and $4b$ respectively, before decreasing to 661 and 801 cm^2 with an increasing spacing. In Ch45, from $3b$, separate local scour holes became extremely deep (Figure 3.7 (c) (d), (e)), while in Ch60, it was from 4b (Figure 3.8 (d), (e)), which might be the reason for the decrease of A_E.

Table 3.3 Performance evaluation parameters

Ch45						
Spacing		2b	3b	4b	5b	6b
Physical habitat	V_E (cm^3)	1035	**1213**	1086	1121	1153
	A_E (cm^2)	690	**738**	701	674	661
	H	0.370	**0.376**	0.366	0.369	0.356
V_p (cm^3/cm)		**0.005**	0.009	0.135	0.303	0.384
d_p (cm)		**1.84**	2.51	4.54	5.36	5.12
M		15	11	8	7	**6**
S		**0.83**	0.71	0.53	0.54	0.58
Ch60						
Spacing		2b	3b	4b	5b	6b
physical	V_E (cm^3)	1313	1282	**1388**	1384	1345
	A_E (cm^2)	849	851	**875**	866	801
	H	**0.401**	0.395	0.395	0.390	0.390
V_p (cm^3/cm)		**0.016**	0.017	0.07	0.079	0.233
d_p (cm)		2.53	**2.48**	3.50	3.71	5.51
M		19	13	10	8	**7**
S		0.83	**0.86**	0.66	0.68	0.62

(4) Performance evaluation

In this part, we employed multiobjective programming (MOP) to quantitatively evaluate the performance of different spacings by comprehensively considering four aspects: bank protection, structural stability, construction cost, and aquatic habitat, based on the simulation results.

The potential bank erosion V_p, listed in Table 3.3, was used to indicate the bank protection effectiveness. It was evaluated following the method of Mansoori (Mansoori, 2014) by calculating the eroded sediment volume per unit length in a 1 cm wide strip 25 mm from the bank within the spur dike reach. Smaller values of V_p indicate a better effectiveness of bank protection. In both Ch45 and Ch60, the values of V_p were quite small with spacings of $2b$ and $3b$. Then, they increased significantly from 0.009 to 0.384 and from 0.017 to 0.233, respectively, as the spacing increased to $6b$. Similar to the straight channel results of Mansoori (Mansoori, 2014), the largest spacing had the biggest V_p.

The structural stability was indicated by the maximum local scour depth d_p, which was summarized in Table 3.3. It was measured by sampling longitudinal bed profiles along spur tips. In Ch45, the value of d_p increased from 1.84 to 5.36 cm, as spacing increased from

$2b$ to $5b$. Then it slightly decreased to 5.12 cm for $6b$. This may be affected by the complex meander flow and the location of spur dikes. The location of d_p for $6b$ was near the 5th spur dike from upstream, while it was 4th for $5b$, closer to the apex. In large spacing cases, the flow became more turbulent than that of small spacing, increasing the randomness of the local scour. In Ch60, d_p increased with spacing except for $2b$ and was smaller than that of Ch45 except for $2b$ and $6b$ affected by sinuosity.

The number of spur dikes M was employed to represent the construction cost, as shown in Table 3.3.

The weighted sum approach (Ehrgott and Wiecek, 2005; Ma, 2004) was used to quantify the performance of different spacings. The method is a common approach for solving MOP problems. It involves assigning a weight to each objective function, reflecting its importance, and linearly combining these objective functions based on their weights, thereby transforming the MOP problem into a single objective programming (SOP) problem. Since the performance was negatively correlated with V_p, d_p and M, the reciprocals of these three factors were used for performance evaluation. An index S, positively correlated with the performance, was calculated by the following weighted sum to quantify the overall performance.

$$S_i = w_{V_p}\frac{1/V_{p_i}}{\max\limits_{i\in K}\frac{1}{V_{p_i}}} + w_{d_p}\frac{1/d_{p_i}}{\max\limits_{i\in K}\frac{1}{d_{p_i}}} + w_M\frac{1/M_i}{\max\limits_{i\in K}\frac{1}{M_i}} + w_{PH}PH_i \tag{3.4}$$

$$PH_i = \frac{1}{3}\left(\frac{V_{E_i}}{\max\limits_{i\in K}V_{E_i}} + \frac{A_{E_i}}{\max\limits_{i\in K}A_{E_i}} + \frac{H_i}{\max\limits_{i\in K}H_i}\right) \tag{3.5}$$

where, i is the label for different spacing cases; w is the weight of each factor; K is the group of spacing cases.

That is using the best values of each factor in all spacing designs as the standard to score each spacing. The standard can be set according to actual needs. In this study, the weights of the four factors were considered equally, i.e., all took 0.25, which could also be determined by the actual situation. The results are listed in Table 3.3.

Based on the uniform spacing simulations, the $2b$ and $3b$ were optimum spacing for Ch45 and Ch60, respectively. Although smaller spacings required higher economic costs, the $2b$ and $3b$ had significantly better performance in terms of bank protection and structural stability compared with other spacings. In addition, there was not much difference in the values characterizing the aquatic habitat assessment, as shown in Table 3.3, so the aquatic habitat assessment method may need to be improved.

3.4. Summary

In this chapter, the 3D numerical model elaborated in the previous chapter was applied to the investigation of flow and sediment transport around spur dikes in meandering channels.

Firstly, we analyzed the effect of the location of a spur dike along the outer bank of a meander on the downstream separation zone length, bank protection extent, and local scour depth, as well as its relationship with the channel sinuosity. The downstream separation zone length and local scour depth depended on both the location of the spur dike and channel sinuosity. The bank protection extent of measured cases was less than the corresponding downstream separation zone. The downstream separation zone length decreased as the spur dike moved downstream. Correspondingly, non-uniform spacing could be adopted to improve cost-effectiveness. Channels with larger sinuosity were more likely to have longer downstream separation zones. Local scour depth increased as the spur dike moved downstream and reached the maximum near the crossover point, where measures might need to be taken to mitigate the local scour. Upstream of this location, channels with greater sinuosity exhibited more severe local scour, whereas the opposite trend was observed downstream.

Secondly, we investigated the effect of spacing and channel sinuosity on flow and bed deformation in meandering channels. Unlike straight channels where maximum scour depth is located near the first spur dike, in meandering channels, serious local scour occurs near both the most upstream spur dike and spur dikes downstream of the meander apex. Therefore, both of these locations should be given special attention to control local scour in practices. Since the deep local scour holes and large velocity fluctuations occurred at different locations with varying spacing, non-uniform spacing should be adopted to lower the construction cost. Different channel sinuosities required different spacing arrangements because the locations of deep local scour holes and large velocity fluctuations were affected by sinuosity. In addition, based on the simulation results, an equation using the weighted sum approach for multiobjective programming problems was proposed to quantify their performance by comprehensively considering four factors of bank protection, structural stability, construction cost, and aquatic habitat. In uniform spacing simulations, $2b$ was the optimum spacing for Ch45 and $3b$ was the best for Ch60.

It is hoped that the results can provide useful information for the spur dike design in practice. It should be noted that this numerical investigation was based on laboratory conditions, having channel width-to-depth (B/h) ratio many times smaller than that of an extensively meandering river, which could lead to the exaggeration of the effect of secondary currents in meanders. The performance of spur dikes in channels with different B/h ratios needs to be investigated.

Chapter 4.
3D modelling of Bank Erosion

4.1. Introduction

Bank erosion is a predominant river morphodynamic process, leading to channel migration, the loss of agricultural lands, and damage to hydraulic structures and infrastructure. Hence, bank protection structures like spur dikes are necessary to control bank erosion. However, it is important to note that bank erosion can also create diverse habitats, contributing to ecological diversity (Lai, 2017). Consequently, some restoration projects have removed bank protection (van der Mark et al., 2012). Therefore, there is a need for reliable and practical 3D numerical models that consider bank erosion to evaluate the performance of spur dikes, guide their design, and assess the morphodynamic response to their removal in restoration projects.

In this chapter, a simple bank mass failure operator was incorporated into the 3D numerical model elaborated in Chapter 2 to develop a new solver that can handle bank erosion. The bank mass failure operator was based on the fixed triangular prism mesh, eliminating the need to explicitly identify the bank locations, and making it suitable for complex riverbanks with spur dikes. It compares the slope angle of each bed surface cell with the critical stability slope angle to determine the stability of this cell and realizes the mass failure by rotating unstable cells.

4.2. Model description

4.2.1. Bank mass failure criterion

Before the bank mass failure operator is applied, a criterion is required to check whether the bank is stable or not. For non-cohesive riverbanks, some studies (Menéndez et al., 2008; Nagata et al., 2000) have compared the bank slope with the angle of repose as a criterion for triggering bank mass failure. If the slope of a riverbank is steeper than the angle of repose of bank materials, a failure surface inclined at the angle of repose extends to the bank top surface. Then, sediment above the failure surface is displaced downslope, resulting in the formation of a deposit with a linear upper surface.

Further, considering that the apparent cohesion of the partially saturated sediment can increase its stability, Spinewine et al. (Spinewine et al., 2002) proposed a simple criterion for the bank mass failure by taking into account distinct angles of repose for the emerged materials (partially saturated sand) and for the submerged materials (saturated sand) based on the experimental observations of lateral erosion induced by dam-break flows in loose sediment valleys. It is claimed that this method constitutes a rough analog of cohesive bank failures.

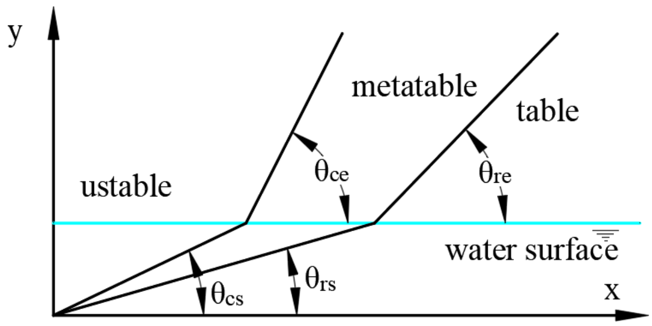

Figure 4.1 Definition of stability angels (source: (Spinewine et al., 2002))

As presented in Figure 4.1, they introduced two critical angles, θ_{cs} and θ_{ce}, a lower one for the bank below the water surface and a higher one for the part above the water surface, which is consistent with the fact that bank portions above the water surface typically exhibit steeper slopes than those below the water surface in natural rivers. Regarding the state of the bank, in addition to the stable state and the unstable state, they also added an additional transition state, the metastable state, by defining two residual angles, θ_{rs} and θ_{re}, for the submerged area and the emerged area, respectively. The slopes that are less steep than the corresponding residual angle are deemed stable, while the slopes falling within the corresponding critical angle and residual angle are termed metastable, since such a slope angle is considered stable for the existing bank but not for the new bank that forms following a bank mass failure. Once bank slopes surpass the corresponding critical angle, it leads to the initiation of the bank mass failure. The failed materials are moved downslope and deposited with the corresponding residual angle.

Some 2D numerical models over unstructured triangular mesh (Abderrezzak et al., 2016; Evangelista et al., 2015; Swartenbroekx et al., 2010) adopted this bank mass failure criterion and achieved good results. This method can eliminate the necessity to explicitly identify the location of the riverbank, greatly enhancing its convenience. As a result, these four threshold angles also will be employed in the current study to judge the stability of each bed surface cell.

For uniform coarse sand with a median diameter of $1.8\,\mathrm{mm}$, a density of $2615\ \mathrm{kg/m^3}$, a loose porosity of 0.405 and a permeability of $1.5\,\mathrm{cm \cdot s^{-1}}$, different angles of repose were measured at rest under different conditions, dry, humid, or submerged (Spinewine et al., 2002). Following this, by default, the threshold angles are set to:

$$\theta_{cs} = 35°,\ \theta_{rs} = 30°,\ \theta_{ce} = 87°,\ \theta_{re} = 85°, \tag{4.1}$$

where, θ_{cs} is the submerged critical angle; θ_{rs} is the submerged residual angle; θ_{ce} is the emerged critical angle; θ_{re} is the emerged residual angle. These angle values can be calibrated and adjusted to suit specific cases.

4.2.2. Bank mass failure operator

In the previous section, the bank failure criterion (critical slope angle) and the stable bank configuration (residual slope angle) have been given. In this part, the method used to model the bank evolution from an unstable state to a stable state will be elaborated.

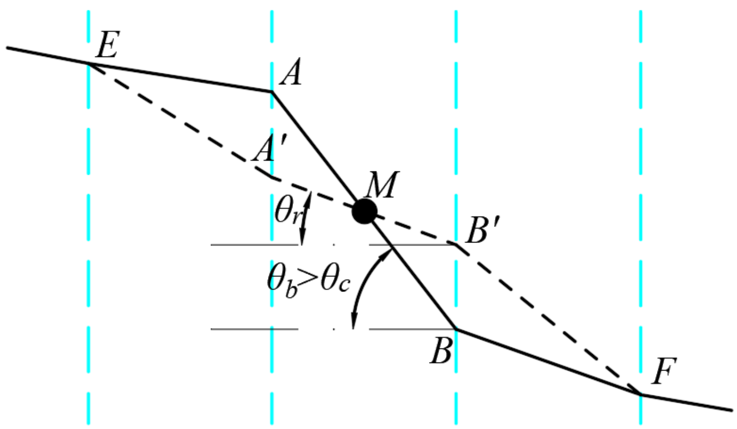

Figure 4.2 Cross-section profile adjustment during mass failure (source: (Zech et al., 2008))

Zech et al. (Zech et al., 2008) proposed a method for the river bank cross-section adjustment when bank mass failure occurs. As illustrated in Figure 4.2, the three-segment line $EABF$ is a part of a bank cross-section profile. When the local slope angle θ_b of section AB exceeds the critical angle θ_{cs} or θ_{ce}, it undergoes a rotational movement around the midpoint M until it reaches the position $A'B'$, which corresponds to the residual angle θ_{rs} or θ_{re}. This adjustment may potentially affect the stability of adjacent sections, for example, from EA and BF to EA' and $B'F$. Therefore, this process is iteratively applied to the entire profile until all sections achieve stability. Swartenbroekx et al. (Swartenbroekx et al., 2010), Evangelista et al. (Evangelista et al., 2015), and Abderrezzak et al. (Abderrezzak et al., 2016) also applied a similar idea in their 2D planar models. Instead of rotating the unstable segments of cross-section profiles, they rotated unstable cells around a horizontal axis.

In this study, a similar technique is adopted, except that some details are different, such as the calculation of local slope angles of bed surface cells, the method of the rotation of bed surface cells from an unstable state to a stable state, and the computation of bed elevation height changes after rotation. These adaptions are made to better suit the cell-centered finite volume method (CCFVM) used in OpenFOAM and the sediment transport model presented in the previous chapter.

4.2.2.1. Calculation of local slope angle

In OpenFOAM, all the variables are stored at each cell center, so it may not be the most appropriate choice to calculate the local slope angle using node elevations as was done in other models (Abderrezzak et al., 2016; Evangelista et al., 2015; Swartenbroekx et al., 2010). Although it is possible to create new arrays treating node elevations, using grid elevations is more convenient, and should be more suitable for parallel calculations in OpenFOAM. For example, Swartenbroekx et al. (Swartenbroekx et al., 2010) also employed the CCFVM and additionally computed node elevations, but they adopted a complicated method to adjust an unstable bed surface cell in order to keep the mass conservation of sediment. The adjustment of a cell required information on all surrounding cells that shared at least one common node with this cell, which may not be friendly to the parallel calculation in OpenFOAM.

Since in the CCFVM, each bed cell has its own distinct level, it is impossible to obtain the local slope angle of a bed cell solely based on the information of that cell itself. Therefore, the elevation of three adjacent cells of a given cell is taken into account to define its slope angle. As depicted in Figure 4.3, the local slope angle of a cell o is determined by the three neighboring cells a, b, c, that share an edge with the cell o. A, B, C are the centroids of these three cells a, b, c, respectively. The slope surface defined by A, B, C is used to represent the bed surface of the cell o. The angle θ_b (Figure 4.4) between the triangle ABC and the horizontal plane is regarded as the slope angle of cell o, which can be calculated from the upward-pointing unit normal vector of triangle ABC.

$$\theta_b = \frac{n_y}{|\mathbf{n}|} \tag{4.2}$$

$$\mathbf{n} = \frac{\overrightarrow{AB} \times \overrightarrow{AC}}{|\overrightarrow{AB} \times \overrightarrow{AC}|} \tag{4.3}$$

where, $\mathbf{n}$ is the upward-pointing unit normal vector of triangle ABC, and n_y is the upward component.

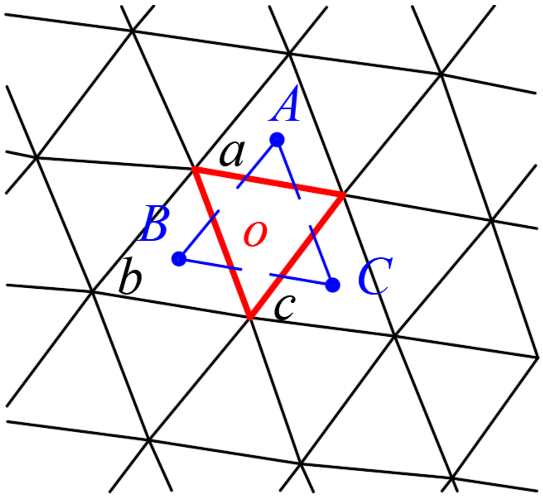

Figure 4.3 Plan view of triangular unstructured mesh
(a, b, c, o denote cells, A, B, C are the centroids of cells a, b, c, respectively)

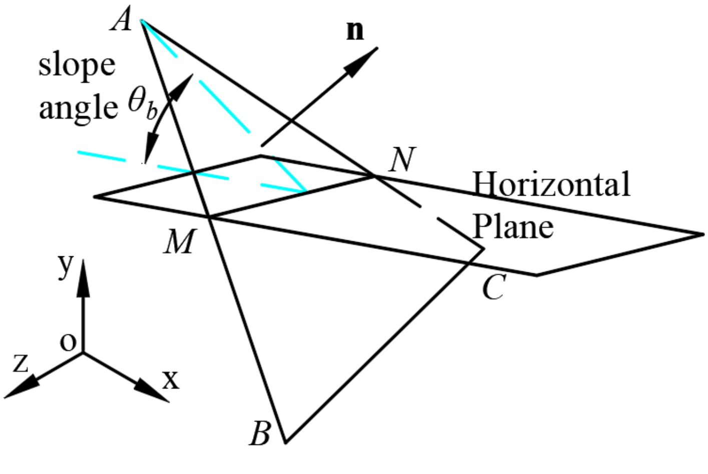

Figure 4.4 Slope angle θ_b of triangle ABC

However, not all cells have three neighboring cells, as some cells, such as boundary cells, may have only two neighboring cells or, even one neighboring cell at sharp corners. Additionally, there are cases where two adjacent cells have one that is rigid base rock and the other is sediment that can be eroded. These situations all require specific treatment.

4.2.2.2. Calculation of mass failure

Once the slope angle θ_b of each bed surface cell is obtained, it can be compared to the critical slope angle, θ_{cs} or θ_{ce} depending on the bed surface below or above the water surface, to check the stability of all bed surface cells. If the slope angle θ_b of the cell o in Figure 4.3 exceeds the critical angle θ_c, bank mass failure occurs. As plotted schematically in Figure 4.5, the mass failure is completed by rotating the triangle ABC around a horizontal axis MN to the new plane triangle $A'B'C'$ until the slope angle θ_b reaching the residual angle θ_r, that is the sediment in the upper area (cell a in the case of Figure 4.5) is instantaneously transported to the lower area (cell b and cell c).

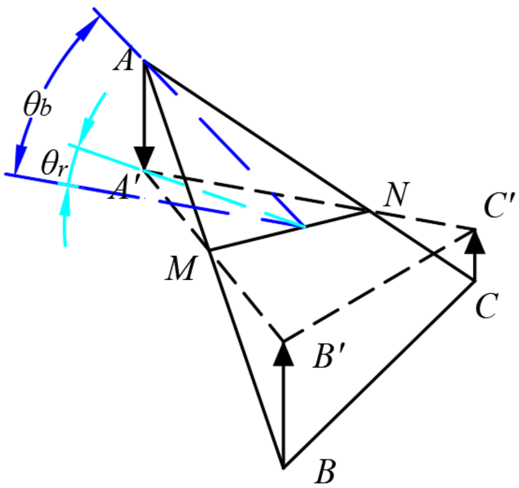

Figure 4.5 Rotation of triangle ABC
(ABC is the unstable plane before the mass failure, $A'B'C'$ is the stable plane after the mass failure)

Through this process, the stability of a cell o is maintained by adjusting the elevation of its neighboring cells. However, this process must keep sediment mass conservation:

$$\Delta z_{ao}S_a + \Delta z_{bo}S_b + \Delta z_{co}S_c = 0 \tag{4.4}$$

where, Δz_{ao}, Δz_{bo}, Δz_{co} are the bed elevation variations of cells a, b, c, respectively, after the mass failure of cell o; S_a, S_b, S_c are the horizontal projected areas of cells a, b, c, respectively.

This requires the horizontal axis MN to be at a proper level. Based on the similarity of triangles, the following condition is satisfied when triangle ABC is rotated around axis MN.

$$\frac{z_a - z_{MN}}{\Delta z_{ao}} = \frac{z_b - z_{MN}}{\Delta z_{bo}} = \frac{z_c - z_{MN}}{\Delta z_{co}} \tag{4.5}$$

where, z_{MN} is the elevation of the axis MN; z_a, z_b, z_c are the bed elevations of cells a, b, c, respectively.

According to these two conditions, the location of the horizontal axis MN can be determined:

$$z_{MN} = \frac{z_a S_a + z_b S_b + z_c S_c}{S_a + S_b + S_c} \tag{4.6}$$

Subsequently, we can obtain the elevation changes in cells a, b and c during the mass failure calculation of cell o:

$$\Delta z_{io} = \left(1 - \frac{\tan\theta_r}{\tan\theta_b}\right)(z_{MN} - z_i), i = a, b, c \tag{4.7}$$

Generally, a cell has three neighboring cells, which means that it may participate in the mass failure calculation of multiple cells at the same time. For example, cell o will participate in the stability calculation of cells a, b and c (Figure 4.3), so the total elevation variation of cell o is given by:

$$\Delta z_o = \Delta z_{oa} + \Delta z_{ob} + \Delta z_{oc} \tag{4.8}$$

where, Δz_o is the total elevation variation in a mass failure computation; Δz_{oa}, Δz_{ob}, Δz_{oc} are the bed elevation variations of cell o due to the mass failure of cells a, b, c, respectively.

However, the summation in equation (4.8) may lead to the emergence of unreasonably large elevation increases or decreases. For example, if both neighboring cells a and b of cell o collapse simultaneously, and the elevation of cell o is lower than a and b, this will result in two elevation increases for cell o, and the superposition of these two could potentially cause an excessively high elevation in cell o.

To address this issue, in this study, each cell is divided into three equal parts and only one-third of the sediment will be involved in the mass failure calculation of the corresponding neighboring cells. During the mass failure calculation, each of the three parts of every cell is independent and has its own distinct level, which is initially the same. In the end, after the mass failure calculation, the final elevation change of each cell is determined by summarizing the changes in sediment volume based on the elevation changes of its three parts. This effectively introduces damping to the elevation changes, increasing computational stability. As shown in Figure 4.6, a bed surface cell o is divided into OIJ, OIK and OJK, and when its neighboring cell a is unstable, only the sediment in triangle OIJ will be included in the mass failure calculation of the cell a. Therefore, the sediment volume variation of cell o during this event is:

$$\Delta V_{oa} = \Delta z_{oa} S_{OIJ} = \frac{1}{3}\Delta z_{oa} S_o \tag{4.9}$$

where, ΔV_{oa} is the sediment volume variation of cell o involved in the mas failure calculation of cell a; S_o is the horizontal projected area of cell o; S_{OIJ} is the horizontal projected area of triangle OIJ, $= \frac{1}{3}S_o$.

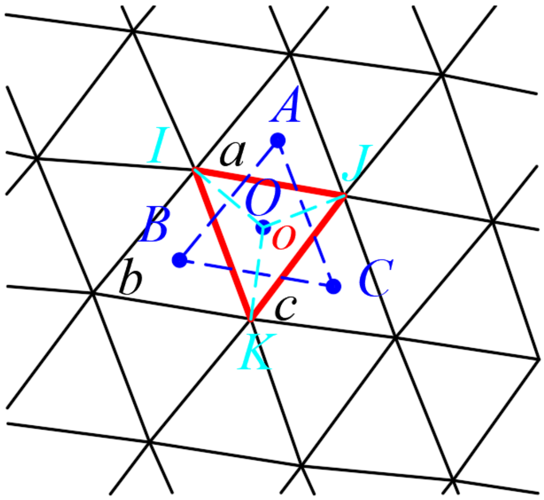

Figure 4.6 Plan view of the division of a bed surface cell o when participating in the mass failure computation of neighboring cells

(O is the centroid of cell o; I, J and K are three nodes of cell o)

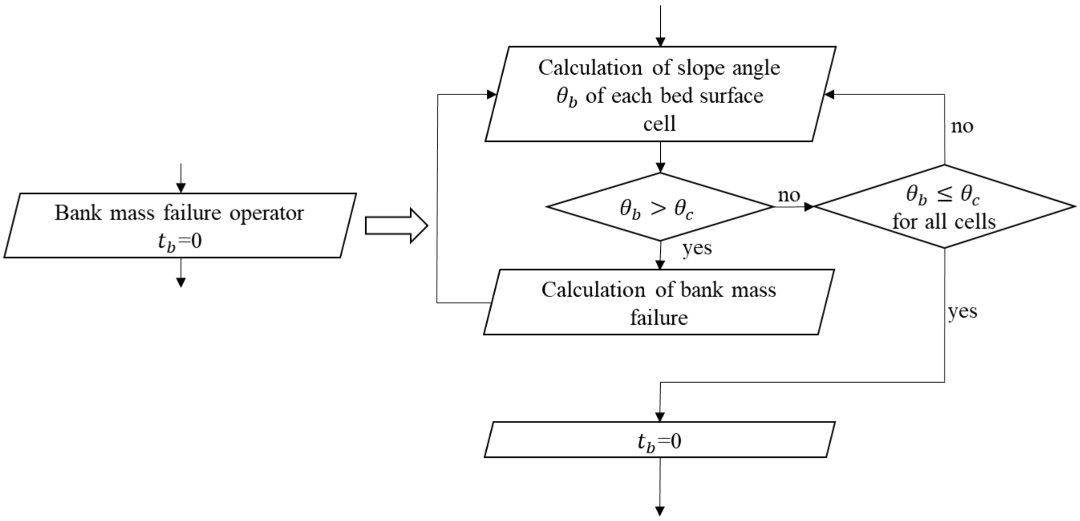

Figure 4.7 Flow chart of bank mass failure operator (a component of Figure 2.4)

Since each cell is divided into thirds equally, equations (4.4), (4.5), (4.6) and (4.7) remain valid and the equation (4.8) is replaced by the following:

$$\Delta z_o = \frac{\Delta V_{oa} + \Delta V_{ob} + \Delta V_{oc}}{S_o} = \frac{1}{3}(\Delta z_{oa} + \Delta z_{ob} + \Delta z_{oc}) \tag{4.10}$$

where, ΔV_{ob}, ΔV_{ob} ΔV_{oc} are the sediment volume variation of cell o involved in the mass failure calculations of cells a, b and c, respectively.

The above stability check and mass failure calculation are performed for all bed surface cells, eliminating the necessity to explicitly identify the location of the riverbank. Similar to the cross-section profile adjustment in Figure 4.2, the rotation of a bed surface cell could potentially affect the stability of its adjacent cells. Therefore, in a bank mass failure operator loop, the above process is necessary to be repeated until the slope angle of every bed surface cell is smaller than the critical angle, as illustrated in Figure 4.7.

Since the time scale of the bank erosion process is generally much longer than that of the fluvial erosion process, the time step for a bank mass failure model is typically much larger than that employed in the sediment transport calculation (Lai, 2017). Lai (Lai, 2017) used a time step of 3600 s for the bank erosion model and a time step of 5 s for the fluvial erosion model. Swartenbroekx et al. (Swartenbroekx et al., 2010) thought the time step for bank mass failure could be regarded as a failure rate affected by bank material properties and vegetation, and it was required to be calibrated. Nonetheless, they applied their bank erosion model once every 50 fluvial erosion model time steps without calibration due to the lack of experimental data. Different form them, Abderrezzak et al. (Abderrezzak et al., 2016) employed the same time step for all modules, but they did not ensure that a new stable geometry was achieved in one single time step. As presented in Figure 2.4, we adopted the same approach as the former two studies, using a larger time step for the bank mass failure.

4.3. Validation 1: Dam-break flow in a straight flume

In this section, the laboratory experiment undertaken by Soares-Frazão et al. (Soares-Frazão et al., 2007) was simulated. The experiment demonstrated the bank failure process induced by rising water levels caused by the dam-break flow in a straight channel. The purpose of the numerical simulation is to evaluate the model performance in reproducing not only the final cross-section profiles but also the temporal variations. The measurement data of this experiment for comparison are available online as the electronic supplement to the original paper of Soares-Frazão et al. (Soares-Frazão et al., 2007).

4.3.1. Experimental setup

Soares-Frazão et al. (Soares-Frazão et al., 2007) conducted the experiment in a horizontal halfwidth channel. Its dimensions are presented in Figure 4.8. As indicated in the perspective view and cross-section, one side of the channel was a vertical glass wall, while the other side was a trapezoidal bank with an initial slope of 50° and a height of 16 cm. There was a gate in the middle part of the channel. Downstream of the gate, the bank was erodible, while the bank upstream of the gate was rigid to limit the flow at the beginning of the erodible bank. The channel bed was also erodible with an initial thickness of 8 cm. Both the erodible bank and bed consisted of uniform coarse sand with a median diameter d_{50} of 1.8 mm, a density of 2615 $\mathrm{kg/m^3}$ and a porosity of 0.405. There was a tank at the upstream end of the channel, initially full of water with a level of 15 cm, while downstream of the gate, there was no water. As the experiment began, the gate was suddenly lifted to simulate the dam-break flow. Downstream of the gate, as the water level rose, the bank mass failure was observed.

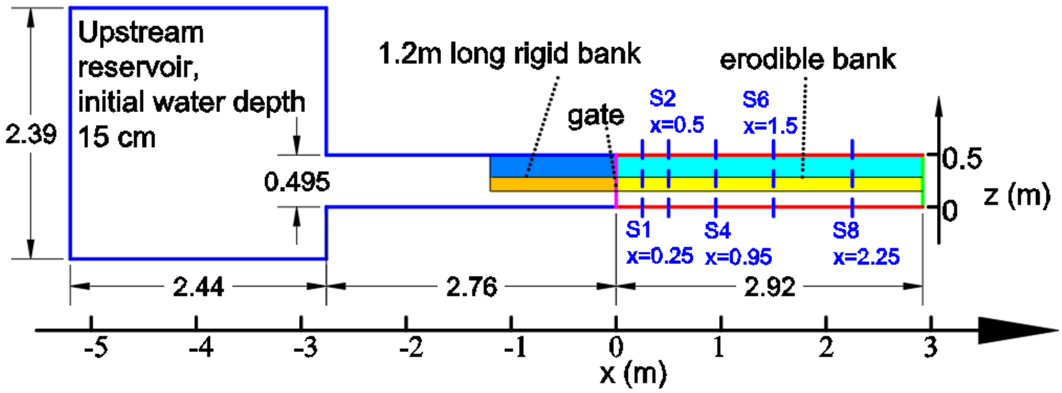

(a) Plan view

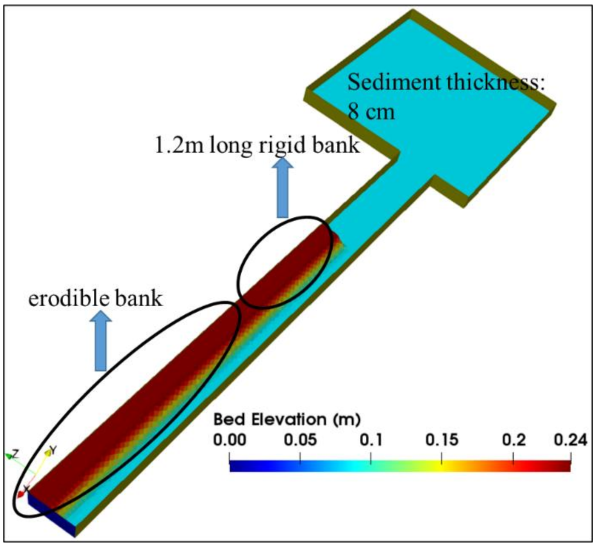

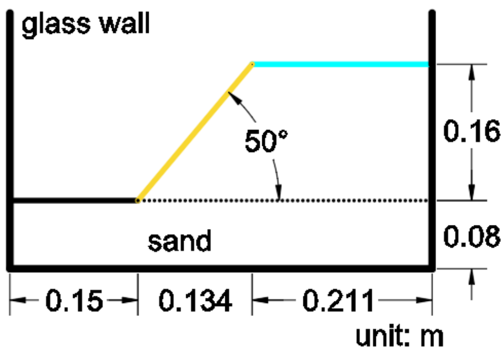

(b) Perspective view

(c) Cross-section

Figure 4.8 Experimental setup of the experiment by Soares-Frazão et al. (Soares-Frazão et al., 2007)

The observed cross-section profiles for five sections, namely S1, S2, S4, S6, and S8 (depicted in the plan view in Figure 4.8) at five moments (1 s, 3 s, 5 s, 10 s, and 15 s) have been provided online. Based on the observed cross-section profiles, in this simulation, the submerged residual angle (θ_{rs}) and critical angle (θ_{cs}) ware designated as 22° and 27°, respectively.

4.3.2. Results and discussions

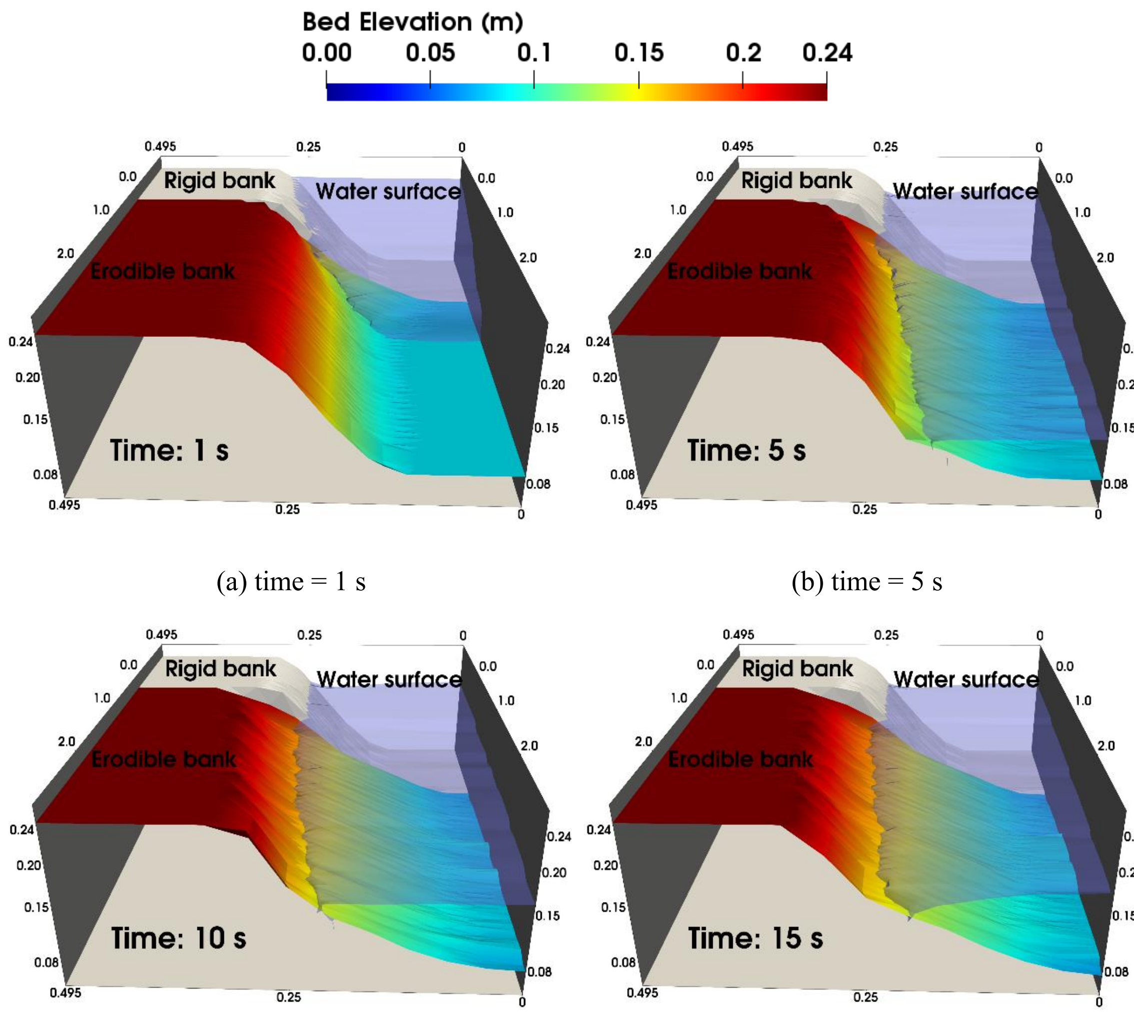

(a) time = 1 s

(b) time = 5 s

(c) time = 10 s

(d) time = 15 s

Figure 4.9 Simulated bed topography evolution

The simulated channel evolution in time is presented in Figure 4.9. As the dam-break flow propagated down the channel, the water level rose, gradually submerging the bank. The critical stable slope angle of the submerged portion decreased, triggering the bank mass failure operator successfully. As a result, the dam toe extended towards the channel center, and the bank top retreated, with this channel enlargement being most pronounced in the immediate vicinity of the gate. It was noticeable that there were distinct differences in the slope angles above and below the water surface due to different critical angles.

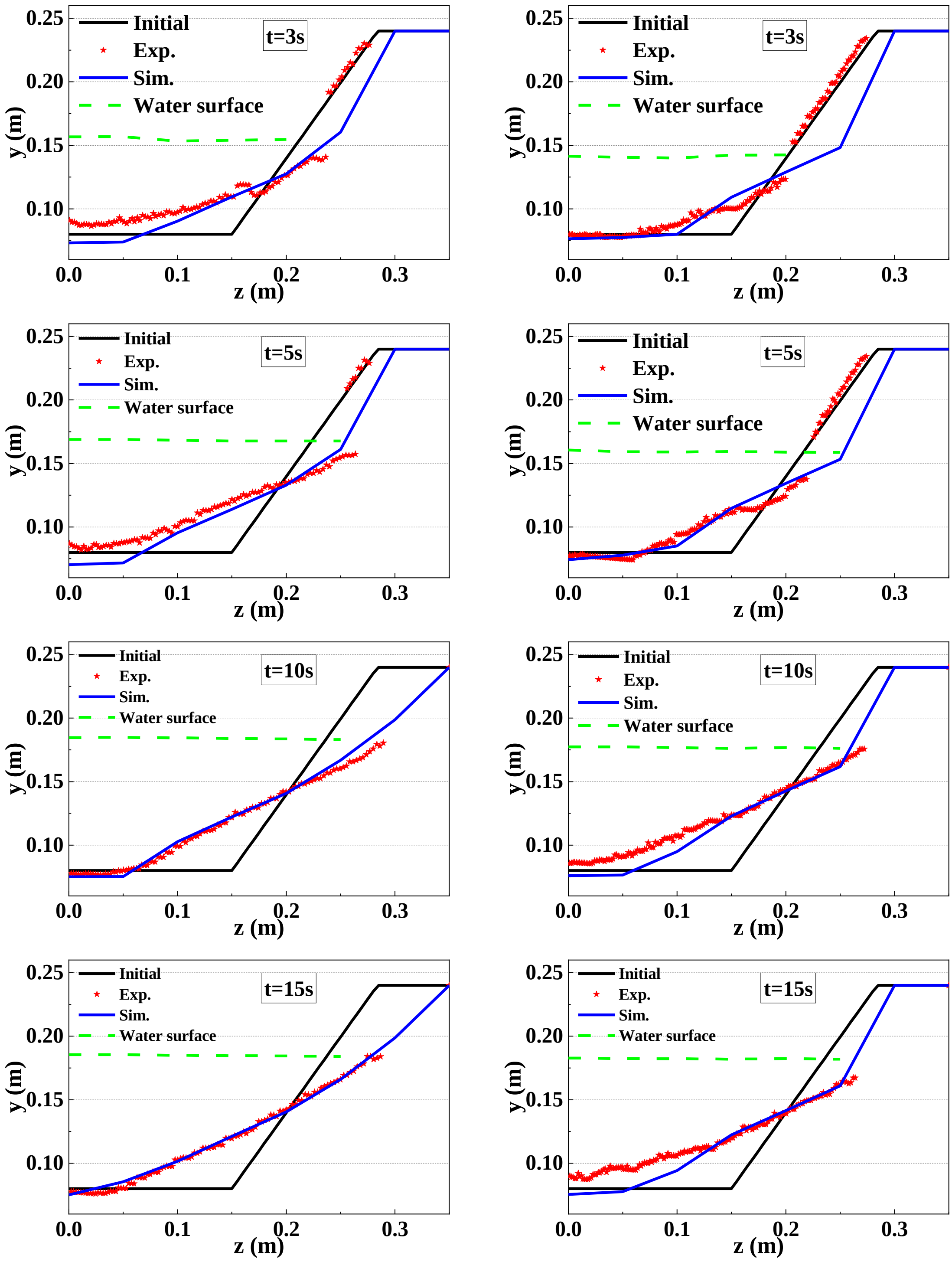

(a) S2 (x = 0.5 m) (b) S4 (x = 0.95 m)

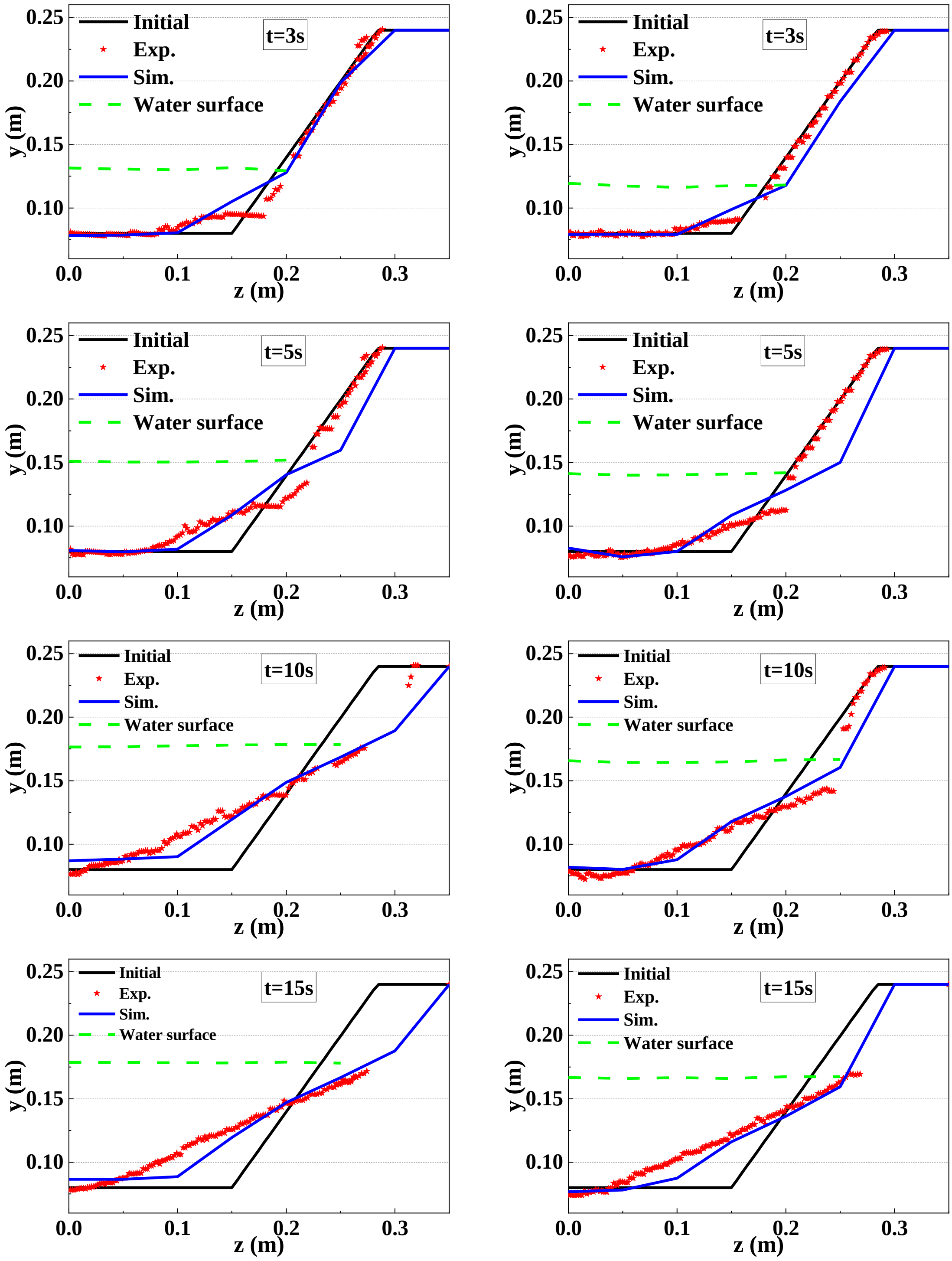

(c) S6 (x = 1.5 m) (d) S8 (x = 2.25 m)

Figure 4.10 Comparison of measured and simulated cross-section evolution

The observed cross-section evolution of Soares-Frazão et al. (Soares-Frazão et al., 2007), simulated cross-section evolution, and water surface were summarized in Figure 4.10. They were compared at four sections, namely S2, S4, S6, and S8, located 0.5 m, 0.95 m, 1.5

m, and 2.25 m downstream of the gate, and at four times of 3 s, 5 s, 10 s, 15 s. The simulated variations in cross-section profiles over time for these sections aligned well with the experimental results, particularly in capturing the final shape at the time of 15 s. However, the degradation in the middle part of the channel (in the vicinity of z = 0 m) was overpredicted, likely stemming from an overestimation of bed load transport (Figure 4.10, (a) t = 3 s, 5 s; (b) t = 10 s, 15 s; (c) t = 10 s, 15 s; (d) t =15s). Besides, in the early stage, the simulated bank mass failure was slightly overestimated, resulting in a greater retreat of the bank top than observations (Figure 4.10, (a) t = 3 s; (b) t = 3 s, 5 s; (c) t = 5 s; (d) t =5s).

Table 4.1 RMSE for four sections at four times

Cross-section	Model	3 s	5 s	10 s	15 s
S2	This study	0.014	0.017	**0.004**	0.003
	2D simulation (Evangelista et al. (2015))	0.012	**0.011**	0.006	-
	2D simulation (Swartenbroekx et al. (2010))	**0.011**	0.012	0.007	-
S4	This study	0.014	0.014	0.008	0.011
	2D simulation (Evangelista et al. (2015))	**0.006**	**0.004**	**0.006**	-
S6	This study	0.008	0.012	**0.007**	0.008
	2D simulation (Evangelista et al. (2015))	**0.006**	**0.009**	**0.007**	-
	2D simulation (Swartenbroekx et al. (2010))	**0.006**	0.012	0.009	-
S8	This study	0.004	0.010	0.016	0.006

Table 4.2 BSS of final cross-section profiles at the time of 15 s

Cross-section	S2	S4	S6	S8
BSS	0.98	0.81	0.92	0.92

In order to quantitatively assess the model performance, values of the root mean squared error (RMSE) for these four sections at the four times were listed in Table 4.1. For comparison, the computed results of Swartenbroekx et al. (Swartenbroekx et al., 2010) and Evangelista et al. (Evangelista et al., 2015) from their respective 2D models were also presented in the table. Turbulence, in-stream structures, and suspended load were not included in their 2D models. It can be seen that the current model has a similar performance.

In addition, the Brier Skill Score (BSS) was also calculated for the final cross-section profiles at the time of 15 s (Table 4.2). The BSS is defined as (Abderrezzak et al., 2016; Sutherland et al., 2004; van Rijn et al., 2003):

$$BBS = 1 - \frac{\sum_{i=1}^{N_m}\left(z_{bi,mes}-z_{bi,sim}\right)^2}{\sum_{i=1}^{N_m}\left(z_{bi,mes}-z_{bi,0}\right)^2} \tag{4.11}$$

where, $z_{bi,mes}$ is the measured bed level; $z_{bi,sim}$ is the simulated bed level; $z_{bi,0}$ is the initial bed level; N_m is the total number of measurements. The BSS, which compares the mean squared difference between the measured results and simulated results, with the mean squared difference between the measured results and the initial bed topography to evaluate whether the simulated results are closer to the measured results than the initial bed topography, serves as a useful performance indicator for evaluating morphodynamic models in coastal engineering. van Rijn et al. (van Rijn et al., 2003) have given the value ranges for qualification: 1.0 ~ 0.8 for excellent, 0.8 ~ 0.6 for good, 0.6 ~ 0.3 for reasonable/fair, 0 ~ 0.3 for poor and negative values for bad. As shown in Table 4.2, the current model reproduced accurately the final bed topography at the time of 15 s.

4.4. Validation 2: Meandering channel migration

In this section, we simulated two laboratory experiments conducted by Karki (Karki, 2019). These experiments were performed in a meandering channel with both erodible banks and an erodible bed under steady inflow, one without spur dikes and the other with spur dikes. The two numerical simulations aimed to evaluate the model performance in predicting not only the planform evolution of meandering channels without in-stream structures but also in scenarios involving spur dikes.

4.4.1. Without spur dikes

4.4.1.1. Experiment setup

The meandering channel was excavated within a 400 cm long and 200 cm wide platform filled with non-cohesive sediment with a median grain size of 0.72 mm and a density of 1410 $\mathrm{kg/m^3}$. The width of the simulation domain was reduced based on the final channel planform to decrease the number of mesh cells and save computational time. As depicted in Figure 4.11, there were four consecutive meanders, the axis of which consisted of arcs and straight lines. The upstream and downstream ends were connected to rigid straight channels with lengths of 0.5 m and 1 m, respectively. The initial channel was 20 cm wide and 6 cm high and had an initial slope of 1:550. The experiment was performed under a constant inflow discharge of 0.95 l/s and without sediment feed for a duration of 60 min.

At the beginning of the experiment, the water gradually entered the inlet and the flowrate increased from zero to constant. The entire experiment of 60 min was not continuous. Instead, the inflow was stopped every 20 min and the bed topography was measured after the bed became dry.

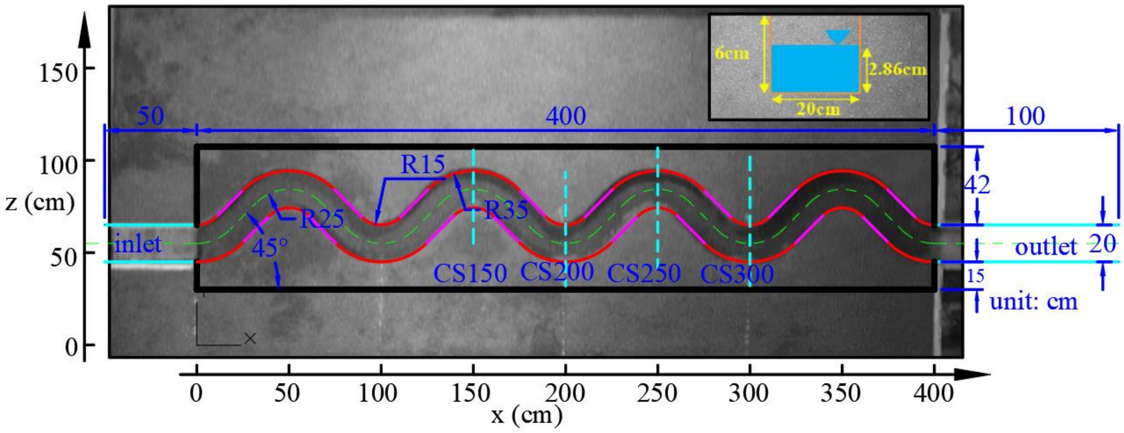

Figure 4.11 Channel geometry of the experiment by Karki (Karki, 2019)

4.4.1.2. Results and discussions

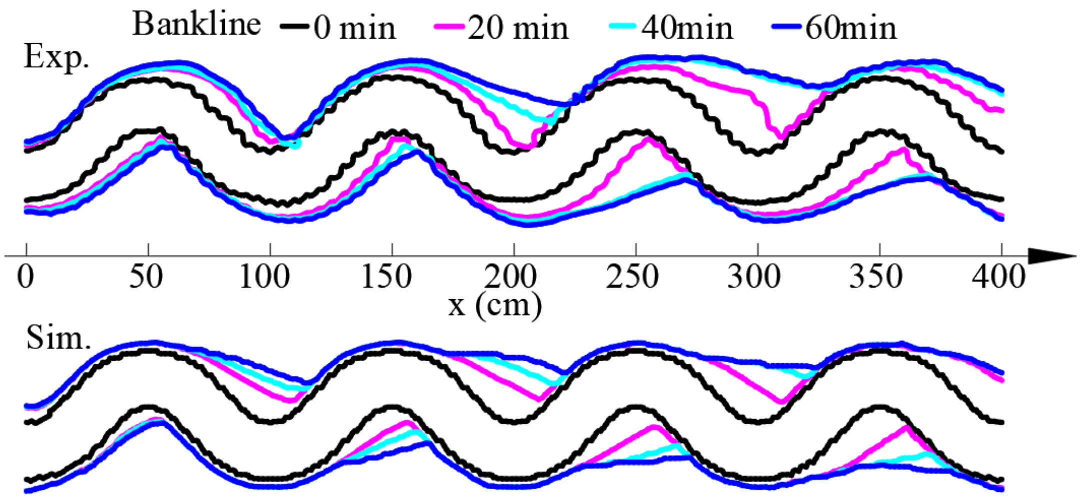

Figure 4.12 Comparison of observed and simulated temporal bankline variations

Figure 4.12 shows the initial banklines as well as the observed and simulated temporal changes in banklines at three moments of 20 min, 40 min, and 60 min. In this comparison, the contour line with a bed elevation of 5 cm was taken as the bankline. Although the bank retreat near the apex of outer banks was underestimated, the model reproduced the bank retreat at the apex of inner banks and captured certain features of the bankline evolution over time in the experiment. For example, the extent of bankline shifting increased from upstream to downstream. In the first 20 min and 40 min, the bank retreat is more pronounced compared to the last 20 min, indicating a decreasing rate of bank retreat over time, particularly in the downstream meanders.

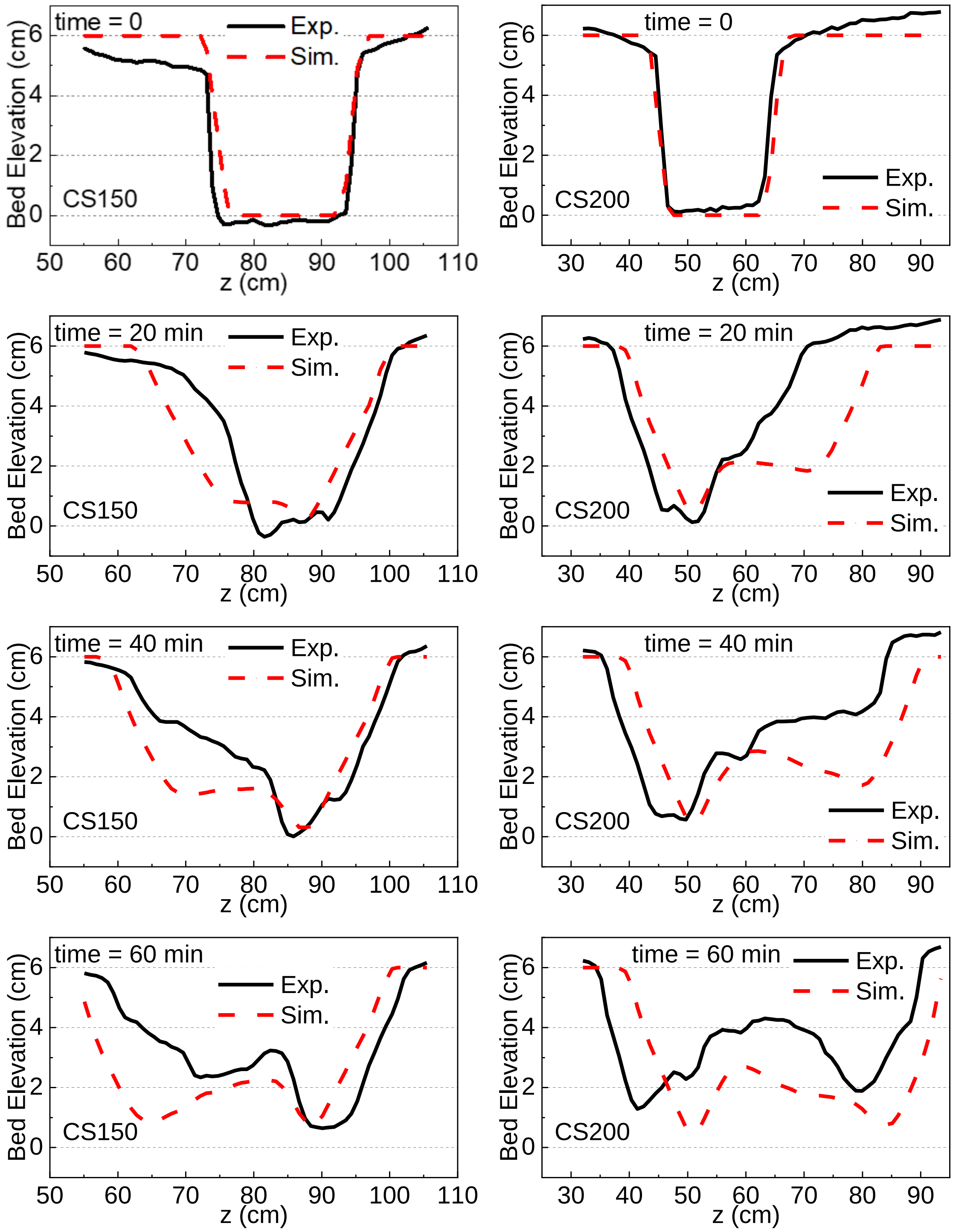

a) CS150 b) CS200

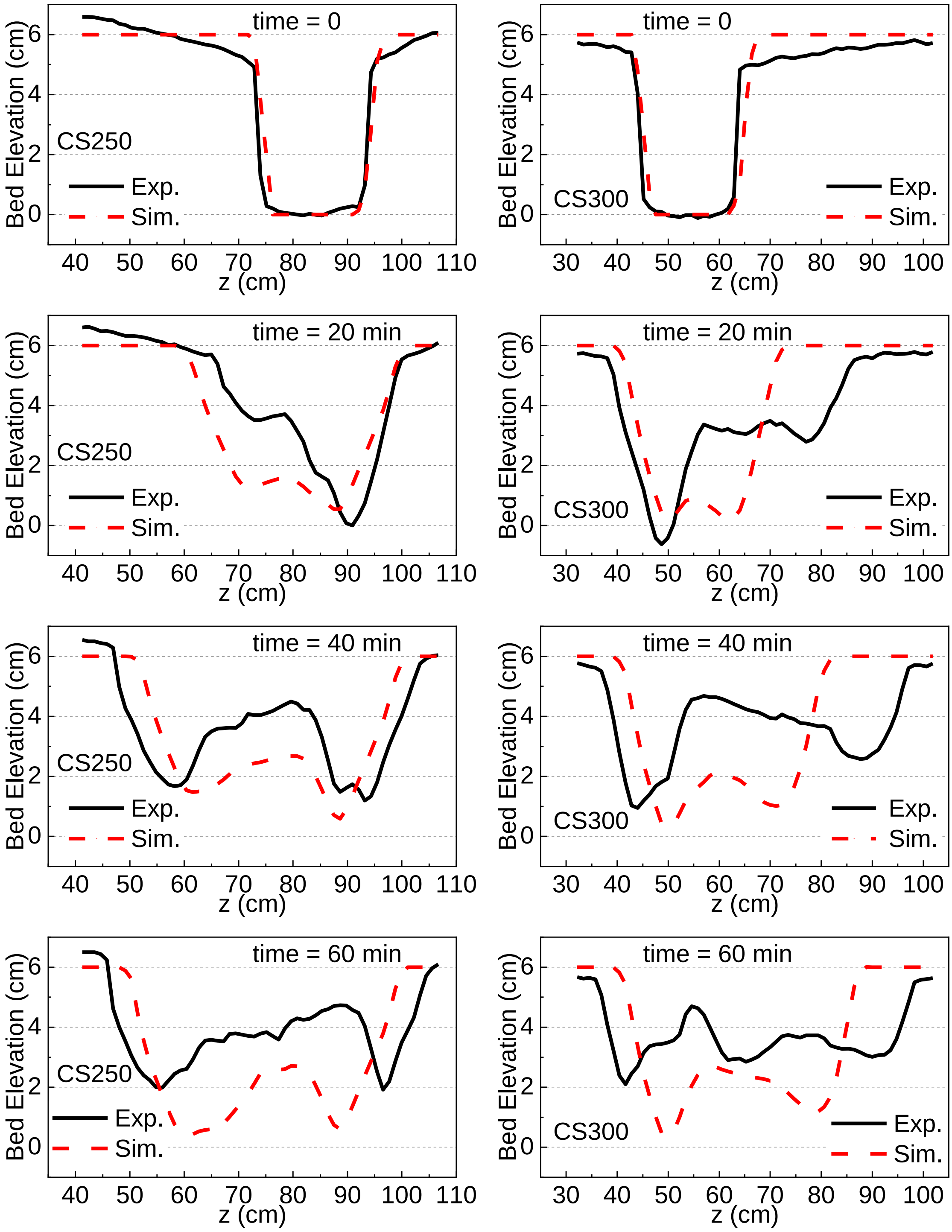

c) CS250 d) CS300

Figure 4.13 Comparison of observed and simulated cross-section evolution

The simulated cross-section profiles at different moments of 20 min, 40 min, and 60 min for four sections at x = 150 m (CS150), 200 m (CS200), 250 m (CS250), and 300 m (CS300) (see Figure 4.11 for locations) were compared with the observed cross-section profiles in Figure 4.13. The small values on the horizontal axis represent the right bank, while the large values represent the left bank. The shapes of cross-sections were basically consistent, although there were certain numerical differences in bed elevation. For CS150 and CS200, the erosion at the inner bank (right bank for CS150 and left bank for CS200) was overestimated. For CS250 and CS300, bank erosion as well as the aggradation in the channel was underestimated. However, in most cases, the position and elevation of the lowest point in cross-sections were fairly close to the experimental results.

Table 4.3 BSS of final cross-section profiles at the time of 60 min

Cross-section	CS150	CS200	CS250	CS300
BSS	0.33	0.56	0.53	0.40

Similar to before, for quantifying the performance of the numerical model, the BSS values for the final shapes of the four sections at 60 min were calculated. As shown in Table 4.3, the BBS values fell within the range of 0.3 to 0.6. According to the criteria of van Rijn et al. (van Rijn et al., 2003), the numerical reproduction of the final cross-section profiles can be considered reasonable or fair.

4.4.2. With spur dikes

4.4.2.1. Experiment setup

Figure 4.14 Photo of experimental channel with spur dikes (source: (Karki, 2019))

The channel geometry, boundary conditions, and procedures of this experiment were identical to the previous experiment, with the exception that a series of spur dikes were installed in the middle meanders of the channel, as shown in Figure 4.14. As plotted in Figure 4.15, rectangular spur dikes were inserted into the sediment with a spacing of 6 cm between them. The initial length of the part of spur dikes within the channel was set to 3 cm, and the crests of the spur dikes were level with the banks.

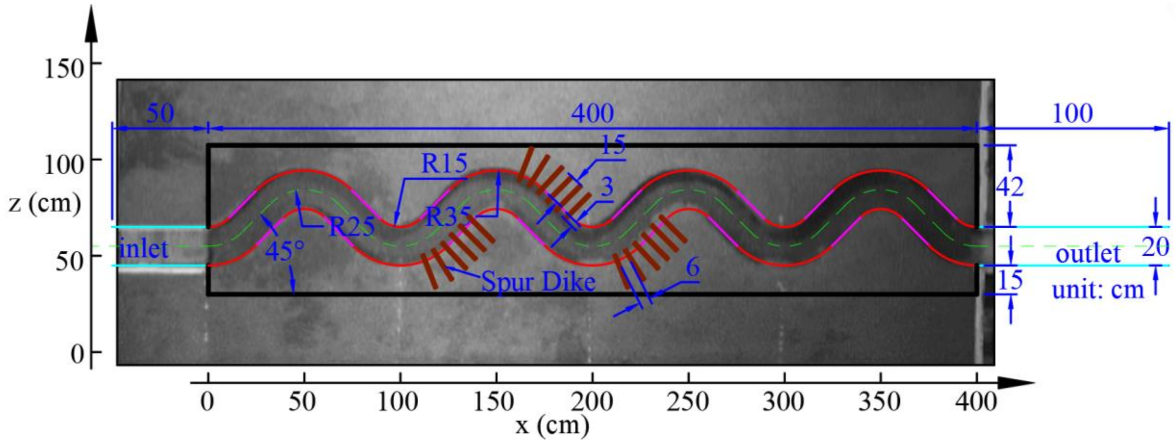

Figure 4.15 Channel geometry and arrangement of spur dikes in the experiment of Karki (Karki, 2019)

4.4.2.2. Results and discussions

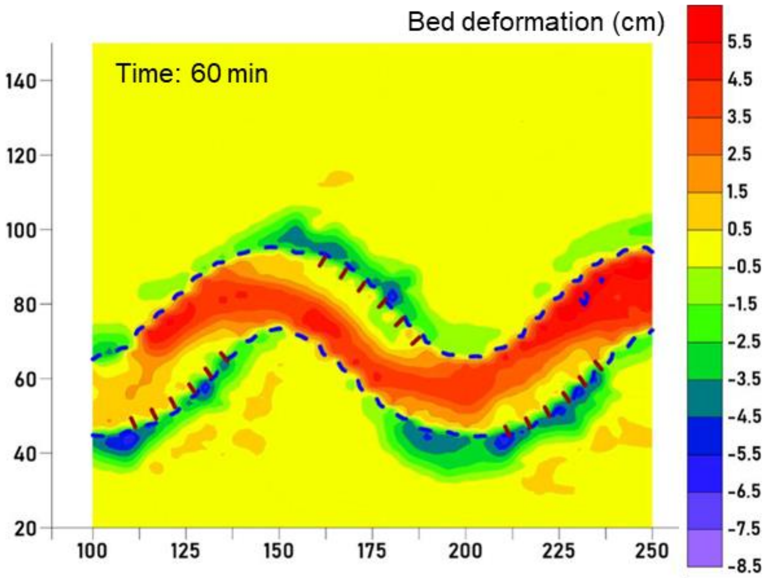

Figure 4.16 Experimental bed deformation at 60 min (source: (Karki, 2019))

The experimental result and simulated result of the final bed deformation in the part installed spur dikes at 60 min are presented in Figure 4.16 and Figure 4.17, respectively, for comparison. The local scour in the vicinity of the spur dike tips and the slight bank retreat in outer banks, where spur dikes were installed, due to the initial vertical walls, were reproduced in a reasonable manner. However, the simulated erosion areas in the original channel were located further downstream than the experimental result, and the erosion in the apex of outer banks near the first spur dikes was not captured. The calculated erosion at x = 100 m was much more severe than the observed results.

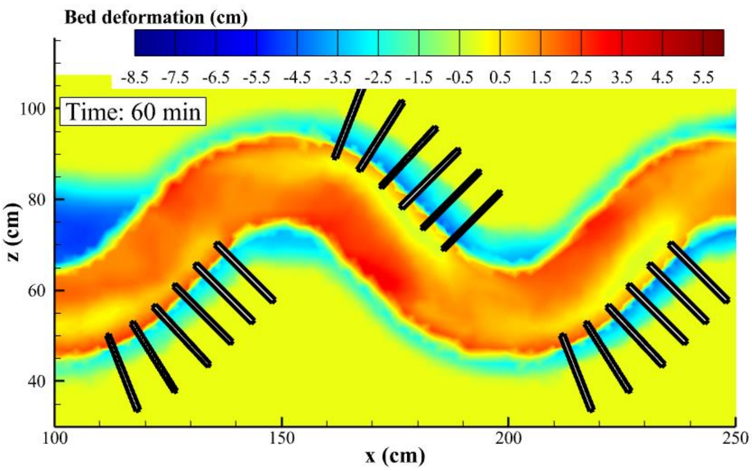

Figure 4.17 Simulated bed deformation at 60 min

However, the simulation conditions and experimental conditions are difficult to be exactly the same. For example, as mentioned earlier, in the experiment, the inflow was stopped every 20 minutes, allowing the channel to dry for topography measurements, but there was no such process in the simulation. The experiment started with zero water depth in the channel, whereas in the simulation, an initial water level was set. All of these factors could lead to errors. In addition, some parameters such as critical slope angle, residual slope angle, bank failure time step, and bed shear stress might be adjusted through calibration against this experiment to enhance the results.

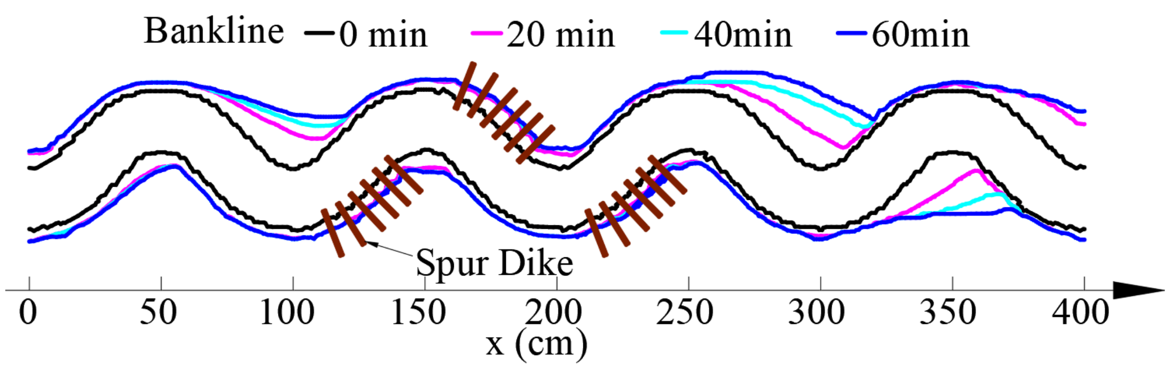

Figure 4.18 Simulated temporal bankline variations with spur dikes

The simulated bankline shifting over time was also plotted in Figure 4.18. In comparison to the results without spur dikes in Figure 4.12, it can be observed that the installation of spur dikes effectively retrained the outer bank retreat, providing protection to banks.

4.5. Summary

In this chapter, a new OpenFOAM solver considering bank erosion was developed by incorporating a bank mass failure operator into the 3D numerical model introduced in Chapter 2. The bank mass failure operator compares the local slope angle of each bed surface cell with the submerged critical angle or emerged critical angle depending on the water depth to determine the stability of this cell and then simulates the collapse by rotating unstable cells. This method can eliminate the necessity to explicitly identify the location of the riverbank, greatly enhancing its convenience.

We have conducted validation for the bank mass failure operator through three experiments: a straight channel dam break experiment, a meandering channel experiment without spur dikes, and a meandering channel experiment with spur dikes. For the first one, both the cross-section profile evolution and final profiles matched well. For the second one, the simulated bankline shifting had good agreement with the observations and the final cross-section profiles were simulated in a reasonable manner. For the last one, the bank retreat in the area installed spur dikes and the local scour around spur dike tips satisfactorily matched the measurements. As a result, it can be concluded that the model can be employed to evaluate the performance of spur dikes against bank erosion and to investigate the temporal changes of planform in a meandering channel.

Chapter 5.
Field application in Uji River

5.1. Introduction

In the previous chapter, the OpenFOAM solver considering bank erosion has been developed and validated with experimental data. In this chapter, the field application of this model was conducted in Uji River, where severe bank erosion occurred in the bend 43 km away from the river mouth.

At first, we reproduced a flood event with the aim of analyzing the causes of the severe bank erosion. Then, two cases with spacings of $2b$, $4b$, respectively, were simulated. The near-bed velocities were compared and the aquatic habitat evaluation for Zacco platypus (dominant species in the river basin) was performed.

5.2. Study area

Uji River is a major river in the Yodo River system, originating from Lake Biwa, the largest lake in Japan (Figure 5.1). It is commonly referred to as the Yodo River and also specifically denotes the 16.2 km long river reach from the confluence section of the Uji River, Katsura River, and Kizu River, located 37.0 km away from the river mouth to the Amagase Dam at a distance of 53.2 km from the river mouth.

Based on the results of cross-sectional topographic surveys, Azuma and Sekiguchi (Azuma and Sekiguchi, 2008) calculated the sediment balance in the Uji River. According to their findings, over the 38-year period from 1967 to 2006, the sediment volume of the riverbed decreased by $3.09 \times 10^6\ \mathrm{m}^3$. As a result, there was a significant trend of riverbed lowering in the downstream area of the Uji River, particularly pronounced near the section 43.0 km away from the river mouth (CS43), where the bank retreated by approximately 70 m at maximum. Aly El-Dien (Aly El-Dien, 2016) analyzed the satellite images of Google Earth from 2004 to 2015, concluding that the maximum retreat distance of the riverbank is approximately 44 meters, with an average erosion rate of about 4 m per year. Karki (Karki, 2019) also analyzed the satellite images from 2004 to 2018 and obtained similar results.

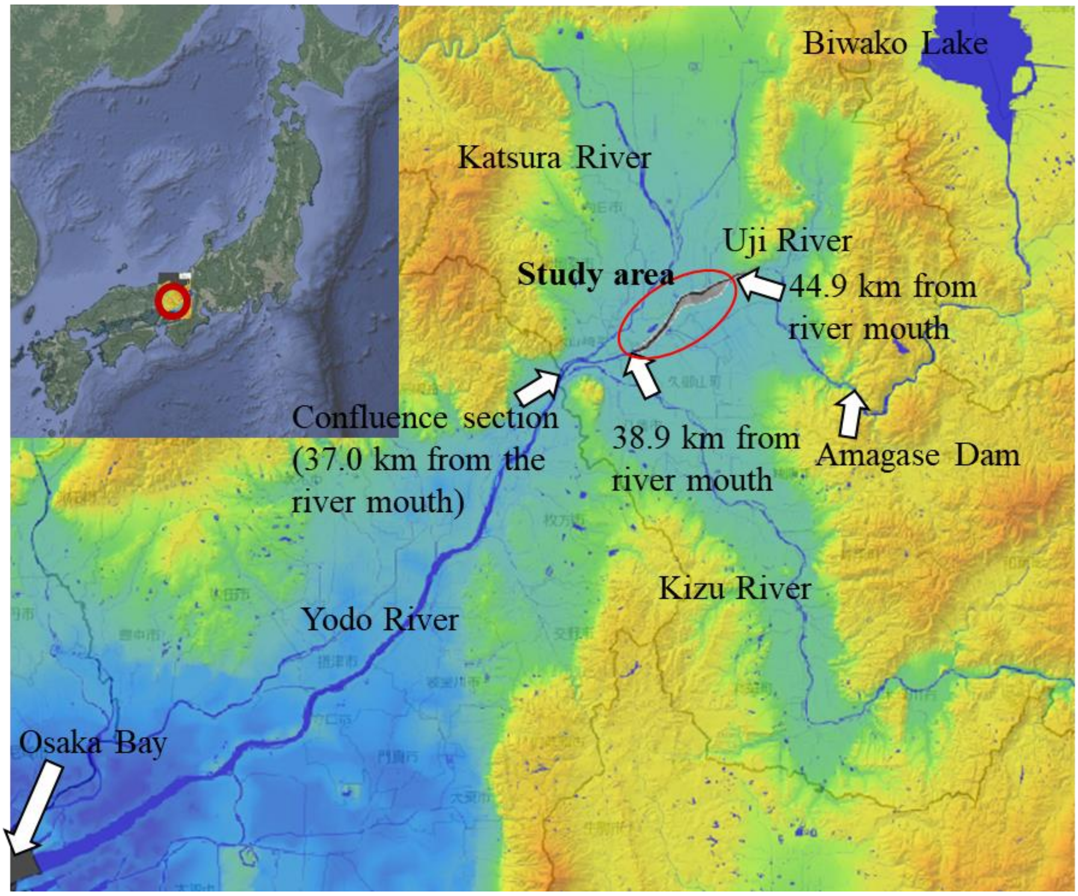

Figure 5.1 Map of Uji River and location of study area (source: GSI Maps)

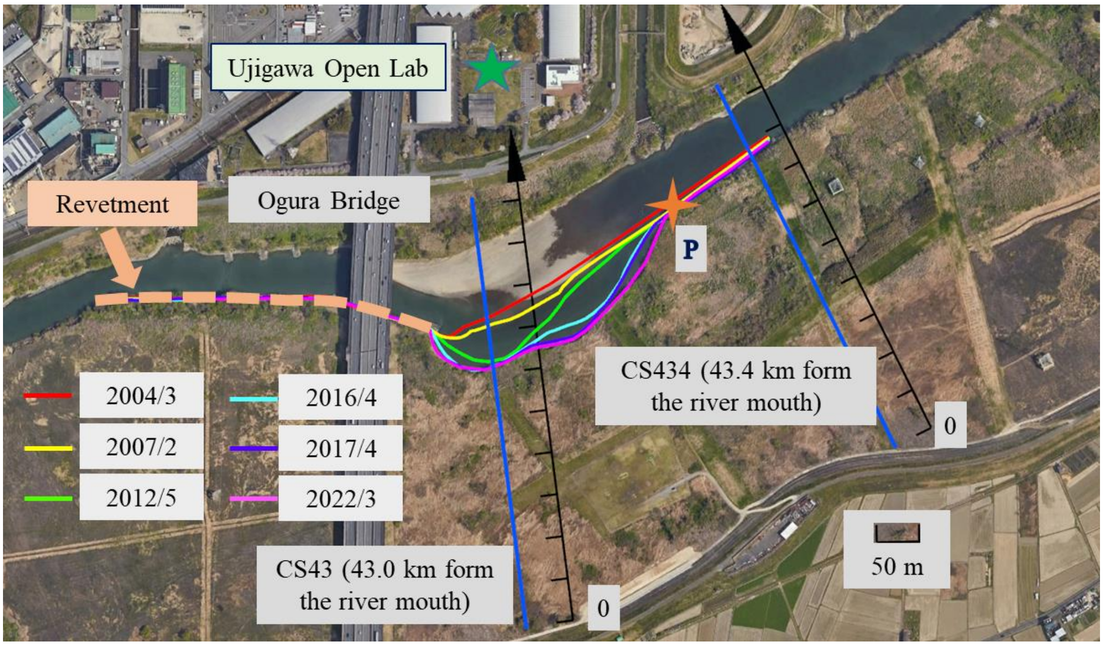

Figure 5.2 Bank erosion around CS43 (the section 43.0 km away from the river mouth) from 2004 to 2022 (source: Google Earth)

As shown in Figure 5.2, the CS43 is located upstream of the Ogura Bridge of the Second Keihan Highway, beside the Ujigawa Open Laboratory and the reclaimed land of old Ogura Pond. Downstream of the CS43, revetments were constructed along a segment of the left bank of the main channel to protect the bridge piers. Bankline evolution from 2004 to 2022 was plotted in Figure 5.2. The bank erosion in the area near the CS43 was extremely severe. The erosion rate was not uniform in space and time, for example, at the CS43, it was very significant between 2007 and 2012, while at an upstream section, it was most pronounced between 2012 and 2016.

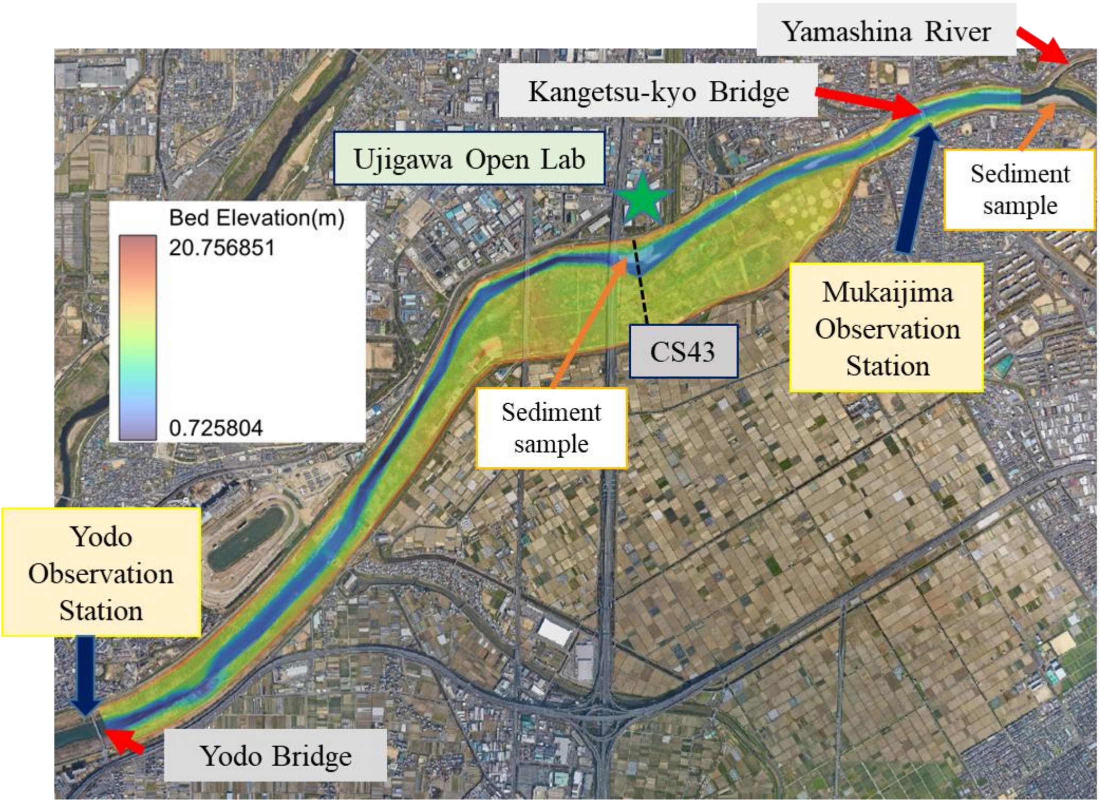

Figure 5.3 Locations of observation station and bathymetry of study area (source: Google Earth)

As shown in Figure 5.3, in the vicinity of this area, the nearest upstream observation station is the Mukaijima Observation Station, located just upstream of the Kangetsu-kyo Bridge on the left bank of the river, 44.9 km away from the river mouth. The nearest downstream observation station is the Yodo Observation Station, situated just downstream of the Yodo Bridge on the right bank of the river, 38.9 km away from the river mouth. Both observation stations can provide continuous hourly water level and flowrate data. Therefore, this study selected the 6.0 km long river reach between these two observation stations as the study area. The simulation domain includes the region between the leaves on both sides of this reach.

Based on the cross-sectional topographical data measured at intervals of 200 m in January 2016, Karki (Karki, 2019) generated the river bathymetry presented in Figure 5.3. This was achieved through spatial interpolation using the HEC-GeoRAS application in the ArcGIS interface. Therefore, the simulations in this chapter were conducted based on this topography for the year 2016. The observed hourly flow rates and water levels for these two observation stations in 2016 were graphically depicted in Figure 5.4 and Figure 5.5, respectively.

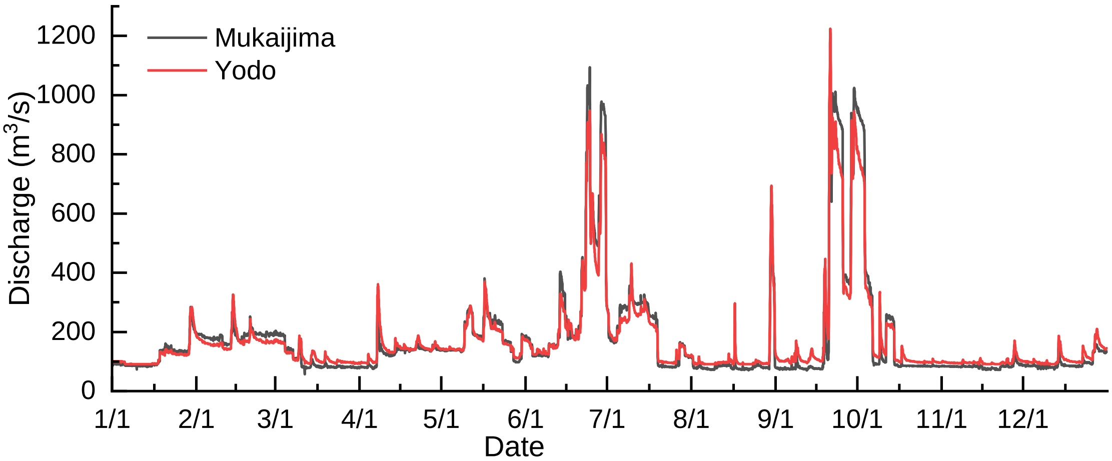

Figure 5.4 Observed hourly flowrates of Mukaijima station and Yodo station in 2016 (source: http://www1.river.go.jp/)

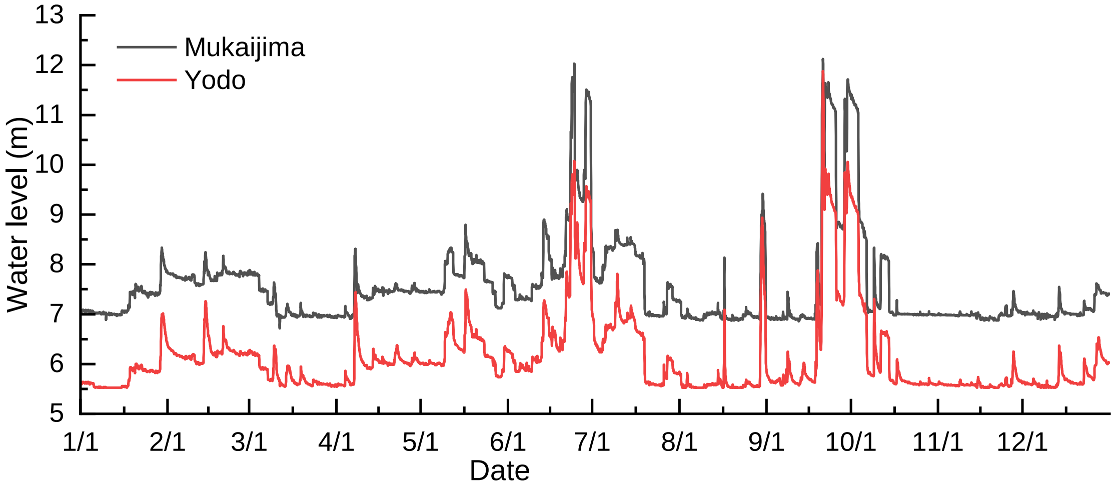

Figure 5.5 Observed hourly water levels of Mukaijima station and Yodo station in 2016 (source: http://www1.river.go.jp/)

Regarding the riverbed sediment size, as plotted in Figure 5.6, Karki (Karki, 2019) measured the grain size distribution of two sediment samples, one collected from a point bar near the confluence with the Yamashina River, the other collected from a point bar near the Ujigawa Open Laboratory (see Figure 5.3 for locations).

From these two sediment samples, we got two median grain diameters, 9.12 mm and 10.44 mm. The average value of the two diameters was used in subsequent simulations, that is, $d_{50} = 9.78$ mm.

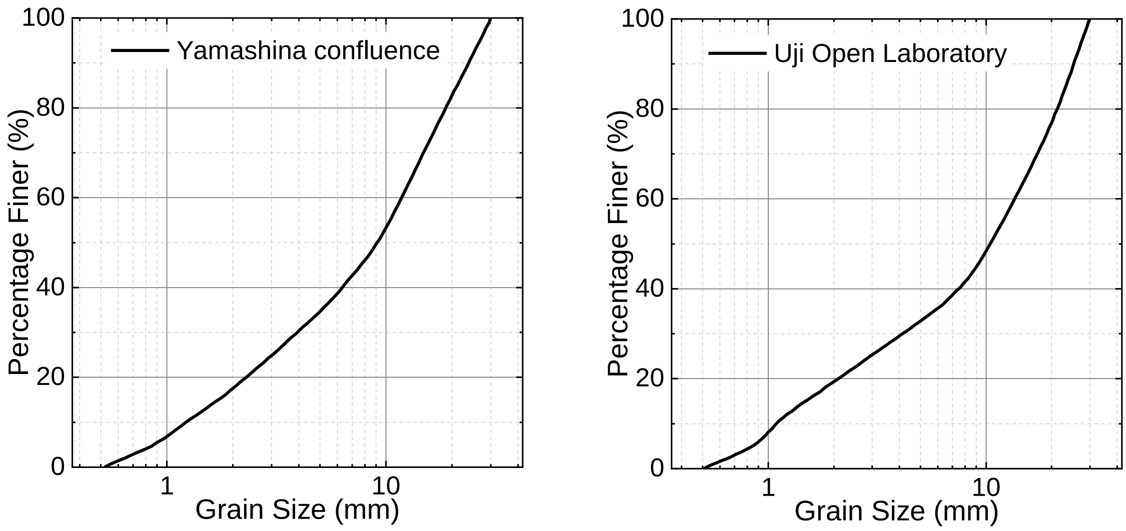

a) Sample near the confluence with Yamashina River b) Sample near Uji Open Laboratory

Figure 5.6 Riverbed sediment grain size distribution (source: (Karki, 2019))

5.3. Flood event reproduction

It is impractical to conduct long-term and large-scale 3D simulations of natural rivers on a yearly basis, due to the high computational cost. Fujita et al. (Fujita et al., 1983) conducted field observations on the bank erosion of CS43 in the Uji River to investigate the correlation between the erosion rate and the discharge and duration of flood events. They concluded that the magnitude and duration of the tractive force during flood stages were major factors controlling the receding rate of the riverbank. Therefore, in this study, a flood event from the year 2016 was selected to numerically investigate the bank erosion process.

5.3.1. Boundary conditions

As presented in Figure 5.4 and Figure 5.5, there were two major flood events in the year 2016, the first at the end of June and the second at the end of September. The first flood event from 19:00 on June 20 to 23:00 on July 3, which was closer to the topographical measurement, was chosen for reproduction. The hydrographs of inlet flow discharge (Mukaijima Observation Station) and outlet water level (Yodo Observation Station) were plotted in Figure 5.7. The simulation duration totaled 316 h, i.e., 1,137,600 s. This is a double-peak flood event, with peak discharges at Mukaijima Station being 1093.98 m^3/s (15:00, June 24) and 978.21 m^3/s (23:00, June 28), a maximum water level of 12.026 m (15:00, June 24). At Yodo Station, the peak discharges were 974.33 m^3/s (16:00, June 24) and 867.5 m^3/s (21:00, June 28), with a maximum water level of 10.077 m (16:00, June 24).

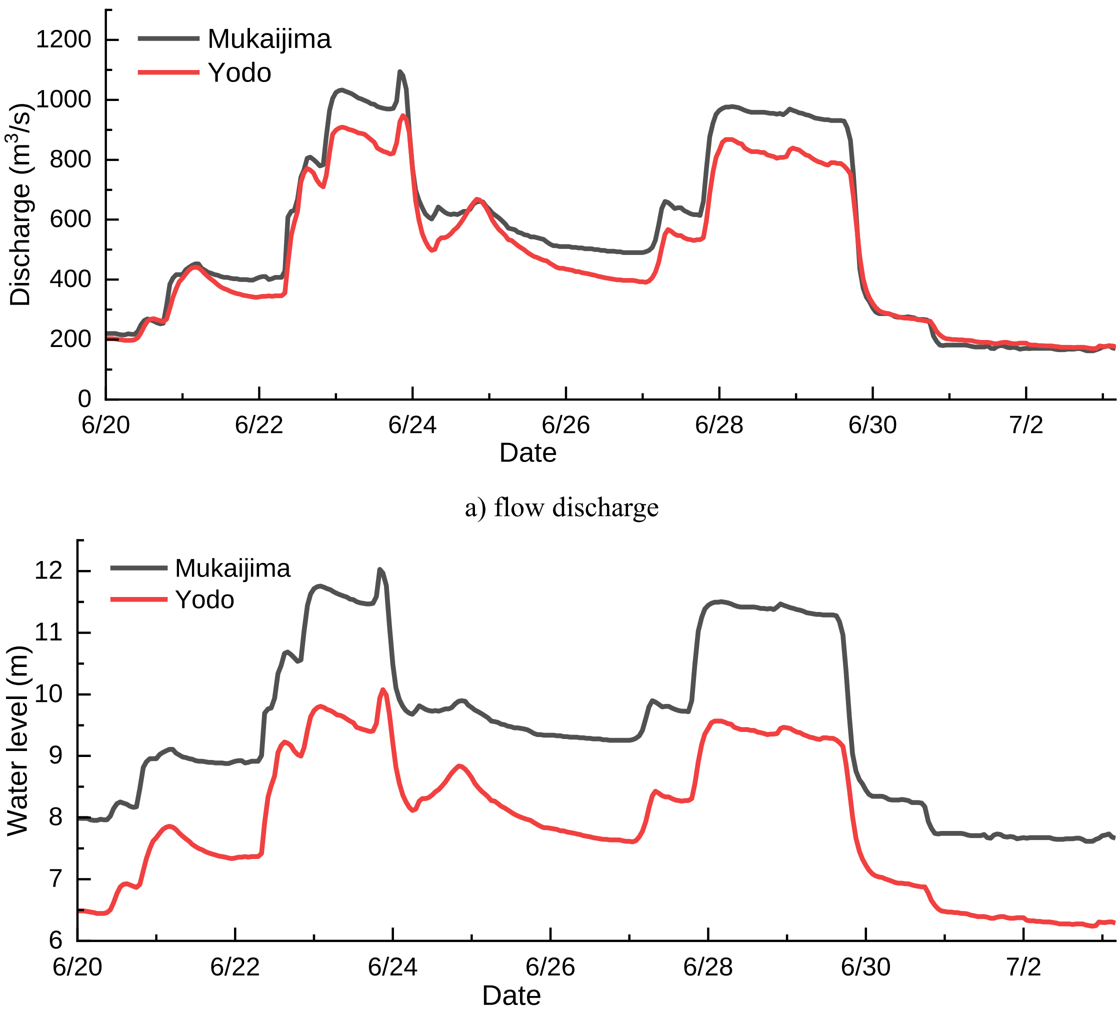

a) flow discharge

b) water level

Figure 5.7 Hydraulic boundary conditions

5.3.2. Mesh generation and mesh quality

In the simulations in this chapter, the semi-structured triangular prism mesh was still employed, generated by Gmsh which is an open-source 3D mesh generator. The vertical extent of the mesh was determined based on the topography and water level range. The topography was reflected through the porosity of each cell. To reduce the cell number and save computational cost, in the horizontal direction, the main channel had finer mesh, while the mesh size in the floodplain was larger, as presented in Figure 5.8. The mesh quality, which was the result of the checkMesh utility of OpenFOAM, is listed in Table 5.1.

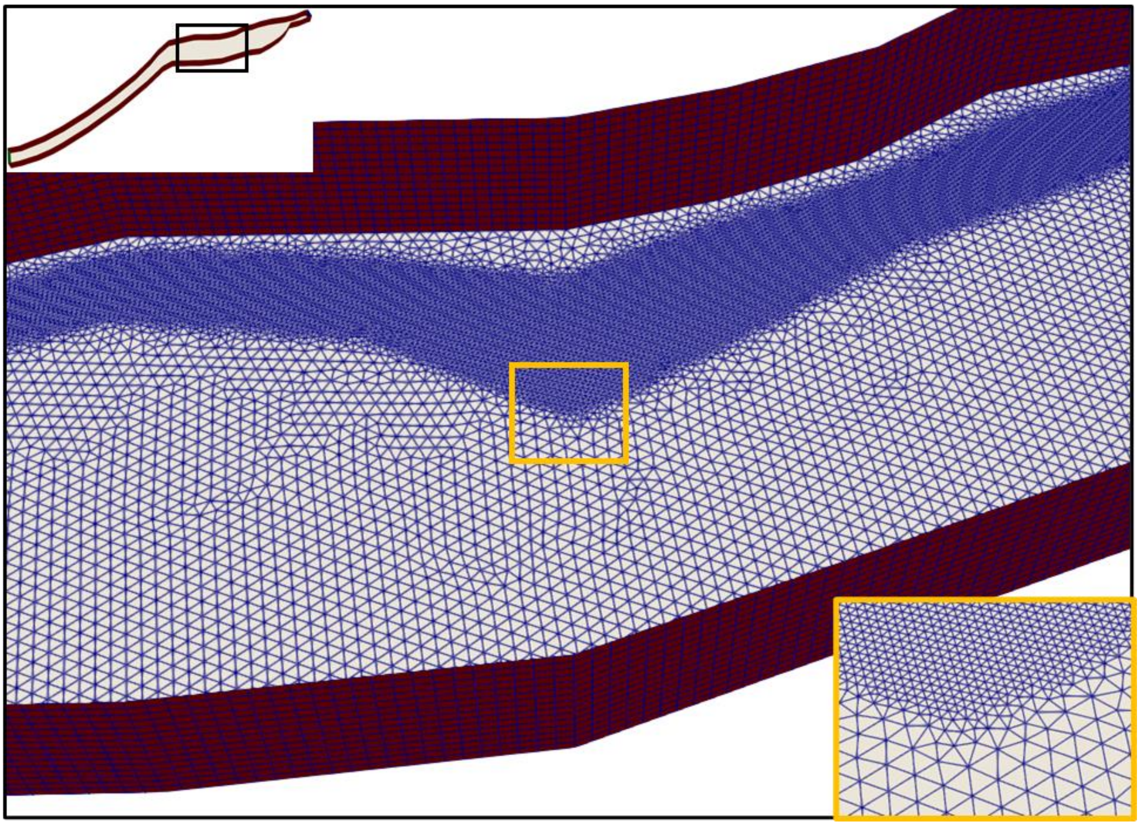

Figure 5.8 Semi-structured triangular prism mesh

Table 5.1 Mesh quality

Max. aspect ratio	Face area (m^2)		Cell volume (m^3)			Mesh non-orthogonality		Max skewness
	Min.	Max.	Min.	Max.	Total	Max.	Average	
9.77	3.26	142.12	5.59	142.12	3.10E+07	31.96	2.64	0.53

5.3.3. Results and discussions

(1) Water level

The simulated water level process and observed water level process at Mukaijima

Observation Station during the flood event are plotted in Figure 5.9. The simulated water level and observed water level exhibited synchronous variations, being nearly equal during low water levels. There was a slight overestimation during high water levels, but the highest water levels were very close. The R^2 value for water level was 0.92, and the mean absolute error was equivalent to 5.12% relative to the mean water depth at Mukaijima Observation Station.

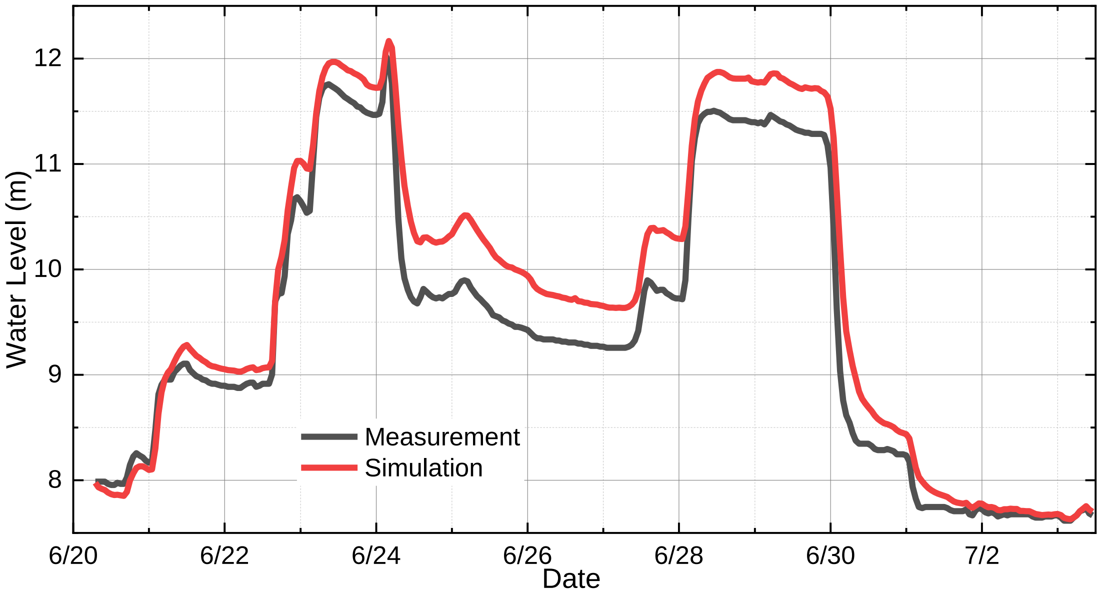

Figure 5.9 Simulated and observed water level at Mukaijima Observation Station

(2) Bed deformation and bank erosion

The initial bed topography and final bed topography at the end of the simulation for the bend in the vicinity of the CS43 are shown in Figure 5.10. The simulated bed deformation is presented in Figure 5.11.

As the bathymetry was interpolated from cross-sectional data, the initial topography appeared angular with many small grooves (Figure 5.10 (a)). In the straight channel portions upstream and downstream of the bend, erosion was mainly concentrated in the center of the main channel, while deposition occurred on its both sides (Figure 5.10 (b), Figure 5.11). This can be more clearly observed in the cross-section evolution of the CS434 (the section 43.4 km away from the river mouth) in Figure 5.12. At the CS43, erosion mainly occurred in the center of the main channel, while there was no fluvial erosion at the left bank toe. Downstream of CS43, affected by the bend, degradation was closer to the left outer bank.

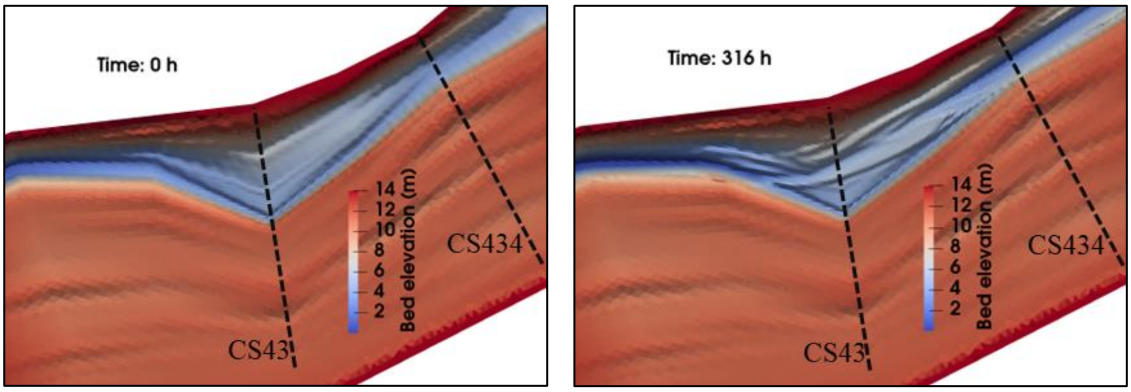

(a) Initial bed topography (a) Final bed topography

Figure 5.10 Simulated bed topography in the vicinity of CS43 (see Figure 5.2 for its location)

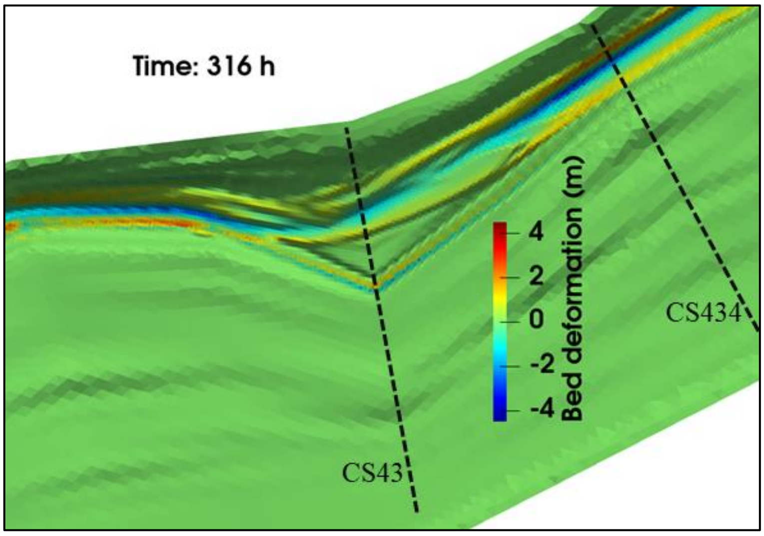

Figure 5.11 Simulated bed deformation in the vicinity of CS43 (see Figure 5.2 for its location)

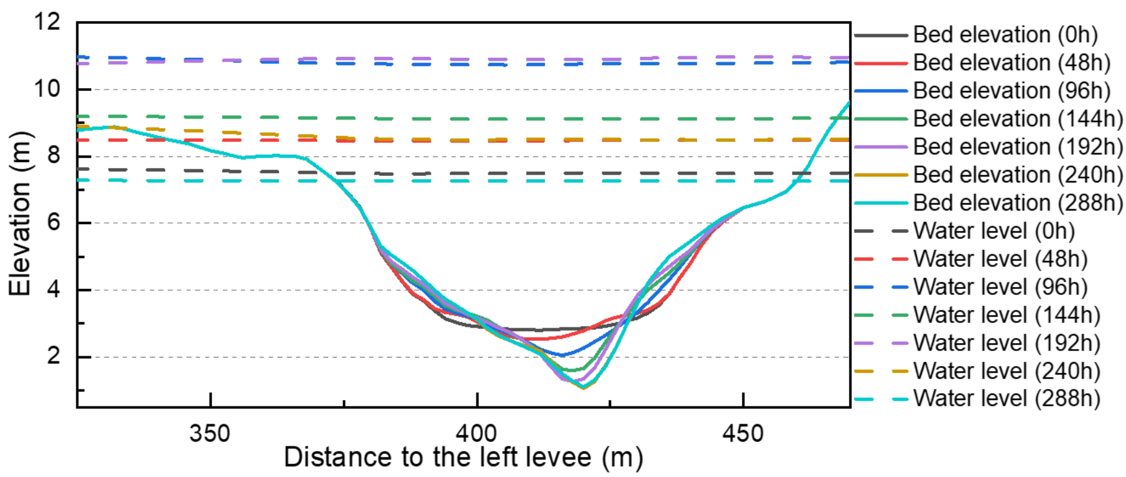

Figure 5.12 Cross-section evolution of CS434 (see Figure 5.2 for its location)

The cross-section evolution over time for section CS43 was plotted in Figure 5.13. The initial left bank was quite steep, and as the water level rose, the critical slope angle decreased, leading to bank mass failure, forming a stable left bank. The bank top retreated by approximately 4 m, which was relatively large compared to the average bank erosion rate of 4 m per year (Aly El-Dien, 2016; Karki, 2019). Afterward, due to erosion being concentrated in the center of the main channel and the absence of erosion at the toe of the left bank, the slope of the left bank remained unchanged and no further bank failure occurred.

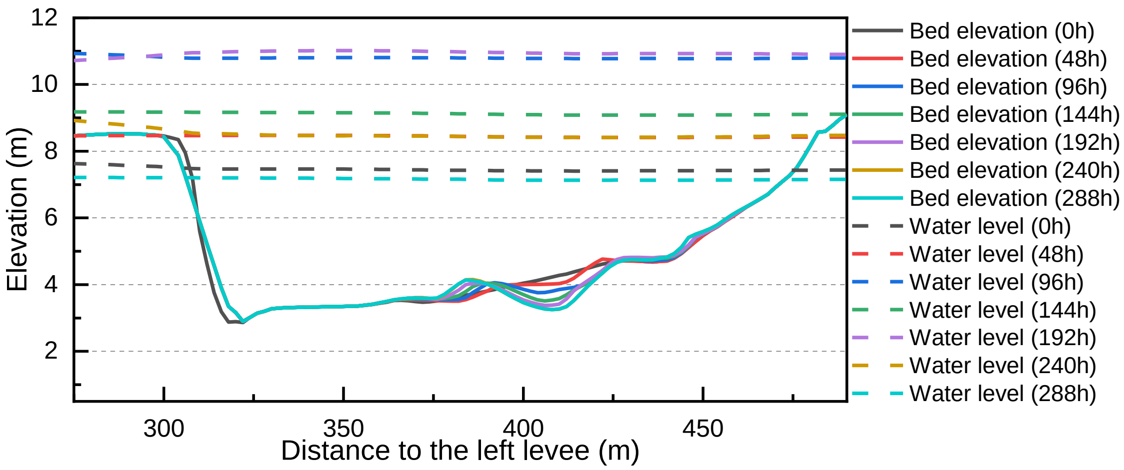

Figure 5.13 Cross-section evolution of CS43 (see Figure 5.2 for its location)

Overall, the model could simulate the bank failure of this reach to some extent, but there are some deficiencies in predicting the fluvial erosion in the main channel and bank toe, which is caused by various factors.

Firstly, the model did not consider non-uniform sediment, neglecting the effect of the particle size distribution and sediment sorting on the sediment transport. In the simulation, all sediment particle sizes were uniformly set to 9.78 mm. In reality, there is a significant difference in the sediment diameter between the bank and channel. Azuma et al. (Azuma et al., 2007) conducted a boring survey on the left bank and analyzed the composition of the sediment deposits. A well-sorted layer of sand and gravel with a diameter of 1 mm was observed near a depth of 1 m. Excluding this layer, silt layers with a particle size of 0.004 mm were deposited from the ground surface to a depth of 3 to 4 m. Below this, at a depth of 4 to 6 m, there was a layer of sand with a particle size of 0.3 mm. The sediment particle size on the left bank is notably smaller than 9.78 mm. In summary, overlooking the non-uniformity of sediment may result in an overestimation of the sediment transport rate in the channel center and an underestimation of the sediment transport rate at the bank toe.

Secondly, as mentioned in Chapter 2, the movement distance of a bed load parcel is restricted to three times the average step length. According to the equation in Chapter 2, when the dimensionless bed shear stress is infinitely large, the average step length reaches its maximum value of 1.467 m for this case. The actual average step length is much smaller than this value. Therefore, the maximum movement distance of a bed load parcel is much smaller than 4.365 m. Compared to the grid size of 5~15 m, this value is relatively small. This could potentially affect the bed load transport. Perhaps the applicability of the Lagrangian model in large-scale simulations needs further discussion and correction.

In addition, since the bathymetry was interpolated from the cross-sectional data with a 200 m interval, its accuracy may also have some impact on the simulation.

(3) Near-bed velocity and bed shear stress

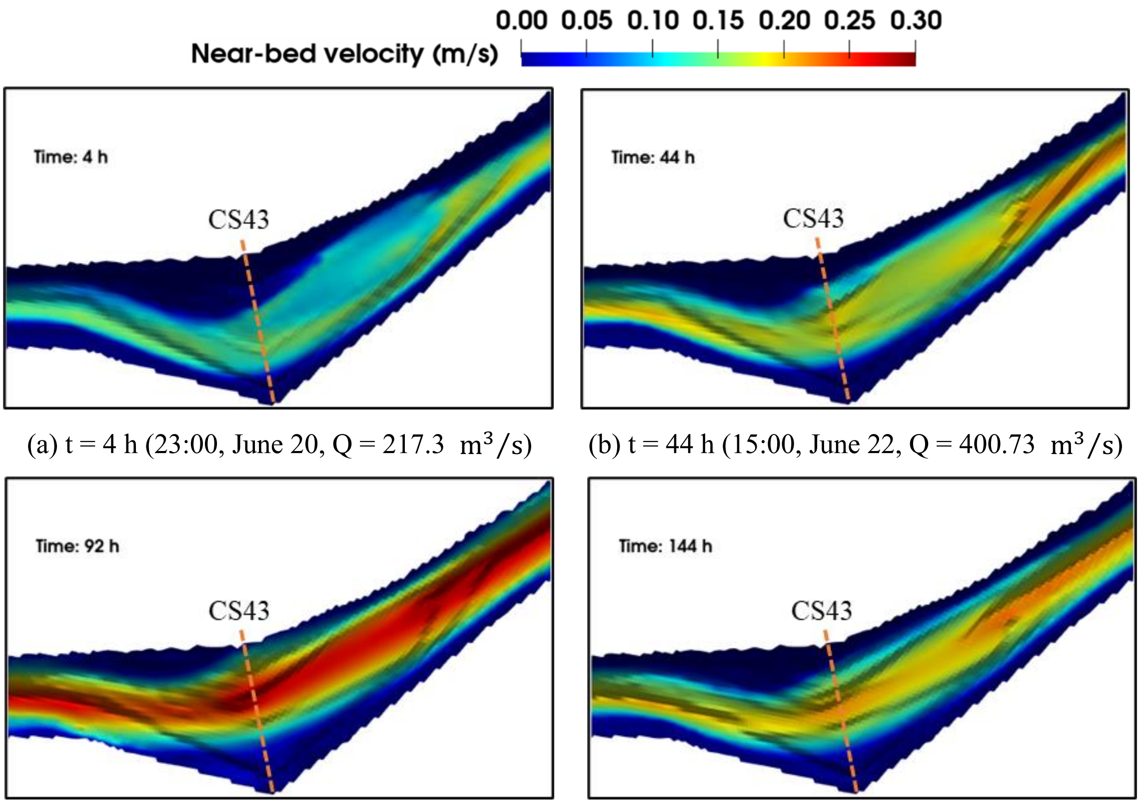

(a) t = 4 h (23:00, June 20, Q = 217.3 m^3/s) (b) t = 44 h (15:00, June 22, Q = 400.73 m^3/s)

(c) t = 92 h (15:00, June 24, Q = 1093.98 m^3/s) (d) t = 144 h (19:00, June 26, Q = 510.73 m^3/s)

Figure 5.14 Contours of near-bed velocity in the vicinity of CS43 (see Figure 5.2 for its location)

The contours of near-bed velocity near the CS43 in the main channel (bed elevation lower than 11 m) at four different stages are shown in Figure 5.14. The four stages were chosen according to the inflow discharge, including the early low flow (217.3 m^3/s), moderate flow before the peak (400.73 m^3/s), maximum peak flow (1093.98 m^3/s) and an intermediate flow (510.73 m^3/s) happened between the two peaks.

Upstream of the CS43, under small flow and low water level conditions, the main flow was closer to the left bank, making it more likely to carry away sediment from the bank toe (Figure 5.14. (a)). As the flow increased, the main flow began to shift towards the right bank, resulting in reduced flow velocity at the left bank toe, especially during peak flow (Figure 5.14. (b), (c), (d)). Conversely, downstream of this section, influenced by the bend, as the flow increased, the flow velocity increased at the left outer bank toe, posing a risk of severe erosion (Figure 5.14. (c)). Therefore, revetment has been implemented at this location against bank erosion (Figure 5.2).

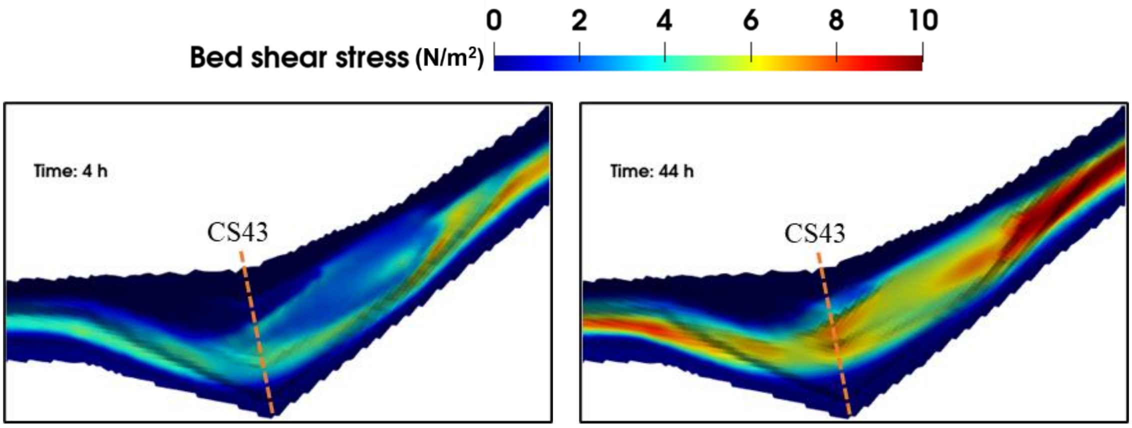

(a) t = 4 h (23:00, June 20, Q = 217.3 m^3/s) (b) t = 44 h (15:00, June 22, Q = 400.73 m^3/s)

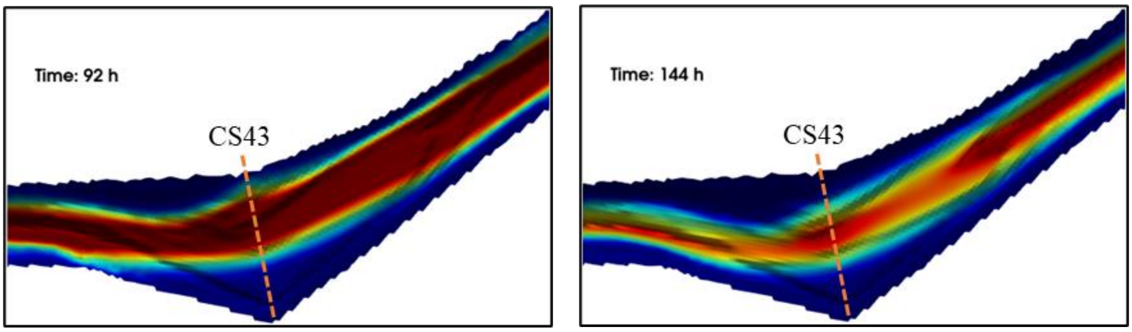

(c) t = 92 h (15:00, June 24, Q = 1093.98 m^3/s) (d) t = 144 h (19:00, June 26, Q = 510.73 m^3/s)

Figure 5.15 Contours of bed shear stress in the vicinity of CS43 (see Figure 5.2 for its location)

Similarly, the contours of bed shear stress at these four stages are presented in Figure 5.15. The variations of bed shear stress distribution with discharge were consistent with the temporal changes in near-bed velocity. Based on this, it could be inferred that the bank erosion process of this reach involves the erosion of the bank toe at a low flow stage, followed by collapse as the bank sediment strength decreases during or after the flood peak.

5.4. Simulations with spur dikes

5.4.1. Case setup

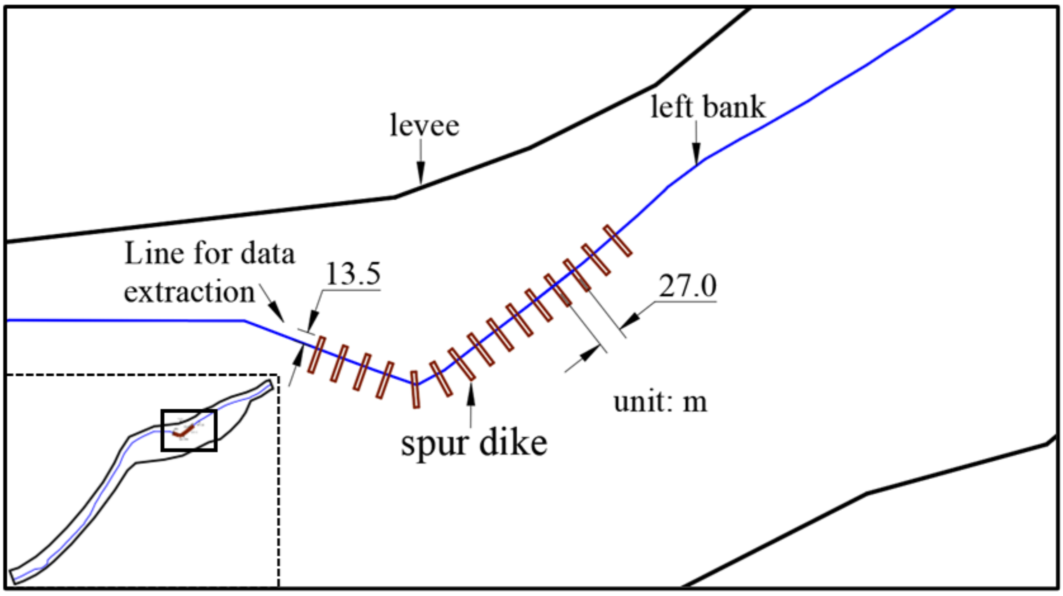

(a) spacing = 2*b* (27.0 m)

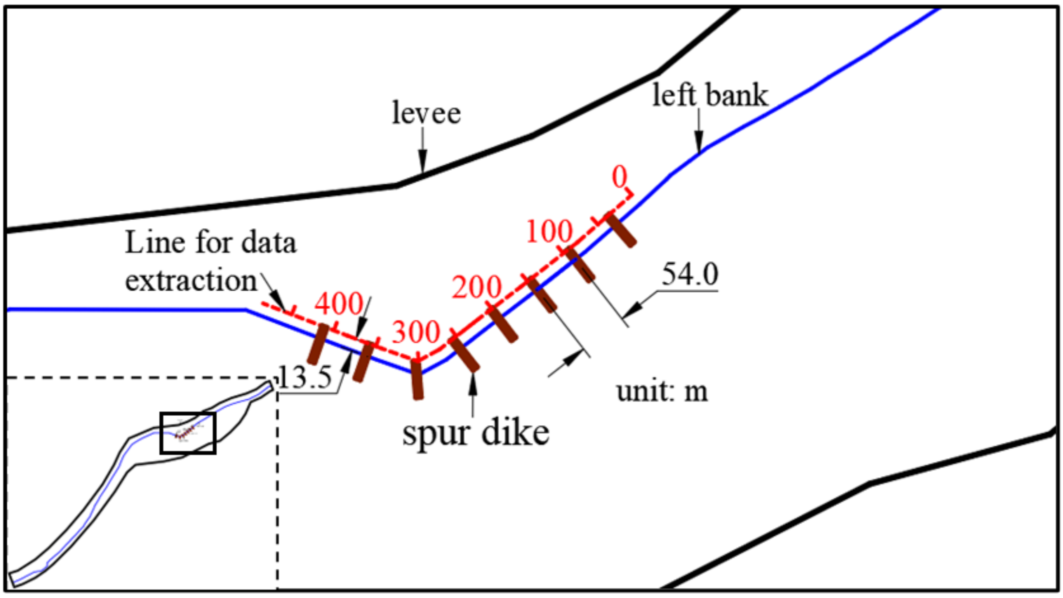

(b) spacing = 4*b* (54.0 m)

Figure 5.16 Arrangement of spur dikes
(*b* is the length of spur dike within main channel, 13.5 m)

In this section, we performed simulations with a series of spur dikes. As shown in Figure

5.2, starting from the point P, the left bank was severely eroded. Therefore, spur dikes were installed between point P and the revetment in simulations. As presented in Figure 5.16, two different spacings were considered. The average width of the main channel in this range was about 90.0 m, so the spur dike length b was set to 15% of the channel width, namely 13.5 m. Simulations were conducted for two cases with spacings of $2b$ (27.0 m) and $4b$ (54.0 m). The boundary conditions were the same as in the previous section.

5.4.2. Results and discussions

As mentioned earlier, due to the neglect of the sediment non-uniformity, the model did not capture bank toe erosion effectively. Therefore, this section focused solely on the flow field results at a lower flow stage (Q = 217.3 $\mathrm{m^3/s}$, 23:00, June 20), where the fluvial erosion is more likely to occur at the bank toe.

(1) Near-bed velocity

The contours of near-bed velocity in the main channel (bed elevation lower than 11 m) of the reach installed spur dikes at the moment of 4 h are shown in Figure 5.17 for both cases. The velocity distributions for the two spacing scenarios were quite similar. Compared to the result without spur dikes (Figure 5.14 (a)), upstream of the section CS43, the spur dikes effectively diverted the flow away from the left bank, reducing the velocity at the bank toe and providing protection against erosion. Consistent with the results in section 3.2, the several spur dikes closest to the CS43 (the apex of the bend) were far from the mainstream and seemed unnecessary.

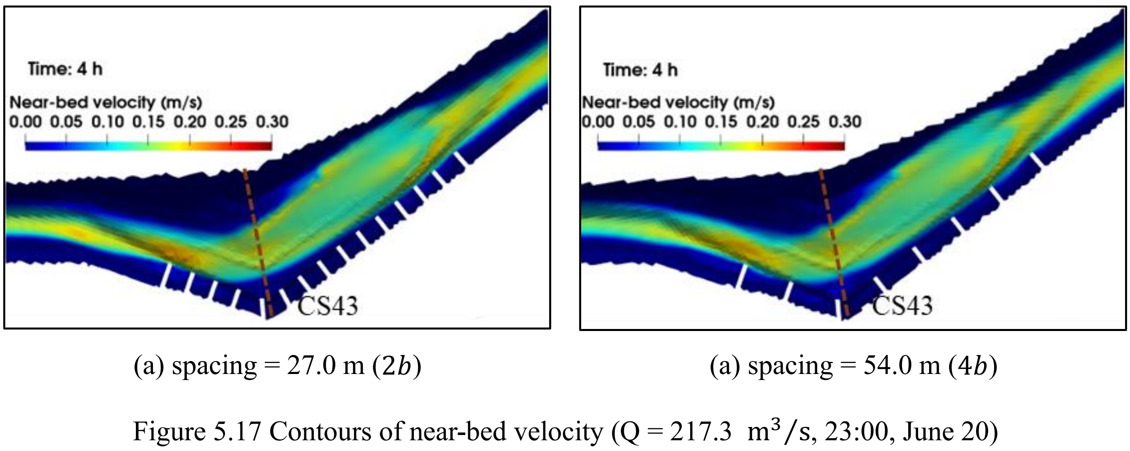

(a) spacing = 27.0 m ($2b$) (a) spacing = 54.0 m ($4b$)

Figure 5.17 Contours of near-bed velocity (Q = 217.3 $\mathrm{m^3/s}$, 23:00, June 20)

The near-bed velocity magnitude along spur tips (the line in Figure 5.16 (b)) was plotted in Figure 5.18. The longitudinal velocity variations for the $2b$ and $4b$ cases were very similar, with the main difference being that under the $2b$ spacing condition, the velocity fluctuations were larger than those under the $4b$ spacing condition. It was evident that the spur dikes with longitudinal distance between 150 m and 350 m had little effect and were not necessary. In the case with a spacing of $2b$, influenced by the bend, the velocity near the most downstream spur dike (longitudinal distance larger than 400 m) exceeded the velocity in the case without spur dikes. However, the revetment has been already constructed from here (Figure 5.2).

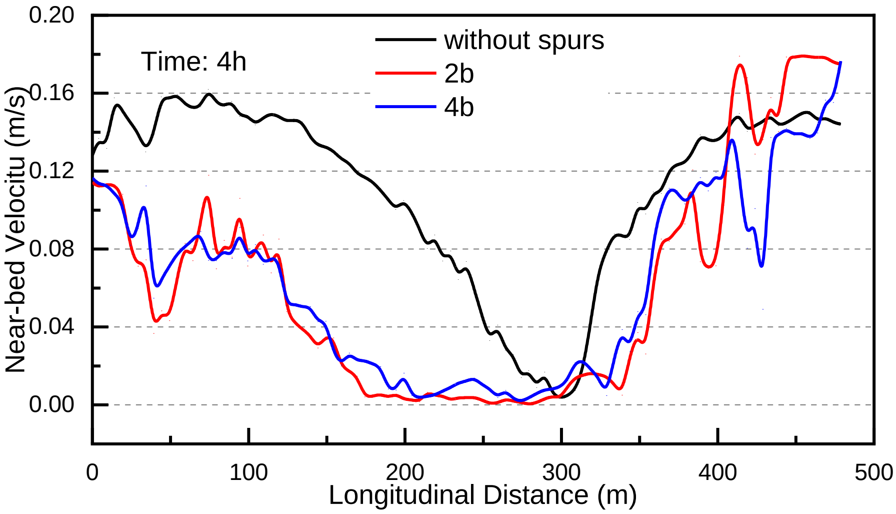

Figure 5.18 Longitudinal profiles of near-bed velocity magnitude along spur dike tips (along the line in Figure 5.16 (b))

(2) Aquatic habit assessment

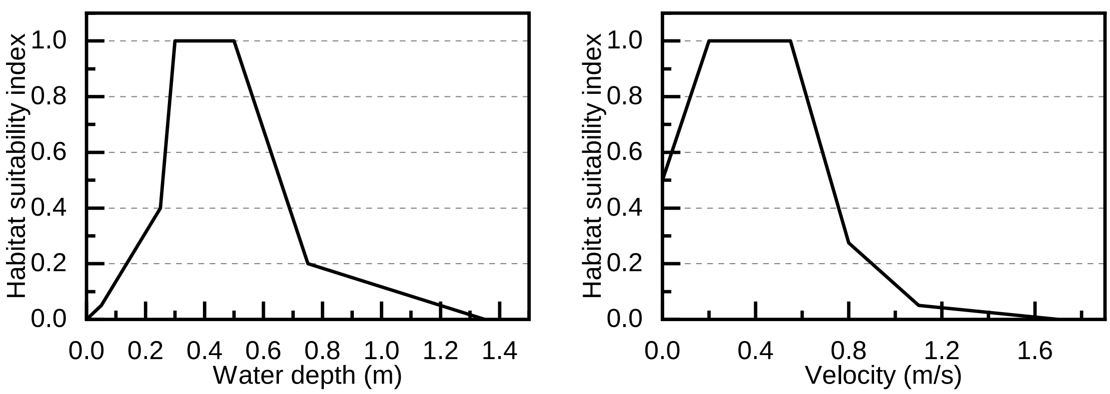

(a) For water depth

(b) For depth-averaged velocity

Figure 5.19 Habitat suitability index for Zacco platypus (source: (Jung and Choi, 2015))

The aquatic habit assessment was performed by using the Instream Flow Incremental Methodology (IFIM) (Stalnaker, 1995) to determine the relationship between stream flows and fish habitat. Ishida et al. Ishida et al. (Ishida et al., 2020) have conducted a habitat evaluation analysis in Uji River under the assumption that the reclaimed land of old Ogura Pond served as a retarding basin. They mentioned that the freshwater minnows, Zacco platypus, was the dominant species in the river basin. Therefore, Zacco platypus was chosen as the target fish in the aquatic habit evaluation. The habitat suitability curves for Zacco platypus (Figure 5.19) used by Jung and Choi (Jung and Choi, 2015) were employed to calculate the habitat suitability indices (HSIs) for the water depth and depth-averaged velocity.

The geometric average of the HSIs for water depth and velocity is taken as the composite suitability index (CSI) (Yang et al., 2023):

$$CSI_i = \sqrt{HSI_{h,i} \times HSI_{u,i}} \tag{5.1}$$

where, subscript i indicates the bed surface cell label; $HSI_{h,i}$, $HSI_{u,i}$ are the HSIs for the water depth and depth-averaged velocity, respectively. The potential value of aquatic habit was quantified by the weighted usable area (WUA):

$$WUA = \sum_{i=1}^{N}(A_i \times CSI_i) \tag{5.2}$$

where, N is the number of bed surface cells; A_i is the bed surface area of the bed surface cell i.

The WUA for the middle part of the study area at the moment of 4 h (Q = 217.3 $\mathrm{m^3/s}$, 23:00, June 20) were listed in Table 5.2. Compared to the natural condition, the area of fish habitat increased slightly after the installation of spur dikes. The WUA increased by 1.69% for the $2b$ spacing and 3.03% for the $4b$ spacing, with a larger increase for a greater spacing. However, on the whole, the installation of spur dikes in this reach has a minimal impact on the improvement of the living environment of Zacco platypus. In my opinion, this factor is not necessary to be considered when designing spur dikes in the study area.

Table 5.2 Weighted usable area (WUA) at the moment of 4 h (Q = 217.3 $\mathrm{m^3/s}$, 23:00, June 20)

	Without spurs	spacing = $2b$	spacing = $4b$
WUA ($\mathrm{m^2}$)	10088.80	10259.79	10394.44
Increase percentage compared to without spur dike	0	1.69%	3.03%

5.5. Summary

In this chapter, the solver considering bank erosion developed in Chapter 4 was applied to the simulations of the Uji River.

Firstly, a flood event in 2016 was reproduced. The comparison of simulated and observed water levels shows good agreement. As for bed deformation and bank erosion, the model could simulate the bank failure during rising water levels, while there are some deficiencies in predicting the fluvial erosion in the main channel and bank toe. Specifically, erosion was mainly concentrated in the center of the main channel, while deposition occurred on both sides. On the one hand, this may be attributed to neglecting the non-uniformity of sediment, leading to an underestimation of the particle size in the main channel, and an overestimation of the particle size in the bank. After all, the latter one is much smaller than the former one actually. On the other hand, it could be influenced by the average step length in the sediment transport model. The average step length by the equation current used in Chapter 2 is relatively small compared to the cell size for the large-scale simulations, limiting the sediment movement. Observing the near-bed velocity and bed shear stress distribution at different stages during the flood, it was found that as flowrate increased and water level rose, the main flow and high-stress areas tended to move away from the outer bank towards the center, upstream of the CS43. Based on this observation, it could be inferred that the bank erosion process of this reach involves the erosion of the bank toe under low flow conditions, followed by collapse as the bank sediment strength decreases during or after the flood peak.

Secondly, two cases with spacings of $2b$, $4b$, respectively, were simulated. Only the results at a low flow stage, where the bank toe was more likely to be eroded, were analyzed. The spur dikes effectively diverted the flow away from the outer bank, reducing the velocity at the bank toe and providing protection against erosion. Two spacings exhibited similar performance. The spur dikes in the vicinity of the apex (CS43) seemed unnecessary, with only the upstream spur dikes playing a role. Besides, the aquatic habitat evaluation for Zacco platypus was performed. The weighted usable area (WUA) increased slightly, by 1.69% for $2b$ and 3.03% for $4b$. In this reach, the impact of spur dikes on the aquatic habitat for Zacco platypus was minimal.

Chapter 6.
Conclusions and recommendations

6.1. Conclusions

The conclusions of this study are summarized as follows:

6.1.1. Model validation for meandering channel applications

Based on the applications in straight channels by Ota et al. (Ota et al., 2017), Ota and Sato (Ota and Sato, 2020) and Okudaira (Okudaira, 2021), the model was tested for flow field with a U-shaped channel experiment and for bed deformation based on a movable bed experiment in a meandering channel to validate its applicability to the investigation of flow and sediment transport around spur dikes in meandering channels for subsequent simulations. For the first one, the simulated water levels and velocity distribution along depth aligned well with the observed ones. For the second one, the numerical result has captured the bed deformation features observed in the experiment.

It can be concluded that the model can be used to analyze the flow and sediment transport around spur dikes in meandering channels.

6.1.2. The effect of the location of a single spur dike and channel sinuosity

A spur dike was sequentially placed at 6 different locations in 3 meandering channels with different sinuosity to analyze the effect of the location of a spur dike along the outer bank on the downstream separation zone length, bank protection extent, and local scour depth, as well as its relationship with the channel sinuosity. The downstream separation zone length and local scour depth depended on both the location of the spur dike and channel sinuosity. The bank protection extent was less than the corresponding downstream separation zone. The downstream separation zone length decreased as the spur dike moved downstream. Correspondingly, non-uniform spacing could be adopted to improve cost-effectiveness. Channels with larger sinuosity were more likely to have longer downstream separation zones. Local scour depth increased as the spur dike moved downstream and reached the maximum near the crossover point, where measures might need to be taken to mitigate the local scour. Upstream of this location, channels with greater sinuosity exhibited more severe local scour, whereas the opposite trend was observed downstream.

6.1.3. The effect of the spacing of a series of spur dikes and channel sinuosity

A series of spur dikes with 5 kinds of spacings were installed in 2 meandering channels to investigate the influence of both spur dike spacing and channel sinuosity. Unlike straight channels where maximum scour depth is located near the first spur dike, in meandering channels, serious local scour occurs near both the most upstream spur dike and spur dikes downstream of the meander apex. Therefore, both of these locations should be given special attention to control local scour in practices. Since the deep local scour holes and large velocity fluctuations occurred at different locations with varying spacing, non-uniform spacing should be adopted to lower the construction cost. Different channel sinuosities required different spacing arrangements because the locations of deep local scour holes and large velocity fluctuations were affected by sinuosity.

Based on the simulation results, an equation using the weighted sum approach for multiobjective programming problems was proposed to quantify their performance by comprehensively considering four factors of bank protection, structural stability, construction cost, and aquatic habitat. In current uniform spacing simulations, $2b$ was the optimum spacing for Ch45 and $4b$ was the best for Ch60.

6.1.4. Model validation for bank erosion

An OpenFOAM solver considering bank erosion was developed by incorporating a bank mass failure operator into the 3D numerical model introduced in Chapter 2. The bank mass failure operator compares the local slope angle of each bed surface cell with the submerged critical angle or emerged critical angle depending on the water depth to determine the stability of this cell and then simulates the collapse by rotating unstable cells. This method can eliminate the necessity to explicitly identify the location of the riverbank, greatly enhancing its convenience. The model performance was tested using three experiments: a straight channel dam break experiment, a meandering channel experiment without spur dikes, and a meandering channel experiment with spur dikes. For the first one, the error of cross-section profiles was acceptable, and both the cross-section profile evolution and final profiles were reproduced in a reasonable manner. For the second one, the simulated bankline shifting had good agreement with the observations and the final cross-section profiles were simulated in a reasonable manner. For the last one, the bank retreat in the area installed spur dikes and the local scour around spur dike tips satisfactorily matched the measurements.

It can be concluded that the model can be employed to evaluate the performance of spur dikes against bank erosion and to investigate the temporal changes of plan form in a meandering channel.

6.1.5. Field application in Uji River

The new solver was applied to the simulations of the Uji River. A flood event in 2016 was reproduced. The comparison of simulated and observed water levels shows good agreement. As for bed deformation and bank erosion, the model could simulate the bank failure during rising water levels, while there are some deficiencies in predicting the fluvial erosion in the main channel and bank toe. Specifically, erosion was mainly concentrated in the center of the main channel, while deposition occurred on both sides. Observing the near-bed velocity and bed shear stress distribution at different stages during the flood, it was found that as the flowrate increased and the water level rose, the main flow and high-stress areas tended to move away from the outer bank towards the center. Based on this observation, it could be inferred that the bank erosion process of this reach involves erosion of the bank toe at lower flow, followed by collapse occurring when the sediment strength of the bank decreases during or after the flood peak.

Two cases with spacings of $2b$, $4b$, respectively, were simulated. Only the results in a lower flow stage, where the bank toe was more likely to be eroded, were analyzed. The spur dikes effectively diverted the flow away from the outer bank, reducing the velocity at the bank toe and providing protection against erosion. Two spacings exhibited similar performance. The spur dikes in the vicinity of the apex (CS43) seemed unnecessary, with only the upstream spur dikes playing a role. Besides, the aquatic habitat evaluation for Zacco platypus was performed. The weighted usable area (WUA) increased slightly, by 1.69% for $2b$ and 3.03% for $4b$. In this reach, the impact of spur dikes on the aquatic habitat for Zacco platypus was minimal.

6.2. Recommendation for future studies

The current numerical study still has several limitations and a summary of issues for improvement and consideration in future research is provided below:

(1) The simulations for meandering channels in Chapter 3 were based on laboratory conditions, having channel width-to-depth (B/h) ratio many times smaller than that of an

extensively meandering river, which could lead to the exaggeration of the effect of secondary currents in meanders. The performance of spur dikes in channels with different B/h ratios needs to be investigated.

(2) The current model did not consider non-uniform sediment and neglected the effect of particle size distribution and sediment sorting on sediment transport. For instance, in Uji River, the particle size in the bank is much smaller than that in the main channel. overlooking the non-uniformity of sediment will result in an overestimation of the sediment transport rate in the channel center and an underestimation of the sediment transport rate at the bank toe.

(3) The logarithmic law of velocity distribution was employed to compute the bed shear stress for bed load transport. Its applicability to regions near spur dikes may need to be further investigated.

(4) The calculation method of average step length in the sediment transport model should be improved. As mentioned in Chapter 2, the movement distance of a bed load parcel is restricted to three times the average step length. In the filed application in Chapter 5, according to the equation in Chapter 2, when the dimensionless bed shear stress is infinitely large, the average step length reaches its maximum value of 1.467 m for the Uji River. The actual average step length is much smaller than this value. Therefore, the maximum movement distance of a bed load parcel is much smaller than 4.365 m. Compared to the cell size of 5 to 15 m, this value is relatively small. This could limit the bed load movement.

(5) The current bank mass failure operator was limited to non-cohesive sediment. Only water depth was considered when determining the critical stability slope angle, and factors such as groundwater table, pore water pressure, sediment properties, and sediment strength variations were not taken into account. These factors can be considered in future research to improve the model.

(6) Vegetation on the river banks affects not only the flow structure but also the strength of banks and can be considered in the future.

(7) The current study focused on impermeable spur dikes under non-submerged conditions. However, impermeable spur dikes could become submerged at high flood levels, and the overtopping flow may result in serious erosion. Therefore, the submergence should be taken into account in spur dike design.

References

Abadi, A.M.N., Bateni, M.M., 2017. Experimental investigation of flow pattern around repelling and attracting T-head spur dikes on flat bed. J. Fundam and Appl Sci. 9 3 , 1644. doi:10.4314/jfas.v9i3.25

Abderrezzak, K.E.K., Moran, A.D., Tassi, P., Ata, R., Hervouet, J.-M., 2016. Modelling river bank erosion using a 2D depth-averaged numerical model of flow and non-cohesive, non-uniform sediment transport. Advances in Water Resources, Numerical modelling of river morphodynamics 93, 75–88. doi:10.1016/j.advwatres.2015.11.004

Alauddin, M., Hossain, M.M., Uddin, M.N., Haque, M.E., 2017. A Review on Hydraulic and Morphological Characteristics in River Channels Due to Spurs. International Journal of Geological and Environmental Engineering 11 4 , 397–404.

Aly El-Dien, A., 2016. Modelling the Hydraulic Erosion and Failure Processes of Cohesive Riverbanks (PhD Thesis). Kyoto University.

Asawa, G.L., 2006. Irrigation and water resources engineering. New age international.

Azuma, R., Sekiguchi, H., 2008. Geomorphological Evolution and Sediment Budget Analysis with the Uji River, Kyoto.

Azuma, R., Sekiguchi, H., Ono, T., 2007. Studies of High-resolution Morphodynamics with Special Reference to River Bank Erosion. DPRI Annuals 50 C , 199–209.

Baird, D.C., Fotherby, L., Klumpp, C.C., Sculock, S.M., 2015. Bank Stabilization Design Guidelines (No. SRH-2015-25).

Basser, H., Karami, H., Shamshirband, S., Akib, S., Amirmojahedi, M., Ahmad, R., Jahangirzadeh, A., Javidnia, H., 2015. Hybrid ANFIS–PSO approach for predicting optimum parameters of a protective spur dike. Applied Soft Computing 30, 642–649. doi:10.1016/j.asoc.2015.02.011

Brackbill, J.U., Kothe, D.B., Zemach, C., 1992. A continuum method for modeling surface tension. Journal of computational physics 100 2 , 335–354.

Brown, S.A., 1984. Design Guidelines for Spur-Type Flow-Control Structures. Transportation Research Record 950 2 , 193–201.

Burcharth, H.F., Andersen, O.K., 1995. On the one-dimensional steady and unsteady porous flow equations. Coastal engineering 24 3–4 , 233–257.

Burele, S.A., Gupta, I.D., Singh, M., Sharma, N., Ahmad, Z., 2012. Experimental study on performance of spurs. ISH Journal of Hydraulic Engineering 18 3 , 152–161.

Cao, X., Gu, Z., Tang, H., 2013. Study on Spacing Threshold of Nonsubmerged Spur Dikes with Alternate Layout. Journal of Applied Mathematics 2013, 945984. doi:10.1155/2013/945984

da Silva, A.M.F., El-Tahawy, T., 2008. On the location in flow plan of erosion–deposition zones in sine–generated meandering streams. Journal of Hydraulic Research 46 sup1 , 49–60. doi:10.1080/00221686.2008.9521939

da Silva, A.M.F., Yalin, M.S., 2017. Fluvial Processes, 2nd ed. CRC Press, London. doi:10.4324/9781315206189

Damian, S.M., 2012. Description and utilization of interFoam multiphase solver (Technical report). International Center for Computational Methods in Engineering.

de Vriend, H.J., 1979. Flow measurements in a curved rectangular channel (No. 9–79). TU Delft, Department of Hydraulic Engineering.

del Jesus, M., Lara, J.L., Losada, I.J., 2012. Three-dimensional interaction of waves and porous coastal structures: Part I: Numerical model formulation. Coastal Engineering 64, 57–72. doi:10.1016/j.coastaleng.2012.01.008

Duan, J.G., 2009. Mean Flow and Turbulence around a Laboratory Spur Dike. Journal of Hydraulic Engineering 135 10 , 803–811. doi:10.1061/(ASCE)HY.1943-

7900.0000077
Duan, J.G., He, L., Fu, X., Wang, Q., 2009. Mean flow and turbulence around experimental spur dike. Advances in Water Resources 32 12 , 1717–1725. doi:10.1016/j.advwatres.2009.09.004
Duan, J.G., Nanda, S.K., 2006. Two-dimensional depth-averaged model simulation of suspended sediment concentration distribution in a groyne field. Journal of Hydrology 327 3–4 , 426–437. doi:10.1016/j.jhydrol.2005.11.055
Egorov, Y., Menter, F., 2008. Development and application of SST-SAS turbulence model in the DESIDER project, in: Advances in Hybrid RANS-LES Modelling. Springer, pp. 261–270.
Ehrgott, M., Wiecek, M.M., 2005. Mutiobjective Programming, in: Figueira, J., Greco, S., Ehrogott, M. (Eds.), Multiple Criteria Decision Analysis: State of the Art Surveys, International Series in Operations Research & Management Science. Springer, New York, NY, pp. 667–708. doi:10.1007/0-387-23081-5_17
Elawady, E., Hinokidani, O., 2000. Study of flow behavior submerged spur-dike on rigid bed 6.
Elhakeem, M., Papanicolaou, A.N., Wilson, C.G., 2017. Implementing streambank erosion control measures in meandering streams: design procedure enhanced with numerical modelling. International Journal of River Basin Management 15 3 , 317–327.
Ettema, R., Muste, M., 2004. Scale effects in flume experiments on flow around a spur dike in flatbed channel. Journal of Hydraulic Engineering 130 7 , 635–646.
Evangelista, S., Greco, M., Iervolino, M., Leopardi, A., Vacca, A., 2015. A new algorithm for bank-failure mechanisms in 2D morphodynamic models with unstructured grids. International Journal of Sediment Research 30 4 , 382–391. doi:10.1016/j.ijsrc.2014.11.003
Fazli, M., Ghodsian, M., Neyshabouri, S.A.A.S., 2008. Scour and flow field around a spur dike in a 90° bend. International Journal of Sediment Research 23 1 , 56–68. doi:10.1016/S1001-6279(08)60005-0
Florsheim, J.L., Mount, J.F., Chin, A., 2008. Bank Erosion as a Desirable Attribute of Rivers. BioScience 58 6 , 519–529. doi:10.1641/B580608
Fujita, Y., Muramoto, Y., Miyasaka, H., 1983. Side bank erosion in rivers. DPRI Annuals 26 B-2 , 427–444.
Garcia, M., Parker, G., 1991. Entrainment of bed sediment into suspension. Journal of Hydraulic Engineering 117 4 , 414–435.
Giglou, A.N., Mccorquodale, J.A., Solari, L., 2017. Numerical study on the effect of the spur dikes on sedimentation pattern. Ain Shams Engineering Journal 9 4 , 2057–2066. doi:10.1016/j.asej.2017.02.007
Giri, S., Shimizu, Y., 2004. Observation on Bed Variation in a Meandering Like Flume with River Training Structures. Annual Journal of Hydraulic Engineering, JSCE 48, 1069–1074. doi:10.2208/prohe.48.1069
Giri, S., Shimizu, Y., Fujita, M., 2003. Flow characteristics in a mildly meandering channel with & without river training structures. Annual Journal of Hydraulic Engineering, JSCE 47, 835–840. doi:10.2208/prohe.47.835
Giri, S., Shimizu, Y., Surajate, B., 2004. Laboratory measurement and numerical simulation of flow and turbulence in a meandering-like flume with spurs. Flow Measurement and Instrumentation 15 5–6 , 301–309. doi:10.1016/j.flowmeasinst.2004.05.002
Greenshields, C., 2020. OpenFOAM v8 User Guide. The OpenFOAM Foundation, London, UK.
Greenshields, C., Weller, H., 2022. Notes on computational fluid dynamics: General principles. CFD Direct Ltd, Reading, UK.
Gu, Z., Cao, X., Gu, Q., Lu, W.-Z., 2020. Exploring Proper Spacing Threshold of Non-Submerged Spur Dikes with Ipsilateral Layout. Water 12 1 , 172. doi:10.3390/w12010172
Han, X., Lin, P., 2018. 3D numerical study of the flow properties in a double-spur dikes field during a flood process. Water 10 11 , 1574.

Han, X., Lin, P., Parker, G., 2022. Numerical modelling of local scour around a spur dike with porous media method. Journal of Hydraulic Research 60 6 , 970–995. doi:10.1080/00221686.2022.2106589

Higuera, P., 2015. Application of computational fluid dynamics to wave action on structures (Ph.D. Thesis). University of Cantabria, Spain.

Hirt, C.W., Nichols, B.D., 1981. Volume of fluid (VOF) method for the dynamics of free boundaries. Journal of Computational Physics 39 1 , 201–225. doi:10.1016/0021-9991(81)90145-5

Hsu, T.-J., Sakakiyama, T., Liu, P.L.-F., 2002. A numerical model for wave motions and turbulence flows in front of a composite breakwater. Coastal Engineering 46 1 , 25–50. doi:10.1016/S0378-3839(02)00045-5

Ishida, Y., Okunishi, K., Harada, M., Ogawa, Y., Maegawa, M., 2020. Flood Control Effect and Habitat Creation in the Middle Basin of the Yodo River Using a Retarding Basin, in: Proceedings of the 22nd IAHR-APD Congress 2020, Sapporo, Japan.

Issa, R.I., 1986. Solution of the implicitly discretised fluid flow equations by operator-splitting. Journal of Computational Physics 62 1 , 40–65. doi:10.1016/0021-9991(86)90099-9

Jasak, H., 1996. Error analysis and estimation for the finite volume method with applications to fluid flows. Imperial College London (University of London).

Jowett, I.G., 1993. A method for objectively identifying pool, run, and riffle habitats from physical measurements. New Zealand Journal of Marine and Freshwater Research 27 2 , 241–248. doi:10.1080/00288330.1993.9516563

Jung, S.H., Choi, S.-U., 2015. Prediction of composite suitability index for physical habitat simulations using the ANFIS method. Applied Soft Computing 34, 502–512. doi:10.1016/j.asoc.2015.05.028

Kafle, M.R., 2021. The Numerical Simulation of Meandering Effects on Velocity Field and Separation Zone past a Spur Dike in Rigid Bed. Nepal Journal of Civil Engineering, meandering 2D 1 1 , 33–40.

Karami, H., Ardeshir, A., Saneie, M., Behzadian, K., Jalilsani, F., 2008. Reduction of Local Scouring with Protective Spur Dike, in: World Environmental and Water Resources Congress 2008. Presented at the World Environmental and Water Resources Congress 2008, American Society of Civil Engineers, Honolulu, Hawaii, United States, pp. 1–9. doi:10.1061/40976(316)255

Karami, H., Ardeshir, A., Saneie, M., Salamatian, S.A., 2012. Prediction of time variation of scour depth around spur dikes using neural networks. Journal of Hydroinformatics 14 1 , 180–191. doi:10.2166/hydro.2011.106

Karami, H., Basser, H., Ardeshir, A., Hosseini, S.H., 2014. Verification of numerical study of scour around spur dikes using experimental data. Water Environ J 28 1 , 124–134. doi:10.1111/wej.12019

Karki, S., 2019. Study on Hydro-morphological Characteristics of Meandering Channels with Groynes (PhD Thesis). Kyoto University, Kyoto.

Katopodes, N.D., 2019. Volume of Fluid Method, in: Free-Surface Flow. Elsevier, pp. 766–802. doi:10.1016/B978-0-12-815485-4.00018-8

Kuang, C., Zheng, Y., Gu, J., Zou, Q., Han, X., 2021. Experimental Study on Backflow Patterns Induced by a Bilateral Groin Pair with Different Spacing. Applied Sciences 11 4 , 1486. doi:10.3390/app11041486

Kuhnle, R.A., Alonso, C.V., Shields, F.D., 2002. Local Scour Associated with Angled Spur Dikes. J. Hydraul. Eng. 128 12 , 1087–1093. doi:10.1061/(ASCE)0733-9429(2002)128:12(1087)

Lagasse, P.F., Clopper, P.E., Pagán-Ortiz, J.E., Zevenbergen, L.W., Arneson, L.A., Schall, J.D., Girard, L.G., 2009. Bridge Scour and Stream Instability Countermeasures: Experience, Selection, and Design Guidance: Volume 2. National Highway Institute (US).

Lai, Y., 2017. Modeling Stream Bank Erosion: Practical Stream Results and Future Needs. Water 9 12 , 950. doi:10.3390/w9120950

Langbein, W.B., Leopold, L.B., 1966. River Meanders- Theory of Minimum Variance 19.

Leopold, L.B., Langbein, W.B., 1966. River Meanders. Sci Am 214 6 , 60–70. doi:10.1038/scientificamerican0666-60

Lesser, G.R., Roelvink, J.A., van Kester, J.A.T.M., Stelling, G.S., 2004. Development and validation of a three-dimensional morphological model. Coastal Engineering, Coastal Morphodynamic Modeling 51 8 , 883–915. doi:10.1016/j.coastaleng.2004.07.014

Liu, P.L.F., Lin, P., Chang, K.-A., Sakakiyama, T., 1999. Numerical Modeling of Wave Interaction with Porous Structures. Journal of Waterway, Port, Coastal, and Ocean Engineering 125 6 , 322–330. doi:10.1061/(ASCE)0733-950X(1999)125:6(322)

Ma, B., Dong, F., Peng, W.Q., Liu, X.B., Huang, A.P., Zhang, X.H., Liu, J.Z., 2020. Evaluation of impact of spur dike designs on enhancement of aquatic habitats in urban streams using 2D habitat numerical simulations. Global Ecology and Conservation 24, e01288. doi:10.1016/j.gecco.2020.e01288

Ma, Z., 2004. Modern Handbook of Applied Mathematics: Operations Research and Optimization Theory Volume, Modern Handbook of Applied Mathematics. Tsinghua University Press.

Mansoori, A.R., 2014. Study on Flow and Sediment Transport around Series of Spur Dikes with Different Head Shape (PhD Thesis). Kyoto University.

Masjedi, A., Akbari, I., Abyar, H., 2011. Evaluating scour at L-shape spur dike in a 180 degree bend. World Applied Sciences Journal 15 12 , 1740–1745.

Mecklenburg, D.E., Jayakaran, A.D., 2012. Dimensioning the Sine-Generated Curve Meander Geometry 1. JAWRA Journal of the American Water Resources Association 48 3 , 635–642.

Menéndez, A., Laciana, C., Garcia, P., 2008. An Integrated Hydrodynamic-Sedimentologic-Morphologic Model for the Evolution of Alluvial Channels Cross-Sections. Engineering Applications of Computational Fluid Mechanics 2, 411–426. doi:10.1080/19942060.2008.11015241

Menter, F., Egorov, Y., 2005. A scale-adaptive simulation model using two-equation models. Presented at the 43rd AIAA Aerospace Sciences Meeting and Exhibit, Reno, Nevada, p. 1095.

Menter, F.R., 2009. Review of the shear-stress transport turbulence model experience from an industrial perspective. International Journal of Computational Fluid Dynamics 23 4 , 305–316. doi:10.1080/10618560902773387

Menter, F.R., 1994. Two-equation eddy-viscosity turbulence models for engineering applications. AIAA Journal 32 8 , 1598–1605. doi:10.2514/3.12149

Menter, F.R., 1992. Improved two-equation k-omega turbulence models for aerodynamic flows.

Menter, F.R., Esch, T., 2001. Elements of Industrial Heat Transfer Predictions, in: 16th Brazilian Congress of Mechanical Engineering (COBEM), Uberlandia, Brazil, 2001.

Mizutani H., 2011. Study on Local Scour and Variation of Bed Composition Around Submerged and Non-Submerged Spur Dyke (PhD Thesis). Kyoto University, Kyoto, Japan.

Mizutani, N., McDougal, W.G., Mostafa, A.M., 1996. BEM-FEM Combined Analysis of Nonlinear Interaction Between Wave and Submerged Breakwater, in: Coastal Engineering 1996. Presented at the 25th International Conference on Coastal Engineering, American Society of Civil Engineers, Orlando, Florida, United States, pp. 2377–2390. doi:10.1061/9780784402429.184

Mooney, K., Maric, T., Höpken, J., 2014. The OpenFOAM Technology Primer. doi:10.13140/2.1.2532.9600

Mosselman, E., 2020. Studies on River Training. Water 12 11 , 3100. doi:10.3390/w12113100

Möws, R., Koll, K., 2019. Roughness Effect of Submerged Groyne Fields with Varying Length, Groyne Distance, and Groyne Types. Water 11 6 , 1253. doi:10.3390/w11061253

Mulahasan, S., Saleh, M.S., Muhsun, S.S., 2021. Simulation of flow around a permeable dike using physical and 3D-CFD models. International Journal of River Basin Management 0 0 , 1–13. doi:10.1080/15715124.2021.1901726
Nagata, N., Hosoda, T., Muramoto, Y., 2000. Numerical analysis of river channel processes with bank erosion. Journal of Hydraulic Engineering 126 4 , 243–252.
Nagata, N., Hosoda, T., Nakato, T., Muramoto, Y., 2005. Three-dimensional numerical model for flow and bed deformation around river hydraulic structures. Journal of Hydraulic Engineering 131 12 , 1074–1087.
Nakagawa, H., Tsujimoto, T., Murakami, S., 1986. Non-equilibrium bed load transport along side slope of an alluvial stream. Presented at the Proc. 3rd Int. Symp. River Sedimentation, Jackson, Miss., USA, pp. 885–893.
Nakamura, T., 2019. Bed Deformation of Erodible Meandering Channel with Spur Dikes (Master Thesis). Kyoto University, Kyoto.
Nakamura, T., Mizutani, N., 2013. Sediment Transport Calculation Considering Laminar and Turbulent Resistance Forces due to Infiltration/Exfiltration and its Application to Tsunami-Induced Local Scouring, in: Volume 6: Polar and Arctic Sciences and Technology; Offshore Geotechnics; Petroleum Technology Symposium. Presented at the ASME OMAE2013, American Society of Mechanical Engineers, Nantes, France, p. V006T10A010. doi:10.1115/OMAE2013-10199
Nicholas, A.P., 2013. Modelling the continuum of river channel patterns. Earth Surface Processes and Landforms 38 10 , 1187–1196. doi:10.1002/esp.3431
Ning, J., Li, G., Li, S., 2019. Numerical Simulation of the Influence of Spur Dikes Spacing on Local Scour and Flow. Applied Sciences 9 11 , 2306. doi:10.3390/app9112306
Nishio, K., 2016. Study on Flow and Bed Fluctuation around Bandal like Structures under Suspended Load Trasport Condition (Master Thesis). Kyoto University, Kyoto.
Okudaira, M., 2021. Three-Dimensional Numerical Simulation on Riverbed Deformation Considering Suspended Load around Bandal-Like Structures (Master Thesis). Kyoto University, Kyoto.
OpenFOAM: User Guide [WWW Document], n.d. . OpenFOAM: User Guide v2112. URL https://www.openfoam.com/documentation/guides/latest/doc/index.html
Ota, K., Nakagawa, H., Zhang, H., 2017. Eulerian-Lagrangian simulation of bed-material load transport around partially permeable and impermeable spur dykes. Presented at the Proc. of 37th IAHR World Congress, Kuala Lumpur, Malaysia, pp. 583–592.
Ota, K., Sato, T., 2020. Three-dimensional numerical simulation of sediment control at lateral diversion. Presented at the Proc. of 22nd IAHR-APD Congress, Sapporo, Japan.
Ota, K., Sato, T., NAKAGAWA, H., 2016a. 3D numerical model of sediment transport considering transition from bed-load motion to suspension—application to a scour upstream of a cross-river structure—. Journal of JSCE 4 1 , 173–180.
Ota, K., Sato, T., Nakagawa, H., Kawaike, K., 2016b. Three-Dimensional Simulation of Local Scour around a Weir-Type Structure: Hybrid Euler-Lagrange Model for Bed-Material Load. Journal of Hydraulic Engineering 143 4 , 04016096. doi:10.1061/(ASCE)HY.1943-7900.0001263
Ouillon, S., Dartus, D., 1997. Three-dimensional computation of flow around groyne. Journal of hydraulic Engineering 123 11 , 962–970.
Paik, J., Sotiropoulos, F., 2005. Coherent structure dynamics upstream of a long rectangular block at the side of a large aspect ratio channel. Physics of Fluids 17 11 , 115104. doi:10.1063/1.2130743
Rashedipoor, A., Masjedi, A., Shojaenjad, R., 2012. Investigation on scour hole around spur dike in a 180 degree flume bend. World Applied Sciences Journal 19 7 , 924–928.
Robertson, E., Choudhury, V., Bhushan, S., Walters, D.K., 2015. Validation of OpenFOAM numerical methods and turbulence models for incompressible bluff body flows. Computers & Fluids 123, 122–145. doi:10.1016/j.compfluid.2015.09.010
Rowiński, P., Radecki-Pawlik, A. (Eds.), 2015. Rivers – Physical, Fluvial and Environmental Processes, GeoPlanet: Earth and Planetary Sciences. Springer International

Publishing, Cham. doi:10.1007/978-3-319-17719-9
Sadat, S.H., Tominaga, A., 2015. Optimal distance between pile-group and spur-dike to reduce local scour. J. JSCE, Ser. B1 71 4 , I_187-I_192. doi:10.2208/jscejhe.71.I_187
Safarzadeh, A., Salehi Neyshabouri, S.A.A., Zarrati, A.R., 2016. Experimental investigation on 3D turbulent flow around straight and T-shaped groynes in a flat bed channel. Journal of Hydraulic Engineering 142 8 , 04016021.
Seed, D., 1997. Guidelines on the geometry of groynes for river training.
Shampa, 2019. Hydro-morphological Study of Braided River with Permeable Bank Protection Structure (doctoral thesis). Kyoto University.
Sharma, K., Mohapatra, P.K., 2012. Separation zone in flow past a spur dyke on rigid bed meandering channel. Journal of Hydraulic Engineering 138 10 , 897–901.
Soares-Frazão, S., Le Grelle, N., Spinewine, B., Zech, Y., 2007. Dam-break induced morphological changes in a channel with uniform sediments: measurements by a laser-sheet imaging technique. Journal of Hydraulic Research 45 sup1 , 87-95-87–95. doi:10.1080/00221686.2007.9521835
Spinewine, B., Capart, H., Le Grelle, N., Soares-Frazão, S., Zech, Y., 2002. Experiments and computations of bankline retreat due to geomorphic dam-break floods, in: Proceedings of River Flow. Citeseer, pp. 651–661.
Stalnaker, C.B., 1995. The instream flow incremental methodology: a primer for IFIM. US Department of the Interior, National Biological Service.
Sutherland, J., Peet, A.H., Soulsby, R.L., 2004. Evaluating the performance of morphological models. Coastal Engineering, Coastal Morphodynamic Modeling 51 8 , 917–939. doi:10.1016/j.coastaleng.2004.07.015
Swartenbroekx, C., Soares-Frazão, S., Staquet, R., Zech, Y., 2010. Two-dimensional operator for bank failures induced by water-level rise in dam-break flows. Journal of Hydraulic Research 48 3 , 302–314. doi:10.1080/00221686.2010.481856
Tai, S., 2019. Effects of the Permeable Impermeable Ratio of Bandals on the Suspended Sediment Behavior around the Structures (Master Thesis). Kyoto University, Kyoto.
Teraguchi, H., 2011. Study on Hydraulic and Morphological Characteristics of River Channel with Groin Structures (PhD Thesis). Kyoto University.
The OpenFOAM Source Code Guide [WWW Document], n.d. . The OpenFOAM Foundation. URL https://cpp.openfoam.org/v8/index.html
Tripathi, R.P., Pandey, K.K., 2021a. Experimental study of local scour around T-shaped spur dike in a meandering channel. Water Supply, meandering channel 21 2 , 542–552. doi:10.2166/ws.2020.331
Tripathi, R.P., Pandey, K.K., 2021b. Numerical investigation of flow field around T-shaped spur dyke in a reverse-meandering channel. Water Supply.
Uijttewaal, W.S.J., Lehmann, D., Mazijk, A. van, 2001. Exchange processes between a river and its groyne fields: Model experiments. Journal of Hydraulic Engineering 127 11 , 928–936.
Vaghefi, M., Yaser, S., Shaker, H.S., 2016. Effects of distance between the T-shaped spur dikes on flow and scour patterns in 90° bend using the SSIIM model. Ain Shams Engineering Journal 7 1 , 31–45. doi:10.1016/j.asej.2015.11.008
van der Mark, C.F., van der Sligte, R.A.M., Becker, A., Mosselman, E., Verheij, H.J., 2012. A method for systematic assessment of the morphodynamic response to removal of bank protection, in: River Flow 2012: The Sixth Edition of the International Conference on Fluvial Hydraulics, San José, Costa Rica. Taylor and Francis, pp. 821–826.
Van Gent, M.R.A., 1995. Wave Interaction with Permeable Coastal Structures (PhD Thesis). Delft University of Technology, Delft.
van Rijn, L.C., 1984. Sediment Transport, Part II: Suspended Load Transport. J. Hydraul. Eng. 110 11 , 1613–1641. doi:10.1061/(ASCE)0733-9429(1984)110:11(1613)
van Rijn, L.C., Walstra, D.J.R., Grasmeijer, B., Sutherland, J., Pan, S., Sierra, J.P., 2003. The predictability of cross-shore bed evolution of sandy beaches at the time scale of storms and seasons using process-based Profile models. Coastal Engineering 47 3 ,

295–327. doi:10.1016/S0378-3839(02)00120-5
Versteeg, H.K., Malalasekera, W., 2007. An introduction to computational fluid dynamics: the finite volume method. Pearson education.
Walters, D.K., Bhushan, S., Alam, M.F., Thompson, D.S., 2013. Investigation of a Dynamic Hybrid RANS/LES Modelling Methodology for Finite-Volume CFD Simulations. Flow Turbulence Combust 91 3 , 643–667. doi:10.1007/s10494-013-9481-9
Wang, B., Wang, X., 2011. Spatial Entropy-Based Clustering for Mining Data with Spatial Correlation, in: Huang, J.Z., Cao, L., Srivastava, J. (Eds.), Advances in Knowledge Discovery and Data Mining, Lecture Notes in Computer Science. Springer Berlin Heidelberg, Berlin, Heidelberg, pp. 196–208. doi:10.1007/978-3-642-20841-6_17
Wu, B., Wang, G., Ma, J., Zhang, R., 2005. Case Study: River Training and Its Effects on Fluvial Processes in the Lower Yellow River, China. J. Hydraul. Eng. 131 2 , 85–96. doi:10.1061/(ASCE)0733-9429(2005)131:2(85)
Wu, W., 2007. Computational river dynamics. CRC Press.
Wu, W., Wang, S.S., 2006. Formulas for sediment porosity and settling velocity. Journal of Hydraulic Engineering 132 8 , 858–862.
Wu, W., Wang, S.S.Y., 1999. Movable Bed Roughness in Alluvial Rivers. Journal of Hydraulic Engineering 125 12 , 1309–1312. doi:10.1061/(ASCE)0733-9429(1999)125:12(1309)
Yamamoto, K., 1996. 日本の水制．山海堂.
Yang, S., Zhang, Z., Wang, Y., Liang, R., Wan, Y., Li, K., 2023. An improved 3D fish habitat assessment model based on the graph theory algorithm. Ecological Indicators 148, 110022. doi:10.1016/j.ecolind.2023.110022
Yang, X., Zhang, S., Li, W., Tang, C., Zhang, J., Schwindt, S., Wieprecht, S., Wang, T., 2022. Impact of the construction of a dam and spur dikes on the hydraulic habitat of Megalobrama terminalis spawning sites: A case study in the Beijiang River (China). Ecological Indicators 143, 109361. doi:10.1016/j.ecolind.2022.109361
Yazdi, J., Sarkardeh, H., Azamathulla, H.M., Ghani, A.A., 2010. 3D simulation of flow around a single spur dike with free-surface flow. International Journal of River Basin Management 8 1 , 55–62.
Yossef, M.F., 2002. The effect of groynes on rivers: Literature review. Delft Cluster publicatienummer 03.03. 04.
Zech, Y., Soares-Frazão, S., Spinewine, B., Le Grelle, N., 2008. Dam-break induced sediment movement: Experimental approaches and numerical modelling. Journal of Hydraulic Research 46 2 , 176–190. doi:10.1080/00221686.2008.9521854
Zhang, H., 2005. Study on Flow and Bed Evolution in Channels with Spur Dykes. Kyoto University.
Zhang, H., Nakagawa, H., 2008. Scour around spur dyke: recent advances and future researches. Disaster Prevention Research Institute Annuals. B 51, 633–652.

List of Figures

List of Tables

Curriculum Vitae

Name: 于合理（YU HELI）

Citizenship: People's Republic of China

Date of Birth: July 27, 1993

Key Qualification

Ph.D. Student (2021-2024)

Department of Civil and Earth Resources Engineering

Kyoto University, Japan

M. Sc. (2015-2018)

College of Water Resources and Hydropower

Sichuan University, China

B.E. (2011-2015)

School of Water Resources and Hydropower Engineering

Wuhan University, China

Key Employment Record

From July 2018 to September 2019

Employer: PowerChina Northwest Engineering Corporation Limited, China

Position Held: Design Engineer

Paper based on the Thesis

Yu H, Yamanoi K, Kawaike K. 3D SIMULATION OF FLOW AND LOCAL SCOUR AROUND A SPUR DIKE WITH DIFFERENT LOCATION IN MEANDERING CHANNELS WITH DIFFERENT SINUOSITY, Journal of Japan Society of Civil Engineers, Ser. B1 (Hydraulic Engineering), Vol.78, No.2, I_1207-I_1212, 2022.

Yu H, Kawaike K, Yamanoi K, Koshiba T. 3D SIMULATION OF THE EFFECT OF SPUR DIKES SPACING ON BED DEFORMATION, FLOW AND PERFORMANCE EVALUATION IN MEANDERING CHANNELS, Journal of Japan Society of Civil Engineers, Ser. B1 (Hydraulic Engineering), 2023.